3-2006

The Effects of Using Solar Radiation Pressure to Alleviate Fuel Requirements for Orbit Changing and Maintenance of the DSCS II F-13 Satellite

Jody A. Paris

The Effects of Using Solar Radiation Pressure to Alleviate Fuel Requirements for Orbit Changing and Maintenance of the DSCS II F-13 Satellite

THESIS

Jody A. Paris, Captain, USAF

AFIT/GA/ENY/06-M08

DEPARTMENT OF THE AIR FORCE
AIR UNIVERSITY

AIR FORCE INSTITUTE OF TECHNOLOGY

Wright-Patterson Air Force Base, Ohio

AFIT/GA/ENY/06-M08

The Effects of Using Solar Radiation Pressure to Alleviate Fuel Requirements for Orbit Changing and Maintenance of the DSCS II F-13 Satellite

THESIS

Presented to the Faculty

Department of Aeronautics and Astronautics

Graduate School of Engineering and Management

Air Force Institute of Technology

Air University

Air Education and Training Command

In Partial Fulfillment of the Requirements for the

Degree of Master of Science in Astronautical Engineering

Jody A. Paris, B.S.A.E.

Captain, USAF

March 2006

AFIT/GA/ENY/06-M08

The Effects of Using Solar Radiation Pressure to Alleviate Fuel Requirements for Orbit Changing and Maintenance of the DSCS II F-13 Satellite

Jody A. Paris, B.S.A.E.
Captain, USAF

Approved:

Lt Col Nathan A. Titus, PhD Thesis Advisor	8 Mar 06 date
Dr. William E. Wiesel Committee Member	8 Mar 06 date
Lt Col Kerry D. Hicks, PhD Committee Member	8 Mar 06 date
Maj Christopher G. Smithtro, PhD Committee Member	6 Mar 06 date

AFIT/GA/ENY/06-M08

Abstract

Orbit disposal and maintenance of aging satellites has become a significant concern over the past few years, as the increasing number of orbiting objects in high-value orbits (e.g. geosynchronous) threatens to limit the launching of future satellites and spacecraft. Many of the satellites currently in orbit, however, were not built with disposal considerations. The DSCS II series, for example, was launched into orbit beginning in the 1970s, and many satellites are now without the fuel required to conventionally transition to a sanctioned disposal orbit. In geosynchronous orbit, however, the largest non-gravitational perturbation is solar radiation pressure (SRP). By adjusting the position of the satellite with a controller to maximize the perturbing acceleration due to the force of SRP, the satellite can be slowly raised into an appropriate disposal orbit. The results from this study, along with validation results propagated with Satellite Tool Kit, are presented. After making several simplifying assumptions (primarily a cylindrical Earth shadow, flat plate geometry, and constant cross-sectional area of the satellite), the time required to raise the modelled DSCS II F-13 satellite 400 km into a disposal orbit is approximately 33 years. This time-to-disposal can be reduced by using a larger area-to-mass ratio and more reflective surface materials.

Acknowledgements

First and foremost, I would like to thank my husband for your love, support and technical help during the course of my thesis work. Additionally, I'd like to thank my advisor, Lt Col Nathan Titus, and thesis committee members, Dr. William Wiesel, Lt Col Kerry Hicks, and Maj Christopher Smithtro for the professional guidance and genuine encouragement you provided me. Dr. Charles "Chuck" Leakas, thank you for your LaTeX wisdom and MATLAB® assistance when things just wouldn't work as I thought they should. Finally, I offer gratitude to my colleagues, Capt Phillip Corbell and Lt Steve Mawhorter, for offering up ingenious ways to improve my code–without you guys, I'd still be running those test cases by hand!

Jody A. Paris

Table of Contents

Page

Page

List of Figures

List of Tables

List of Symbols

Symbol		Page
ψ	shadow function	12
a	semimajor axis	19
e	eccentricity	19
i	inclination	19
Ω	right ascension of the ascending node	19
ω	argument of perigee	19
ν	true anomaly	19
n	mean motion	21
$\mu_\oplus$	gravitational parameter of the Earth	21
E	eccentric anomaly	21
t	time	21
r_a	radius of apoapsis	21
r_p	radius of periapsis	21
h_a	height of apoapsis	21
h_p	height of periapsis	21
T	orbital period	21
ε	total specific mechanical energy	21
r	radius	21
h	height	21
L	true longitude	22
p	semilatus rectum	22
λ_o	mean longitude	22
ϖ	longitude of periapsis	23
θ	argument of latitude	23
u	argument of latitude	23
Δ_r	non-two-body perturbation acceleration in the radial direction	25

Symbol		Page
Δ_t	non-two-body perturbation acceleration in the tangential direction	25
Δ_n	non-two-body perturbation acceleration in the normal direction	25
$\vec{\Delta}$	total disturbing acceleration vector	26
M	mean anomaly	27
$\hat{i}_N$	unit vector in local North direction	28
$\hat{i}_r$	unit vector in the radial direction	28
$R_\oplus$	equatorial radius of the Earth	29
ϕ_{gc}	geocentric latitude	29
J_k	kth zonal harmonic coefficient	29
$P_k(\sin\phi_{gc})$	kth order Legendre polynomial with corresponding derivative	29
r_I	I component of the ECI position vector	30
r_J	J component of the ECI position vector	30
r_K	K component of the ECI position vector	30
SF	solar flux	31
$D_{aphelion}$	Earth aphelion	31
p_{SR}	solar pressure per unit area	31
c	speed of light	31
ϕ_{inc}	solar radiation incident angle	31
ϕ_{ref}	solar radiation reflected angle	33
m	satellite mass	33
A_{exp_s}	average effective cross-sectional area of the spin-stabilized platform	35
A_{exp_d}	average effective cross-sectional area of the despun platform	35
$\hat{s}$	unit vector from the satellite to the Sun	36
$\vec{r}_{\oplus\odot}$	Earth-Sun vector	36
$\lambda_{M_\odot}$	mean longitude of the Sun	37
$M_\odot$	mean anomaly of the Sun	37
$\dot{E}$	rate of orbital energy	42

Symbol		Page
$\vec{v}$	ECI velocity vector	42
Ψ	celestial longitude of the Sun	44

List of Abbreviations

The Effects of Using Solar Radiation Pressure to Alleviate Fuel Requirements for Orbit Changing and Maintenance of the DSCS II F-13 Satellite

I. Introduction

1.1 Motivation: Using Solar Radiation Pressure as a Controller

Detachment 12 of the Space and Missile Systems Center (SMC Det 12) serves as the primary provider of launch capability, spaceflight and on-orbit operations for Department of Defense users [27]. SMC Det 12, and the Air Force Space Command in general, has continuing interest in the area of orbit disposal and maintenance of aging satellites. In particular, the study of moving an existing satellite (that has expended all of its onboard fuel supply) into a disposal orbit is of interest, as is, conversely, de-orbiting a satellite using low-fuel maneuvers and potential lunar flybys. The first topic will be addressed in this thesis; the second is left as future work.

For high altitude orbits, solar radiation pressure becomes the dominant perturbative force, especially for satellites with large surface areas. By intentionally aligning a satellite's orientation with respect to the sun, this perturbative force can be used to maneuver the vehicle. This could potentially be used as a means of moving satellite into disposal orbits when there is insufficient fuel onboard. This topic has been of particular interest to the Air Force and Department of Defense of late due to the increasing number of in-orbit vehicles. As a result, research into the disposal of satellites (and the related topic of collision avoidance) has been encouraged.

An additional benefit, by having this technique available, is that the mission life of many Air Force satellites might be extended because less fuel would be needed for station keeping and/or orbit maintenance. This thesis uses a representative Air Force spacecraft, a Defense Satellite

Communications System (DSCS) F-13 satellite, as a test vehicle for demonstrating the ability of solar radiation pressure to alleviate fuel requirements for orbit changing and/or orbit maintenance.

1.2 Background

1.2.1 Orbital Perturbations and Solar Radiation Pressure. Every object in space, whether in orbit about a planet (e.g. Earth) or flying through interstellar regions, experiences small changes in its two-body motion caused by external forces. These disturbances are called orbital perturbations, and fall into two main categories: gravitational and non-gravitational. Gravitational perturbative forces are those involving the gravitational attraction of secondary bodies (i.e. Earth, Moon or Sun) on the satellite. Non-gravitational perturbative forces are all the other types of disturbances, including atmospheric drag, solar radiation pressure and Earth albedo. For Earth-orbiting satellites, such as the DSCS II F-13, the dominant perturbations are gravitational. The common spacecraft perturbations for satellites orbiting in the geosynchronous belt are listed in Table 1.1 [10].

In this thesis, the primary gravitational perturbations that will be considered are from the Sun and the Earth. The uneven mass distribution of the Earth causes zonal harmonics, which act to alter the apparent forces of the Earth on the satellite depending on where the satellite is orbiting about the Earth. The main gravitational perturbation for a satellite in geosynchronous orbit is the second-order even zonal harmonic, commonly referred to as the Earth oblateness and/or J2 perturbation. The solar third-body perturbation affects the satellite orbit slightly less, although the modelling of the disturbance is significantly more difficult computationally than for the J2 perturbation due to the complicated orbit of the Earth about the Sun and the magnitude of the vectors involved. The orbital perturbations caused by the Sun's gravity are less than for the Moon (which will be neglected due to computational instability, with no diminished value of the thesis), but have a greater effect than solar radiation pressure.

Table 1.1: Common Geosynchronous Satellite Perturbations, Adapted from [10].

Perturbation	Formula	Acceleration (m/s^2) of Geosynchronous Spacecraft with $A/M = 0.01 m^2/kg$
Earth's Oblateness	$3\frac{GM_\oplus}{r^2}\left(\frac{R_\oplus}{r}\right)^2 J_{20}$	7.4×10^{-6}
Lunar Third Body	$2\frac{GM_m}{r^3}r$	7.3×10^{-6}
Solar Third Body	$2\frac{GM_\odot}{r_\odot^3}$	3.3×10^{-6}
Atmospheric Drag	$\frac{1}{2}C_D\frac{A}{M}\rho V^2$	negligible
SRP	$\frac{A}{M}\frac{\Phi_\odot}{c}$	4.6×10^{-8}
Earth's Albedo	$\frac{A}{M}\frac{\Phi_\odot}{c}A_\oplus\left(\frac{R_\oplus}{r}\right)^2$	4.2×10^{-10}

The primary non-gravitational perturbation for a geosynchronous satellite like the DSCS II F-13 comes from solar radiation pressure (SRP). The SRP disturbance is caused by incoming incident solar photons impinging on an energy absorbing surface (the satellite), which generates a force per unit area on the surface. If the vector sum of all the forces acting on the distinct segments of the satellite does not pass through the satellite's center of mass, a torque will also be generated [8]. The SRP perturbation is essentially equivalent to adding an incremental velocity (Δv) to one end of the orbit (e.g. perigee) and subtracting the same Δv at the other end (e.g. apogee), causing the orbit to gradually become elliptic. Six months later, the Earth is at the opposite side of its orbit around the Sun, and the action is reversed to recircularize the orbit [9]. Figure 3.7 illustrated this concept.

1.2.2 DSCS II F-13. The satellite chosen for study in this thesis is the DSCS II F-13, which was launched into a geosynchronous orbit on 21 November 1979 from Cape Canaveral,

Florida. The 16 TRW-built DSCS II satellites form a constellation of communications satellites once charged with relaying secure voice and data communications for the United States military. They replaced a set of 26 spacecraft launched under the Department of Defense's Initial Defense Communications Satellite Program beginning in 1966. Each DSCS II spacecraft is a cylindrical spin-stabilized satellite with a despun antenna platform housing two parabolic antennas. The spin-stabilized cylinder is covered with a layer of body-mounted solar arrays to provide electrical power augmented by a system of three Nickel Cadmium batteries.

The DSCS II F-13's initial mass was 611 kg; it had an initial perigee height of 37104 km and an initial apogee height of 37195 km. Upon reaching orbit, the satellite's inclination was 13.6^o. Its design life was only intended to be five years, but the satellite provided many more years of valuable service to the Department of Defense (DoD). Additional parameters for the DSCS II F-13 can be found in Appendix A [23, 37].

1.3 Research Goals

1.3.1 Problem Statement. The primary objective of this thesis is to determine how long it will take to raise the orbit of the DSCS II F-13 satellite into a disposal orbit using SRP. To meet this goal, this thesis undertakes the development of a numerical model in MATLAB® to simulate the satellite's orbit, orientation with respect to the sun and the effects of the perturbative forces caused by the solar radiation pressure, Earth oblateness and the solar third-body effects. In addition to the simulation effort, the thesis involves the development of two techniques to control the attitude of the satellite by taking advantage of the applied solar radiation pressure forces.

1.3.2 Scope and Assumptions. The DSCS II F-13 satellite will be modelled with approximated despun and spin-stabilized platform areas. The code will implement a case structure, which will enable several parameters to be easily varied: despun platform area, coefficients of absorption and specular and diffuse reflection of the despun platform area, number of orbits and the controller

used. The solution will be propagated with a cylindrical Earth shadow, constant cross-sectional area of the satellite and the perturbations addressed in Section 1.3.1. The modified equinoctial equations of motion of the satellite will be integrated to obtain the solution and the results will be plotted.

For the purposes of this thesis, the collision avoidance problem will not be addressed. Nor will the number of man-hours required to raise the orbit have a consideration on the complexity of the controller used, although it would indeed in the operational world. The contributions of several perturbations will not be examined, due to the small effects they have on satellites in geosynchronous orbit. These include perturbing forces due to atmospheric drag, the Earth's magnetic field, Earth albedo and infrared radiation pressure, higher order even zonal harmonics, sectorial harmonics, tesseral harmonics and tides. The model will not include periods of dramatically increased or decreased solar activity or a conical Earth shadow model due to the small percentage gain in accuracy (approximately 5% for each). Since the unknown surface properties of the satellite cause the results to vary by as much as 80%, the additional computation time required to model these perturbations yields no real added value.

To limit the run time of the code to a reasonable threshold, a number of simplifying assumptions were used. As previously mentioned, a cylindrical shadow model is used that neglects the penumbra and umbra regions. This shadow model essentially regards the Sun as a point source, and neglects the transition regions of the shadow projection. Additionally, the shadow is considered to be unaltered due to any flattening of Earth's pole and/or changes in atmospheric density, although both could be considered for future work.

Further assumptions include a constant (original) satellite mass and approximated satellite surface areas. The satellite parameters are not well documented; the area of the parabolic antennae on the despun platform can only be estimated. For the purposes of this thesis, the parabolic antennas will be combined and modelled as one flat plate with zero thickness. The mass of the

satellite is considered to be negligible for purposes of the solar third-body perturbation calculations. Additionally, the nominal coefficients of specular reflection, diffuse reflection and absorption are taken to be one-third each, since the current reflective properties of the satellite are not well known.

The SRP model used in the development of the simulation code ignores any torque caused by SRP resultant force acting outside the satellite's center of mass. Several algorithms from Vallado's text were referenced in the development of the code, and they each have their own inherent assumptions. These assumptions are minor as compared to the simplifying assumptions already addressed, and may be referenced in the text accompanying the algorithms in his book [32].

For the purposes of this thesis, the desired disposal orbit is defined as 400 km above the epoch altitude of the satellite for the DSCS II, as it already resides in the disposal orbit set forth by the United States Space Command in Appendix D. Additionally, the orbital period is considered to be constant over the integration time, and the equatorial radius of the Earth is considered to remain at a constant 6378 km.

Finally, Coverstone's controller model (see Section 3.4.2) has inherent simplifications and assumptions. Most notably, she assumes only specular reflection and a constant solar flux. Further information regarding her assumptions can be found in her paper [11].

1.4 Overview of Chapters

The structure of the thesis is such as to guide the reader through the thought processes involved. The next chapter summarizes the previous research conducted relating to the subject matter, and provides the groundwork for cultivating an appropriate model for the orbit of the DSCS II F-13. Chapter III presents, in detail, the theory and equations behind the algorithms used to create the model of the orbit. Chapter IV will enumerate the numerical results obtained from the MATLAB® model developed in Chapter III. Recommendations and conclusions will then be outlined in Chapter V, along with suggestions for any future work that might be performed.

II. Background

2.1 The Infancy of Solar Radiation Pressure Research

The earliest studies of SRP began in the late 19th century. Not until the first spacecraft were launched in the middle of the 20th century, however, did in situ data become available, and hence theories were experimentally proven. Over the past century, our knowledge of SRP and its perturbing effects on spacecraft in Earth orbit and interplanetary space has matured and developed into an intricate science. For many years, the focus of SRP studies was confined to the minimization of its effects on spacecraft. More recently, considerable effort has been put into the development of applications to harness the SRP effects for purposes of interplanetary propulsion, namely with solar sails. Consequently, the work begun by many pioneers of the late 1800s and early 1900s has come full circle as their theories are now used to harness the SRP acceleration as opposed to minimizing its effects. The focus of this thesis rests in this area: using the perturbing SRP acceleration to raise the orbit of a satellite.

Although this thesis concentrates on the effects of SRP, it is important to note that the field of study grew from work regarding radiation pressure on Earth. In 1873, Scottish physicist James Clerk Maxwell set forth the first suppositions about the existence of radiation pressure [29]. For nearly 30 years after Maxwell, the subject matter laid effectively dormant, until Nichols and Hull from Darthmouth College and Russian physicist Peter Lebedev were able to (independently) experimentally measure radiation pressure in precision laboratory tests in 1900. About the same time, one of Maxwell's students, English physicist and mathematician John Henry Poynting, suggested the existence of an effect of the Sun's radiation that causes small particles orbiting the Sun to gradually approach it and eventually enter the Sun's atmosphere.

The earliest study of SRP in particular began in 1924, when Russian astronautics pioneer Konstantin Eduardovitch Tsiolkovsky, widely considered the father of astronautics and rocket dynamics, and his colleague, Russian engineer Fridrickh Arturovich Tsander, first introduced a proposal to

use SRP as a method of spacecraft propulsion. Their concept used very thin sheets of mirrors with large surface areas to harness the Sun's radiation pressure as a form of propulsion. These concepts matured into the evolution of practical solar sailing, first written of by Tsander around 1924 [22]. During this period, Poynting completed the first study of the Sun's radiation pressure as it affects small meteorites in interplanetary space. Later, American cosmologist Howard Percy Robertson expanded on Poynting's research and the resulting theory is now called the Poynting-Robertson effect.

2.2 The Space Age

After the first spacecraft (Sputnik I and II, Explorer-I and Vanguard) were successfully launched in the late 1950s, in situ data on the perturbing effects of SRP became available. The launch of the Vanguard and Echo1A satellites, and the ensuing perturbations, fueled scientists around the world to study the effects closely and develop accurate models that would predict the effects of SRP on spacecraft during their orbital lifetime. Koskela, Kozai and Musen, three scientists that studied these early perturbations, each sought to build models to describe the SRP effects on satellites in Earth orbit. These men all used simplifying assumptions in their derivations, most notably constant solar flux, constant satellite area (perpendicular to the solar radiation vector), cylindrical Earth shadow, no diffuse reflection and no absorption [10].

In the early 1960s, scientists began to hone the models developed by the first researchers (namely Koskela, Kozai and Musen). Robert Bryant, who was working for the National Aeronautics and Space Administration (NASA) Goddard Space Flight Center, sought to refine the previous work by conducting his own study in 1961. He was the first to observe that when Earth's shadow is neglected in the orbital propagation model, a spacecraft will only experience short periodic changes in its semimajor axis. Conversely, when the SRP model includes the shadow, the satellite will experience a more significant perturbation. This had great implications for users at the time,

since the principal finding of Bryant's work indicated that the long-term effects of SRP are much greater when a satellite experiences solar eclipsing by the Earth [7, 10]. This discovery will prove to be a driving factor in the development of this thesis, as the problem requires not the short-term perturbations of the semimajor axis, but the long-term effects obtained by spending time in Earth's shadow.

2.3 Modern Research and Applications

As the years elapsed from Bryant's groundbreaking discovery in the early 1960s, spacecraft rapidly evolved into more complex vehicles. The equations of motion that were sufficient to properly track orb-shaped satellites in low-earth orbits were no longer adequate. More powerful launch vehicles enabled satellites to reach higher orbits, and the effects of SRP began to dominate the perturbations. New generations of scientists were directed to study the effects of SRP under these new conditions.

Harwood et al. began with the simplest of satellites, a spherical spacecraft. This spacecraft had a constant cross-sectional area and an acceleration vector that was perpendicular to the SRP vector, which greatly reduced (with the assistance of other simplifying assumptions) the computational time need to analyze the SRP perturbations. Harwood introduced a varying Earth-Sun (and therefore satellite-Sun) distance, which enabled the solar flux constant to be realistically varied according to time of year. For the first time, a time-varying SRP acceleration was studied.

The first satellite to require precise SRP modeling was the oceanographic satellite Ocean Topography Experiment (TOPEX)/Poseidon . This satellite was built to acquire altimeter measurements, which are used to map the ocean topography. TOPEX/Poseidon justified further study and application of more accurate models for SRP disturbing acceleration, because even small errors in the orbit determination process would be magnified into significant inconsistencies in its topographical measurements. Marshall et al. developed a more rigorous modeling tool that simulated

the satellite with a box-wing shape (a box as the main body and flat plates for the solar panel arrays). The satellite's cross-sectional area was allowed to shift as it rotated around the Earth and underwent programmed attitude changes. Like earlier studies, some simplifying assumptions were made by the authors, such as a cylindrical Earth shadow and constant surface reflection properties. The authors implement Lambert's cosine law for diffuse reflection (as does Vallado [32]), which, although a simplification of the full diffusion model, is more than most authors use in their research. In Marshall's model, the authors also accounted for the lesser perturbations due to the satellite's thermal emissions, Earth's albedo, and Earth's infared emissions [10].

Much of the contemporary modeling research efforts are focused on the effects of SRP perturbations on interplanetary spacecraft. One such project is the Japanese Selenological and Engineering Explorer (SELENE), which will use an octagon-shaped relay satellite to transmit communications between SELENE's main orbiter and Earth following SELENE's launch in 2007 (see Figure 2.1). The long-term effects of SRP on the relay satellite will be studied for approximately one year, once it achieves its elliptical orbit around the Moon [36]. Since the Moons mass is relatively insignificant, it cannot hold much of an atmosphere, and hence SRP becomes the dominant non-gravitational perturbation acting on the satellite. For this reason, the effects of SRP on the lunar-orbiting satellite must be modeled accurately. Project engineers used force equation models similar to those postulated by Chobotov, Ries et al. and Milani et al. in their derivation of the SRP effects, but have neglected the shadow of the Moon [10].

A program widely used in the astrodynamics community to study the general effects of perturbations was developed by the Charles Stark Draper Laboratory. The Draper Semi-analytical Satellite Theory (DSST) model analytically separates the secular and long-periodic motions from the short-periodic motion, thus enabling the user to modify the modeled forces to suit their accuracy and computation time requirements. DSST makes several assumptions; the SRP model uses a cylindrical Earth shadow and a constant coefficient of reflection. The DSST model is convenient

Figure 2.1: SELENE Orbiter. The spacecraft has three components: the main orbiter, a small relay satellite, and a small Very Long Baseline Interferometry (VLBI) satellite. The main orbiter, which has a rectangular box shape, carrys the scientific instrumentation. The relay satellite is an octagonal shape and will be used to communicate between the orbiter and Earth. The VLBI satellite is the same shape as the relay satellite; its purpose is to conduct investigations on the position and precession of Earth's moon [24].

for many users because it tailors the program to take advantage of the best of both general and special perturbation techniques. Cefola et al. have recently used the DSST program to study the short-periodic motion of formation flying satellites [25].

An additional study of non-gravitational perturbations was presented by Bruce Bowman et al., of the Space Warfare Center at Schriever Air Force Base (AFB) in Colorado, in 2000. His paper addressed the long-term effects of SRP, atmospheric drag and Earth albedo on the approximately 20 West Ford needles clusters that formed after the initial package was launched in 1963. The copper needles, which have a large area to mass ratio, decayed rapidly once placed in orbit, and clusters were formed due to delays in releasing the needles.

Bowman's analysis is of interest, as the long-term perturbations due to direct SRP found in the West Ford needles could be analogous to the attempted raising of an orbit in this thesis. Although the needles are primarily located in a low earth orbit (LEO) orbit, without active control the West Ford needles exhibited a semimajor axis displacement of approximately 10 km in 34 years [10]. In a GEO orbit, as for this thesis, the semimajor axis should be expected to raise much more in the same amount of time (with a controller), so the results from Bowman are encouraging.

2.3.1 Earth Shadow Models. It is important to note at this point that many researchers over the past century have made simplifying assumptions regarding the Earth's shadow, namely by either using a cylindrical model for analysis or neglecting the shadow entirely. For calculations where the effects of SRP on a spacecraft were not required to be known absolutely, or over long periods of time, neglecting the shadow is acceptable. In the application addressed in this thesis, however, SRP effects play a major role in the outcome, and the simplifying assumptions made by previous authors will not provide an accurate enough model.

One of the simplest models used to model SRP in the presence of Earth's shadow was proposed in 1971 by Sylvio Ferraz Mello. He introduced a shadow function, ψ, which is set equal to one if the satellite is illuminated and to zero when the satellite is in shadow [12]. A more sophisticated

method was developed by Kabelac in 1988. He derived a method which uses a more realistic conical Earth shadow with both penumbra and umbra regions. Kabelac's model accounts for the mutual position of the Sun, Earth and satellite, the shape of conical surface, light diffusion, atmospheric absorption and the effect of ozone [16].

A number of researchers have used the updated shadow models to analyze spacecraft eclipse transition effects in further detail. Vokrouhlicky et al. have written a sequence of papers on this topic. The papers use Kabelac's model to analyze the shadow effects on a spacecraft as it transitions between regions of the shadow projection. The authors note that the apparent size of the sun, with respect to the spacecraft, changes as the spacecraft moves in and out of the penumbra region [33]. The authors then, in later papers, expound upon Kabelac's model to include the altering of Earth's shadow due to the flattening of Earth's pole and changes in atmospheric density [10]. This particular inclusion is beyond the scope of this thesis but could be addressed in follow-on studies.

2.3.2 Advanced Solar Radiation Pressure Force Models. Modern scientists have also focused on developing more accurate solar radiation pressure force and torque models. R.M. Georgevic, perhaps the first to consider modeling the effects of SRP on reflecting surfaces, developed a mathematical archetype for computing the radiation pressure force and torques on both a parabolic high gain antenna and a circular cylinder in 1973. Georgevic emphasized the importance of approximating a body's irradiated surface area and determining the specular and diffuse reflection vectors [13]. David Vallado based his model for SRP acceleration on Georgevic's early work and on Burns et al. (2000). Burns et al. developed an attitude guidance law for time-varying spacecraft orientation, which is more realistic than assuming the satellite maintains a constant attitude normal to the Sun. Vallado's model includes absorption and specular and diffuse reflection. To model the diffuse reflection, he assumes a Lambertian reflective surface; this means that light impinging on the surface is scatted such that the surface luminance is the same regardless of the observer's viewing angle. Not all surfaces are perfect Lambertian reflectors, but the approxima-

tion is generally a good one for surfaces with unknown characteristics. Vallado also implements a macro-model approximation technique for the shape and orientation of the satellite [32]. Vallado's model will be incorporated into this thesis.

2.3.3 Modified Equinoctial Orbital Elements. For most astrodynamics problems, one of the first decisions to make is which coordinate frame to use in defining the spacecraft position and dynamics. For the purposes of this thesis, geosynchronous (and near-geosynchronous) satellites are being considered exclusively. Due to the special nature of these orbits, including eccentricities and inclinations of near zero degrees [4, 32], defining an appropriate coordinate system becomes important in avoiding singularities. Perhaps the most obvious set of elements is the equinoctial (EQU) orbital elements, as they are free from singularities for zero eccentricities and both zero and ninety degree inclinations.

The EQU set are functions of the mean anomaly, M and of the classical orbital elements eccentricity, e, inclination, i, argument of perigee, ω and right ascension of the ascending node, Ω. Broucke and Cefola applied the EQU elements, based on the initial definitions by Arsenault et al., to the two-body problem for general and special perturbations [6].

Somewhat more recently, however, Walker et al. redefined the set as the modified equinoctial elements (MEE) by substituting the semiparameter for the semimajor axis and introducing a different "fast variable", the phase angle. The authors chose to replace the mean longitude of the EQU set (Cefola's "fast variable") with the true longitude, thus setting the true longtitude as the element fixing position within the orbit. By replacing the semimajor axis, the authors effectively obtained a set of elements that is applicable to most orbits and have non-singular equations of motion [34]. Noting that two of the elements are singular for an inclination of 180° (an orbit which to this date has no satellites in it), the MEE set of orbital elements are the most appropriate for the application of this thesis [4].

Several authors have used the MEE set of elements for projects and research in the recent years. Betts used the MEE set to define both his vehicle dynamics and trajectory modeling for a low-thrust optimization problem in 2000 [4], in a 1994 paper describing the direct transcription method of numerical analysis for optimal interplanetary low-thrust orbit transfers [3] and in a 2003 paper regarding optimal low-thrust trajectories to the moon [5]. Betts based much of his work using the MEE element set on theory developed by Dr. Jean Kechichian, who authored several papers that used EQU coordinates [17,18]. The low-thrust application is of interest concerning this thesis, as the acceleration from SRP qualifies, certainly, as a low-thrust acceleration. Trawny et al. used the MEE set for a controlled lunar impact mission, which also included a trade study of low-thrust pulsed plasma thrusters versus a solid rocket booster [30].

2.3.4 Solar Sails. Much of the recent emphasis on the exploration of SRP effects has been in solar sail research. Refer to Figures 2.2 and 2.3 for representative illustrations of concept solar sails. Scientists are currently developing methods for harnessing the SRP forces as a source of propulsion for long-term interplanetary space travel. Solar sails are particularly attractive for this application because, unlike conventional propulsion methods, solar sails require no onboard fuel source. Even though the thrust produced from radiation pressure is small, it will continue as long as the sail is viable and the satellite can maintain a visual path to the Sun. The principles that have been developed for use by solar sails, however, still apply to satellites not equipped with sails. Solar panels, temperature-control panels and sun shades can also, in effect, be used like solar sails. This thesis will study the feasibility of implementing various architectures on satellites for better utilization of the perturbing acceleration caused by SRP to raise a satellite's orbits.

Victoria Coverstone has spent a number of years researching solar sails, and has published many papers regarding interplanetary travel and transfer orbits using solar sail technology. One paper in particular develops a technique for escaping the Earth using a solar sail. She begins with a spacecraft in a geosynchronous transfer orbit and uses a control algorithm to maximize

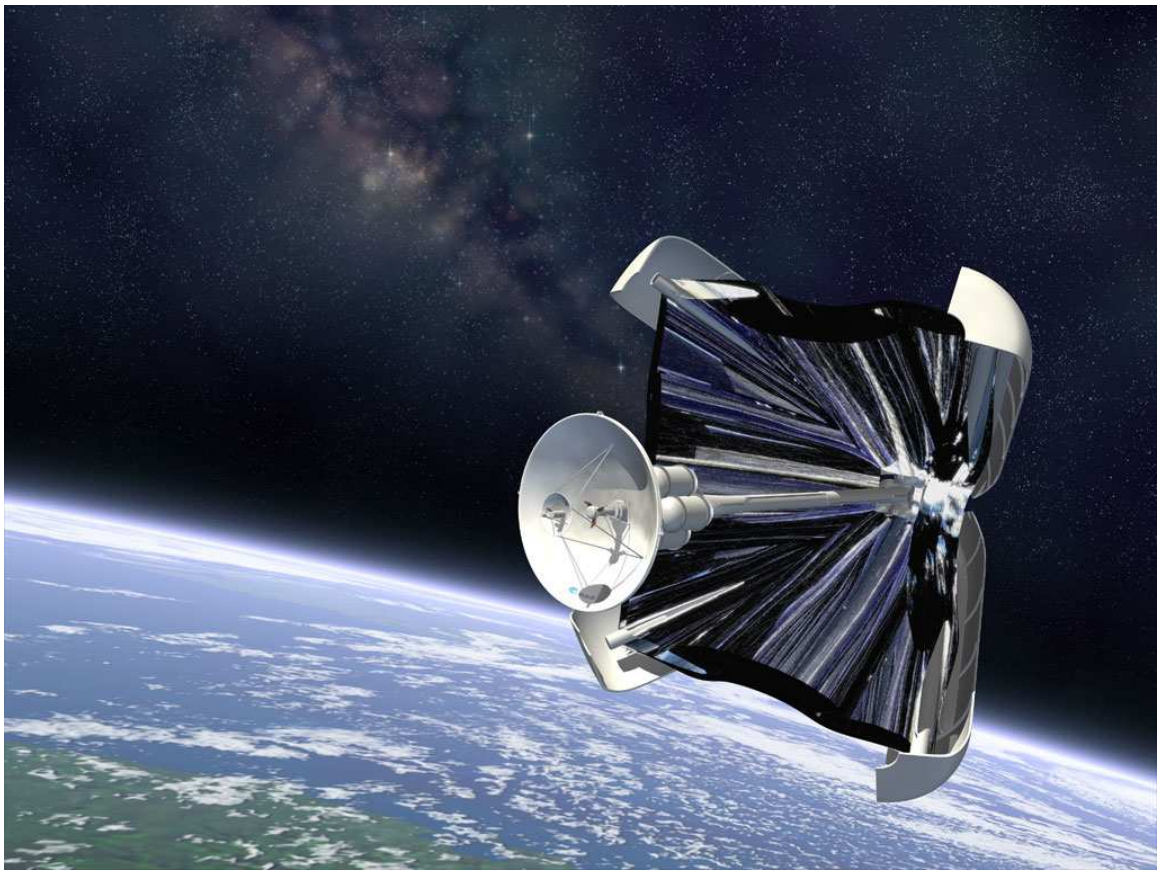

Figure 2.2: NASA Artist's Rendering of a Conceptual Solar Sail Deploying [23].

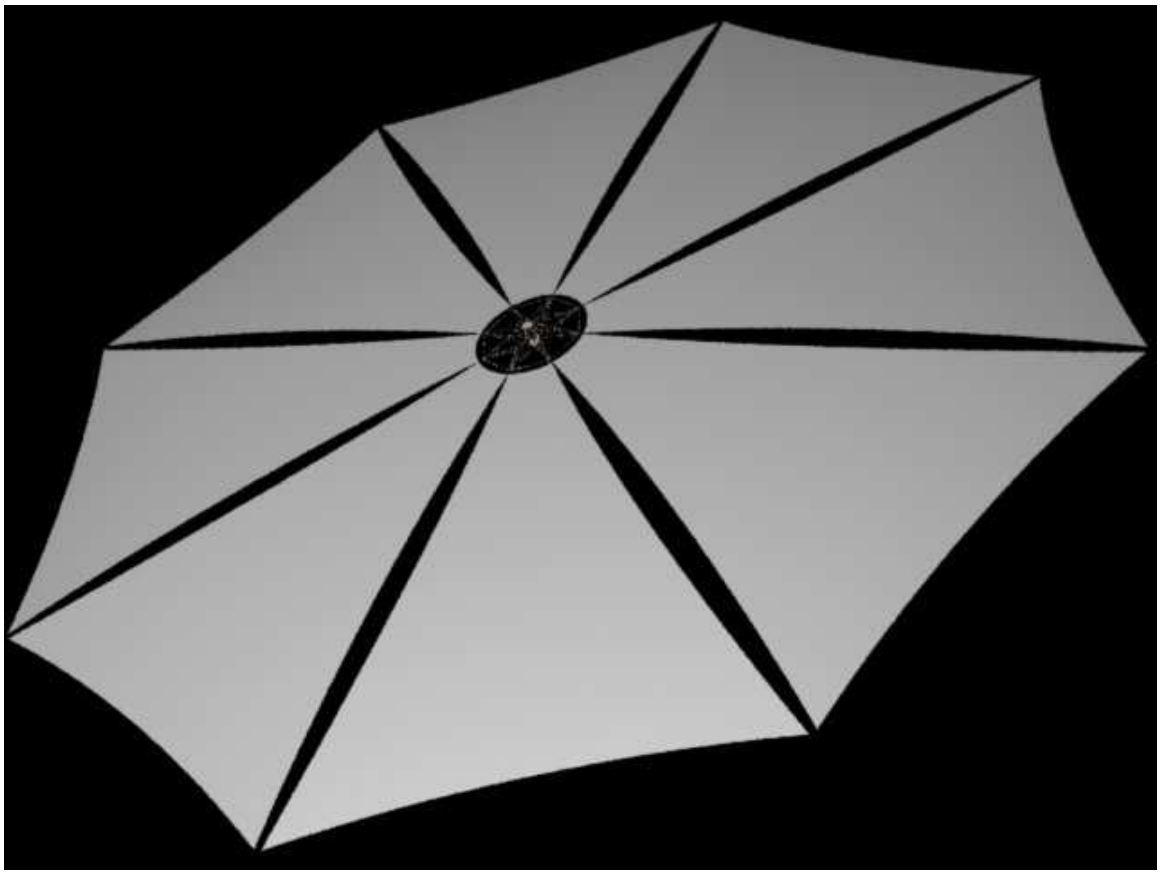

Figure 2.3: Artist's Rendering of a Deployed Circular Solar Sail [23].

the component of sail force along the velocity vector, thus maximizing the instantaneous rate of increase in the total orbital energy. This thesis will make use of her work with solar sail control algorithms in the MEE coordinate frame to optimize the force on the satellite, thereby raising the orbit at a faster rate [11].

III. Methodology

The theory and equations presented in this chapter were used by the author to build the orbital propagation model in MATLAB® (reference Appendix C for the full set of source code). The algorithm to calculate the eccentric anomaly was obtained from an outside source (see Section C.1).

3.1 Finding Classical Orbital Elements from the Two-Line Element Set

Data from the most recent two-line element set (TLE), along with the necessary constants for orbital propagation, are the required inputs into the MATLAB® code in Appendix C. A TLE is the standard format for communicating the information pertaining to the orbit of a specific Earth-orbiting object. A snapshot (at a given time, or epoch) of the satellite can be taken and sent to another organization for purposes of tracking the object. More information on the TLE, particularly for interpreting the TLE, can be found in Appendix A.

Many orbital problems begin with the calculation of the six classical orbital elements (COE), which in most texts are given by the semimajor axis, a, the eccentricity, e, the inclination, i, the right ascension of the ascending node, Ω or RAAN, the argument of perigee, ω, and the true anomaly, ν. Figure 3.1 illustrates the COE arrangement for a sample orbit.

From the TLE, several of the COE, along with numerous other parameters, are extracted: i_o (degrees), Ω_o (degrees), e_o (dimensionless), ω_o (degrees), mean anomaly, M_o (degrees), and mean motion, n_o (revs/day) [28]. The subscript o indicates the value at epoch (reference time), which is defined as the date and time given in the TLE.

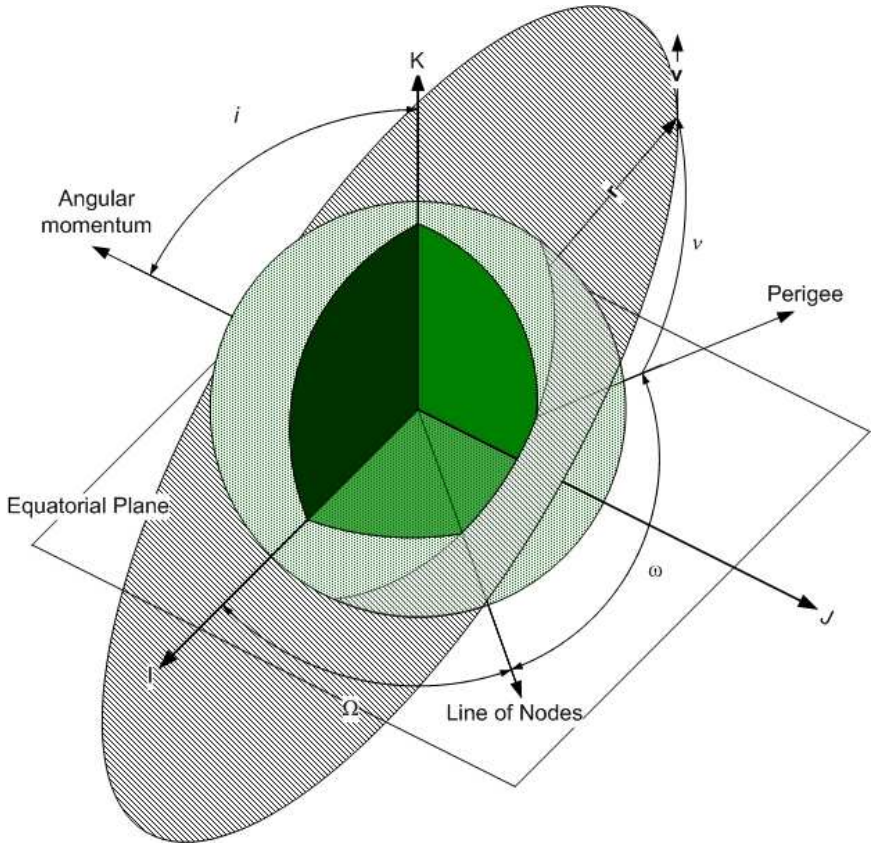

Figure 3.1: COE Geometry. The COE a and e are difficult to depict in this figure, and thus are omitted.

After converting degrees to radians and n to units of radians per second, the remaining COE are calculated through the formulas

$$a = \left(\frac{\mu_\oplus}{n^2}\right)^{1/3} \tag{3.1}$$

$$\nu = 2\arctan\left[\left(\sqrt{\frac{1+e}{1-e}}\right)\tan\left(\frac{E}{2}\right)\right] \tag{3.2}$$

where $\mu_\oplus$ is the gravitational parameter of the Earth and E is the eccentric anomaly [14]. Note from this point forward the subscript o will be dropped, as these formulas are applicable to any time t in the orbit. E may be calculated through a Newton-Raphson iteration (see Section C.1 for details) [26].

Several other orbital parameters are of interest, and may be calculated using the equations

$$r_a = a\,(1+e) \tag{3.3}$$

$$r_p = a\,(1-e) \tag{3.4}$$

$$h_a = r_a - R_\oplus \tag{3.5}$$

$$h_p = r_p - R_\oplus \tag{3.6}$$

$$T = 2\pi\sqrt{\frac{a^3}{\mu_\oplus}} \tag{3.7}$$

$$\varepsilon = \frac{-\mu_\oplus}{2a} \tag{3.8}$$

$$r = a\,(1 - e\cos E) \tag{3.9}$$

$$h = r - R_\oplus \tag{3.10}$$

where r_a is the radius of apoapsis, r_p is the radius of periapsis, h_a is the height of apoapsis, h_p is the height of periapsis, T is the orbital period, ε is the total specific mechanical energy, r is the instantaneous radius of the spacecraft and h is the instantaneous height of spacecraft [14].

These parameters are used to calculate the modified equinoctial elements, and hence the equations of motion, in Section 3.2 below.

3.2 Modified Equinoctial Elements

The MEE were derived from a set of equinoctial orbital elements first described in Broucke and Cefola [6]. The equinoctial set was derived to avoid the singularities that accompany the COE, namely, Ω becoming indeterminate as the inclination goes toward zero and ω becoming indeterminate as the eccentricity goes toward zero. The equinoctial elements, however can result in singular equations of motion with some perturbation techniques.

The MEE set was developed by Walker et al. to eliminate the singularities associated with those perturbation techniques. Walker et al. employed a different "fast variable", the true longitude L, and the semilatus rectum p as opposed to the mean longitude λ_o and the semimajor axis. In doing so, the authors derived a set of elements that, when used in any perturbation technique, enables them to be applicable to all orbits and have non-singular equations of motion. These characteristics lend the MEE set toward use for geosynchronous orbit problems. The set of MEE equations are defined in terms of the COE as [34]

$$p = a\left(1 - e^2\right) \tag{3.11}$$

$$f = e\cos\left(\omega + \Omega\right) \tag{3.12}$$

$$g = e\sin\left(\omega + \Omega\right) \tag{3.13}$$

$$h = \tan\left(i/2\right)\cos\Omega \tag{3.14}$$

$$k = \tan\left(i/2\right)\sin\Omega \tag{3.15}$$

$$L = \Omega + \omega + \nu \tag{3.16}$$

where

$$p = \text{ semiparameter or semilatus rectum}$$

$$L = \text{ true longitude}$$

The usual terminology also defines $\varpi = \Omega + \omega$ as the longitude of periapsis and $\theta = \omega + \nu$ as the argument of latitude [3].

Equations 3.11-3.16 can be solved for the classical orbital elements in terms of the modified equinoctial elements to facilitate converting between the two element sets, as below

$$a = \frac{p}{1 - f^2 - g^2} \tag{3.17}$$

$$e = \sqrt{f^2 + g^2} \tag{3.18}$$

$$i = 2 \arctan\left(\sqrt{h^2 + k^2}\right) \tag{3.19}$$

$$= \arctan\left(2\sqrt{h^2 + k^2}, 1 - h^2 - k^2\right) \tag{3.20}$$

$$\omega = \arctan(g/f) - \arctan(k/h) \tag{3.21}$$

$$= \arctan(gh - fk, fh + gk) \tag{3.22}$$

$$\Omega = \arctan(k, h) \tag{3.23}$$

$$\nu = L - (\Omega + \omega) \tag{3.24}$$

$$= L - \arctan(g/f) \tag{3.25}$$

$$u = \omega + \nu \tag{3.26}$$

$$= \arctan(h \sin L - k \cos L, h \cos L + k \sin L) \tag{3.27}$$

where u is the argument of latitude [3] used in lieu of ν for circular orbits. In the equations above, expressions of the form $\arctan(a, b)$ indicate a four quadrant inverse tangent calculation, such as *atan*2 in MATLAB®.

In order to implement the MEE set in the two-body equations of motion, Battin derived the Cartesian position and velocity vectors in MEE coordinates. The MEE set is related to the earth-centered inertial (ECI), or Cartesian, radius and velocity vectors through the expressions [2]

$$\vec{r} = \begin{bmatrix} \frac{r}{s^2}\left(\cos L + \alpha^2 \cos L + 2hk \sin L\right) \\ \frac{r}{s^2}\left(\sin L - \alpha^2 \sin L + 2hk \cos L\right) \\ \frac{2r}{s^2}\left(h \sin L - k \cos L\right) \end{bmatrix} \tag{3.28}$$

$$\vec{v} = \begin{bmatrix} -\frac{1}{s^2}\sqrt{\frac{\mu}{p}}\left(\sin L + \alpha^2 \sin L - 2hk \cos L + g - 2fhk + \alpha^2 g\right) \\ -\frac{1}{s^2}\sqrt{\frac{\mu}{p}}\left(-\cos L + \alpha^2 \cos L + 2hk \sin L - f + 2ghk + \alpha^2 f\right) \\ \frac{2}{s^2}\sqrt{\frac{\mu}{p}}\left(h \cos L + k \sin L + fh + gk\right) \end{bmatrix} \tag{3.29}$$

where

$$\alpha^2 = h^2 - k^2 \tag{3.30}$$

$$s^2 = 1 + h^2 + k^2 \tag{3.31}$$

$$w = 1 + f \cos L + g \sin L \tag{3.32}$$

$$r = \frac{p}{w} \tag{3.33}$$

These equations yield the Cartesian state vector $(\vec{r}, \vec{v}) = (r_x, r_y, r_z, v_x, v_y, v_z)$ when supplied with the equinoctial coordinates (p, f, g, h, k, L). Betts noted that the inverse transformation (from Cartesian to MEE form) can be calculated, though for this case the true longitude L can only be found within a multiple of 2π. It must be resolved into an angle between 0 and 2π through knowledge of the reference epoch time [3].

Equations 3.11-3.16 are direct equations; they can be individually differentiated with respect to time to obtain the differential equations required for solving orbital problems (in terms of the

COE and their derivatives). Walker et al. used Lagrange's planetary equations

$$\frac{da}{dt} = \frac{-2a^2}{\mu}\frac{\partial \widetilde{R}}{\partial \tau} \tag{3.34}$$

$$\frac{de}{dt} = \frac{-a\left(1-e\right)^2}{\mu e}\frac{\partial \widetilde{R}}{\partial \tau} - \frac{1}{e}\sqrt{\frac{1-e^2}{\mu a}}\frac{\partial \widetilde{R}}{\partial \omega} \tag{3.35}$$

$$\frac{di}{dt} = \frac{1}{\sqrt{\mu a\left(1-e^2\right)}\sin i}\left(\cos i\frac{\partial \widetilde{R}}{\partial \omega} - \frac{\partial \widetilde{R}}{\partial \Omega}\right) \tag{3.36}$$

$$\frac{d\omega}{dt} = \sqrt{\frac{1-e^2}{\mu a}}\left(\frac{1}{e}\frac{\partial \widetilde{R}}{\partial e} - \frac{\cot i}{1-e^2}\frac{\partial \widetilde{R}}{\partial i}\right) \tag{3.37}$$

$$\frac{d\Omega}{dt} = \frac{1}{\sqrt{\mu a\left(1-e^2\right)}\sin i}\frac{\partial \widetilde{R}}{\partial i} \tag{3.38}$$

and, expressing the classical elements in terms of the modified equinoctial elements and performing the appropriate transformation of $\widetilde{R}\left(a,e,i,w,\Omega,t-\tau\right)$ into $\widetilde{R}\left(p,f,g,h,k,L\right)$, derived the Gaussian equations of motion

$$\dot{p} = \frac{2p}{w}\sqrt{\frac{p}{\mu}}\Delta_t \tag{3.39}$$

$$\dot{f} = \sqrt{\frac{p}{\mu}}\left[\Delta_r \sin L + \left[\left(w+1\right)\cos L + f\right]\frac{\Delta_t}{w} - \left(h\sin L - k\cos L\right)\frac{g\Delta_n}{w}\right] \tag{3.40}$$

$$\dot{g} = \sqrt{\frac{p}{\mu}}\left[-\Delta_r \cos L + \left[\left(w+1\right)\sin L + g\right]\frac{\Delta_t}{w} - \left(h\sin L - k\cos L\right)\frac{f\Delta_n}{w}\right] \tag{3.41}$$

$$\dot{h} = \sqrt{\frac{p}{\mu}}\frac{s^2\Delta_n}{2w}\cos L \tag{3.42}$$

$$\dot{k} = \sqrt{\frac{p}{\mu}}\frac{s^2\Delta_n}{2w}\sin L \tag{3.43}$$

$$\dot{L} = \sqrt{\mu p}\left(\frac{w}{p}\right)^2 + \frac{1}{w}\sqrt{\frac{p}{\mu}}\left(h\sin L - k\cos L\right)\Delta_n \tag{3.44}$$

where Δ_r, Δ_t and Δ_n are the non-two-body perturbation accelerations in the radial, tangential and normal directions, respectively. The convention for the radial direction is along the geocentric radius vector of the spacecraft (measured positive in the direction away from the geocenter); the tangential direction is perpendicular to the radius vector (measured positive in the direction of orbital motion); the normal direction is the positive direction along the angular momentum vector

of the satellite's orbit [3, 34], as defined in Equations 3.49-3.51 below. Betts mentions in his paper that Equation 3.41 reflects the derivation performed by Battin [2] and corrects an error presented in the original paper by Walker et al. [3, 34].

3.3 Equations of Motion

The modified equinoctial dynamics equations can be rearranged into matrix form [4], expressed as

$$\dot{\vec{y}} = \mathbf{A}\vec{\Delta} + \vec{b} \tag{3.45}$$

where

$$\mathbf{A} = \begin{bmatrix} 0 & \frac{2p}{w}\sqrt{\frac{p}{\mu}} & 0 \\ \sqrt{\frac{p}{\mu}}\sin L & \sqrt{\frac{p}{\mu}}\frac{1}{w}\left[(w+1)\cos L + f\right] & -\sqrt{\frac{p}{\mu}}\frac{g}{w}\left(h\sin L - k\cos L\right) \\ -\sqrt{\frac{p}{\mu}}\cos L & \sqrt{\frac{p}{\mu}}\frac{1}{w}\left[(w+1)\sin L + g\right] & \sqrt{\frac{p}{\mu}}\frac{f}{w}\left(h\sin L - k\cos L\right) \\ 0 & 0 & \sqrt{\frac{p}{\mu}}\frac{s^2\cos L}{2w} \\ 0 & 0 & \sqrt{\frac{p}{\mu}}\frac{s^2\sin L}{2w} \\ 0 & 0 & \sqrt{\frac{p}{\mu}}\left(h\sin L - k\cos L\right) \end{bmatrix} \tag{3.46}$$

and

$$\vec{b} = \begin{bmatrix} 0 & 0 & 0 & 0 & 0 & \sqrt{\mu p}\left(\frac{w}{p}\right)^2 \end{bmatrix}^{\mathrm{T}} \tag{3.47}$$

The total disturbing acceleration vector $\vec{\Delta}$ is given by

$$\vec{\Delta} = \Delta_r\hat{i}_r + \Delta_t\hat{i}_t + \Delta_n\hat{i}_n \tag{3.48}$$

which is expressed in a rotating radial coordinate frame whose principle axes are defined by

$$\hat{i}_r = \frac{\vec{r}}{\|\vec{r}\|} \tag{3.49}$$

$$\hat{i}_n = \frac{\vec{r} \times \vec{v}}{\|\vec{r} \times \vec{v}\|} \tag{3.50}$$

$$\hat{i}_t = \hat{i}_n \times \hat{i}_r = \frac{(\vec{r} \times \vec{v}) \times \vec{r}}{\|\vec{r} \times \vec{v}\| \|\vec{r}\|} \tag{3.51}$$

These are the unit vectors in the radial, normal and tangential directions, respectively. The 3×3 rotation matrix, $\mathbf{R}$, from the radial-tangential-normal (RTN) coordinate frame to the ECI coordinate frame is defined in terms of the unit position vectors in Equations 3.49-3.51 as

$$\mathbf{R} = \begin{bmatrix} \hat{i}_r & \hat{i}_t & \hat{i}_n \end{bmatrix} \tag{3.52}$$

For unperturbed two-body motion, $\vec{\Delta}$ is zero. The first five equations of motion then become $\dot{p} = \dot{f} = \dot{g} = \dot{h} = \dot{k} = 0$, indicating that all of the modified equinoctial elements except for the fast variable, L, are constant. It is also important to note that any perturbing forces can be included in $\vec{\Delta}$, given that they are rotated (if necessary) into the RTN coordinate frame. For a satellite in geosynchronous orbit, the three most influential perturbations are those caused by Earth oblateness, gravitational disturbances from secondary bodies and SRP [32].

3.3.1 Gravitational Disturbing Acceleration. Earth oblateness, which is sometimes referred to as simply the J2 perturbation when higher order zonal harmonics (as well as all sectorial and tesseral harmonics) are neglected (see Figure 3.2), induces periodic variations in all orbital elements (a, e, i, Ω, ω, M). Secular perturbations, however, are only induced by even zonal harmonics, and only affect Ω, ω and M [32]. For the purposes of this thesis, only the J2 perturbations will be modeled, as these have the most effect on a satellite within a geosynchronous orbit about the Earth. The models often used for determining the perturbing acceleration due to oblate body

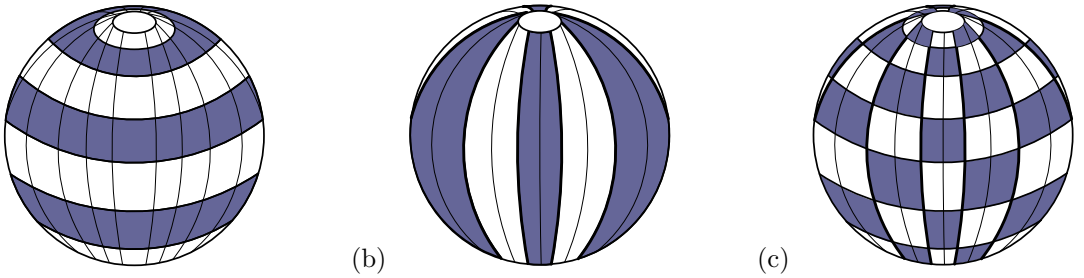

Figure 3.2: Disturbing Forces on the Gravity Field of a Central Body. The shaded regions in subfigures (a), (b) and (c) indicate areas of increased gravity.
(a) Zonal Harmonics. Zonal harmonics often coincide with the more massive latitudinal bands of the Earth (e.g., the equator). They account for most of the non-spherical Earth gravitational anomalies.
(b) Sectorial Harmonics. The sectorial harmonics, so called due to the resemblance to sections of an orange, correlate to longitudinal bands of increased mass (e.g., North-South running mountain ranges like the Rockies and Appalachians).
(c) Tesseral Harmonics. These harmonics represent specific regions on the Earth which depart from the perfect sphere model, e.g., Australia and Antartica.

effects are normally defined in a local horizontal reference frame. The non-spherical gravitational acceleration vector is given in this frame as

$$\vec{\delta g} = \delta g_N \hat{i}_N - \delta g_r \hat{i}_r \tag{3.53}$$

where $\hat{i}_N$ defines the unit vector in the local North direction

$$\hat{i}_N = \frac{\hat{e}_N - \left(\hat{e}_N^{\mathrm{T}} \hat{i}_r\right) \hat{i}_r}{\|\hat{e}_N - \left(\hat{e}_N^{\mathrm{T}} \hat{i}_r\right) \hat{i}_r\|} \tag{3.54}$$

with

$$\hat{e}_N = \begin{bmatrix} 0 & 0 & 1 \end{bmatrix}^{\mathrm{T}} \tag{3.55}$$

and $\hat{i}_r$ defines the unit radial direction component as given in Equation 3.49.

Ignoring the tesseral and sectorial harmonics, the general forms for the oblate Earth perturbations to the gravitational acceleration model (in the North and radial directions, respectively)

are

$$\delta g_N = -\frac{\mu_\oplus \cos\phi_{gc}}{r^2} \sum_{k=2}^{n} \left(\frac{R_\oplus}{r}\right)^k P'_k J_k \tag{3.56}$$

$$\delta g_r = -\frac{\mu_\oplus}{r^2} \sum_{k=2}^{n} (k+1) \left(\frac{R_\oplus}{r}\right)^k P_k J_k \tag{3.57}$$

where $\mu_\oplus$ is the Earth's gravitational constant, r is the geocentric distance to the satellite, $R_\oplus$ is the equatorial radius of the Earth, ϕ_{gc} is the geocentric latitude, J_k is the kth zonal harmonic coefficient and $P_k(\sin\phi_{gc})$ is the kth order Legendre polynomial with corresponding derivative P'_k. For a model that only includes zonal harmonics, the east component of the zonal gravity effects is exactly zero and can be set as such to generate a fairly accurate model [4, 5].

For J2 effects only, the perturbations to the gravitational acceleration are

$$\delta g_N = -\frac{\mu_\oplus \cos\phi_{gc}}{r^2} \left(\frac{R_\oplus}{r}\right)^2 P'_2 J_2 \tag{3.58}$$

$$\delta g_r = -\frac{\mu_\oplus}{r^2} \left[3 \left(\frac{R_\oplus}{r}\right)^2 P_2 J_2\right] \tag{3.59}$$

where Vallado [32] defines

$$J_2 = 0.0010826269 \tag{3.60}$$

$$P_2 = \frac{1}{2}\left(3\sin^2\phi_{gc} - 1\right) \tag{3.61}$$

The derivative of the Legendre polynomial is (note that there is also a $\cos\phi_{gc}$ term that has already been absorbed in Equation 3.58)

$$P'_2 = 3\sin\phi_{gc} \tag{3.62}$$

and the geocentric latitude is easily computed using the ECI position vector of the satellite

$$\phi_{gc} = \arctan\left(r_K, \sqrt{(r_I^2 + r_J^2)}\right) \tag{3.63}$$

where the I, J and K components of the radius vector are given as r_I, r_J and r_K respectively. The gravitational perturbation in the rotating radial reference frame, then, is achieved through a rotation by matrix $\mathbf{R}$

$$\vec{\Delta_g} = \mathbf{R}^{\mathrm{T}}\vec{\delta g} \tag{3.64}$$

3.3.2 Solar Radiation Pressure Perturbing Acceleration. Like atmospheric drag, SRP is a nonconservative non-gravitational disturbance. The SRP perturbing force increases in relative magnitude, however, as the effects of atmospheric drag decrease. In GEO, for example, the perturbing force due to atmospheric drag can be considered to be negligible, whereas SRP is the dominant perturbation at that altitude.

SRP perturbing acceleration is difficult to model for many reasons. Most models implement a constant solar flux, though solar flux in fact varies both throughout the year and during periods of solar activity. The variations associated with periods of increased solar activity cannot be accurately forecasted due to their sporadic tendencies, but the variations exhibited in solar flux are computationally insignificant for the purposes of this thesis (on the order of 7%) due to the larger ambiguities in surface characteristics.

For an accurate model, the cross-sectional areas of the satellite must also be computed with reasonable precision, and the Earth's shadowing effects on the satellite must be considered. Other difficulties arise in estimating the reflective properties of the satellite, as the composition of the satellite surfaces will directly affect how much force from SRP can be harnessed to produce incremental acceleration. The development of an accurate model also involves the ability to calculate the precise position of the Sun with respect to the satellite and the Earth at any given time during

the orbit, as well as the correct attitude of the satellite (and orbit) and the exact value of the SRP itself. Using this determination, the satellite can be reoriented with respect to the Sun at the proper positions to maximize (and in turn minimize) the components of the force vector in the unit normal direction.

To account for the yearly variance of the solar flux, Wertz developed a time-varying formula to replace the often-used solar flux constant $SF = 1353\ W/m^2$. His equation for the solar flux, below, uses a value measured from the Earth aphelion point, which can be obtained from tables in the *Astronomical Almanac*. An abbreviated form of the tables is presented in Appendix B [31]. $D_{aphelion}$ is defined as 2π times the number of days elapsed from Earth aphelion, as a fraction of the whole year.

$$SF = \frac{1358}{1.004 + 0.0334 \cos D_{aphelion}} \quad \frac{W}{m^2} \tag{3.65}$$

The change in momentum, or the force of the solar pressure per unit area p_{SR}, is defined in terms of the solar flux as

$$p_{SR} = \frac{SF}{c} \tag{3.66}$$

where c is the speed of light.

Most models for SRP perturbations do not include the complex surface geometry of a satellite. Satellite surfaces degrade with time while in orbit, and although reflective properties may have been known with relative accuracy at launch, over many years the coefficients will fluctuate drastically and models must be updated to reflect the true perturbing forces experienced by the satellite. To incorporate a more accurate picture of how the satellite behaves under perturbing forces from SRP, an algorithm must include both the absorption and reflection of a representative solar ray. Figure 3.3 illustrates the geometry involved when calculating the forces on the satellite due to SRP.

The two primary types of reflection, specular and diffuse, are illustrated in Figure 3.4. The solar radiation incident on the satellite surface area, as in Figure 3.3, shows the incident angle ϕ_{inc},

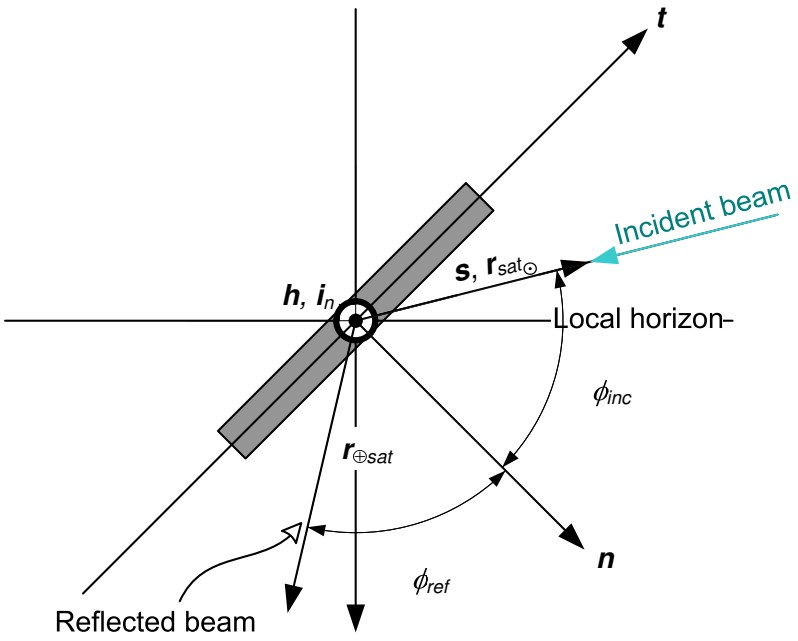

Figure 3.3: Incident Solar Radiation Geometry. Note that h and i_n are oriented upwards from the plane of the paper; s and $r_{sat\odot}$ are collinear with the incident solar ray. The unit vectors t and n are the unit vectors in the tangential and normal directions (with respect to the flat plate), respectively.

defined as the angle between the normal unit vector $\hat{n}$ and the unit vector defining the direction from the satellite to the Sun, $\hat{s}$. Note that the reflected angle, ϕ_{ref}, and the incident angle are equal for purely specular reflection [35].

Vallado derives a relationship for the perturbing acceleration by assuming a Lambertian diffusion (see Section 2.3.2) to model the diffuse and specular radiation forces as they affect the satellite. He uses a macro-model to sum each satellite surface area, as follows,

$$\vec{a}_{SR} = -\sum_{i=1}^{n} \frac{p_{SR} A_{\odot_i} \cos\phi_{inc_i}}{m} \left\{ 2 \left[\frac{c_{Rd_i}}{3} + c_{Rs_i} \cos\phi_{inc_i} \right] \hat{n} + (1 - c_{Rs_i})\, \hat{s} \right\} \tag{3.67}$$

where $A_{\odot_i}$ is the average effective cross-sectional area of surface i, m is the mass of the entire satellite, and c_{Rd_i} and c_{Rs_i} are the coefficients of diffuse and specular reflectivity, respectively [32]. Note that the coefficient of absorption is not explicitly needed, although it has been incorporated since $1 - C_{Rs} = C_{Ra} + C_{Rd}$. The surface normal unit vector $\hat{n}$ and the solar incidence unit vector $\hat{s}$ are required to specify the orientation of the satellite. A macro-model estimates the shape and orientation of the satellite to find a more accurate acceleration; the summation adds the contributions from the n flat plate surfaces of the satellite model, where each surface is the ith element.

For the case of a spin-stabilized satellite with one rotating platform and one despun platform, such as the DSCS II satellite, Equation 3.67 simplifies to (with $n = 2$)

$$\vec{a}_{SR} = -\vec{a}_{SR_d} - \vec{a}_{SR_s} \tag{3.68}$$

where d and s indicate the despun and spin-stabilized platforms, respectively, and

$$\vec{a}_{SR_d} = \frac{1}{m} p_{SR} A_{exp_d} \cos\phi_{inc_d} \left\{ 2 \left[\frac{c_{Rd_d}}{3} + c_{Rs_i} \cos\phi_{inc_d} \right] \hat{n}_d + (1 - c_{Rs_d})\, \hat{s}_d \right\} \tag{3.69}$$

$$\vec{a}_{SR_s} = \frac{1}{m} p_{SR} A_{exp_s} \cos\phi_{inc_s} \left\{ 2 \left[\frac{c_{Rd_s}}{3} + c_{Rs_i} \cos\phi_{inc_s} \right] \hat{n}_s + (1 - c_{Rs_s})\, \hat{s}_s \right\} \tag{3.70}$$

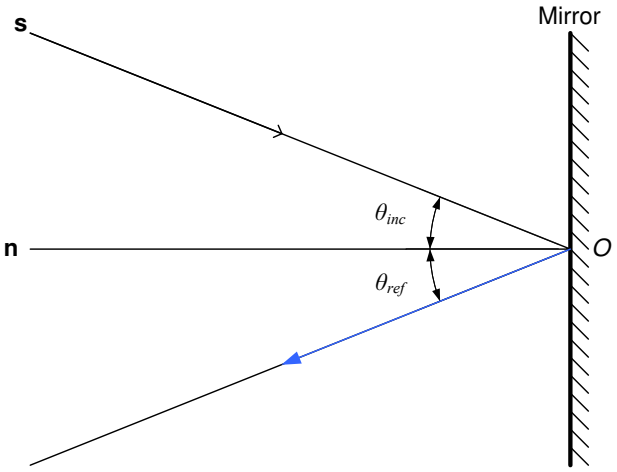

(a)

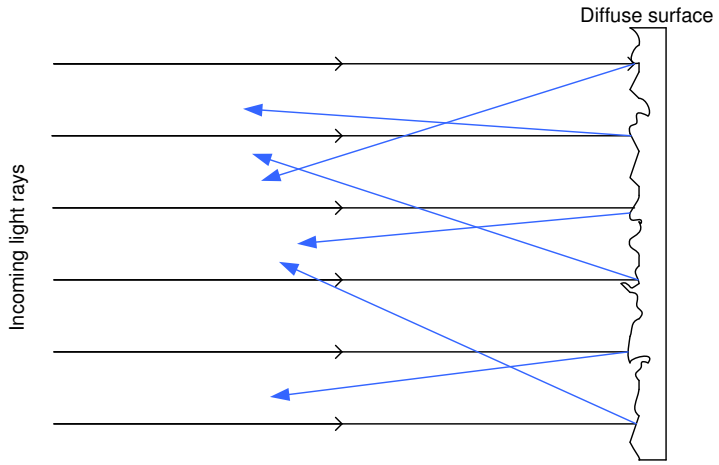

(b)

Figure 3.4: (a) Specular Reflection. A mirror-like reflection, specular reflection is often identified by the congruent angles the incoming and reflected waves make with the surface normal vector. (b) Diffuse Reflection. With this type of reflection, the wave bounces off of the reflecting surface at seemingly random angles, due to the surface irregularities.

The average effective cross-sectional areas, A_{exp_s} and A_{exp_d}, are approximated by flat plates (refer to Figure 3.5). For cylinders, this is a valid approximation, as the area as seen from the Sun will indeed be represented as a flat plate area. For the parabolic antennas on the DSCS II satellite's despun platform, flat plate approximations are used due to the ambiguity of the measurements available.

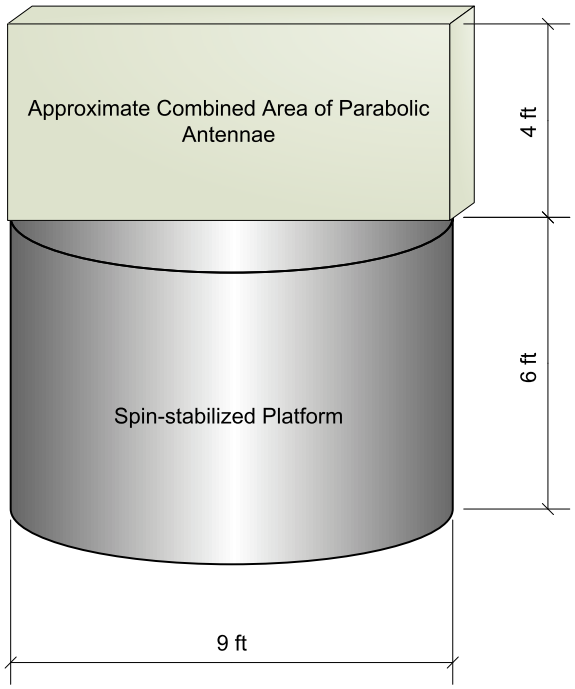

Figure 3.5: DSCS II F-13 Approximate Area Illustration. Although the despun platform approximate area is shown with some depth in the figure, for the purposes of this thesis it is assumed to have zero depth. The spin-stabilized platform is faced with solar panels.

Since the focus of the thesis is to raise the orbit of a geosynchronous satellite the most effectively (read: most quickly) with only SRP, it is also interesting to consider larger (at least conceptually) flat plate areas for the DSCS II parabolic antennae approximation. The motivation for this thesis is satellite disposal, and it is unlikely that very large solar sail-like devices would be used for this purpose. Therefore, only smaller areas are considered; the original flat plate approximated area (area factor equal to 1) will be multiplied by two different area factors: five and ten. The simulation will be repeated for each of these areas, and then the change in semimajor axis

will be plotted versus area factor (1, 5 and 10), as well as the time to disposal versus area factor. These plots should give an indication of how the satellite responds to the SRP perturbation with changing flat plate areas.

The coefficients of absorption and diffuse and specular reflectivities are also considered unknown values. The satellite used in the model has been in orbit since 1979, and the since the satellite surfaces have degraded over time, the current coefficients cannot be accurately estimated. For the purposes of this thesis, the coefficients (note that $c_{Ra} + c_{Rd} + c_{Rs} = 1$) have each been set to one-third unless noted. Several other test cases will also be simulated: all absorption ($c_{Ra} = 1$), all specular reflection (c_{Rs}), all diffuse reflection (c_{Rd}) and a blend of specular and diffuse reflection ($c_{Rd} = 0.5$ and $c_{Rs} = 0.5$). This will highlight the contribution of these types of reflection to the orbit raising solution.

Specific parameters regarding the DSCS II satellite, including the TLE set used for orbit propagation, can be found in Appendix A [23].

The unit vector defining the direction from the satellite to the Sun at any given time, $\hat{s}$, can be computed through

$$\hat{s} = \frac{\vec{r}_{sat\odot}}{\|\vec{r}_{sat\odot}\|} \tag{3.71}$$

where $\vec{r}_{sat\odot}$ is the vector from the satellite to the Sun. From Figure 3.6, it is evident that $\vec{r}_{sat\odot}$ is simply the sum of two vectors

$$\vec{r}_{sat\odot} = \vec{r}_{\oplus\odot} - \vec{r} \tag{3.72}$$

where $\vec{r}_{\oplus\odot}$ is the Earth-Sun vector and $\vec{r}$ is the ECI position vector of the satellite.

The Earth-Sun vector, at any given time t, is calculated using an algorithm from Vallado's text. Given the current Julian date, the number of Julian centuries is calculated as

$$T_{TDB} = \frac{JD - 2451545.0}{36525} \tag{3.73}$$

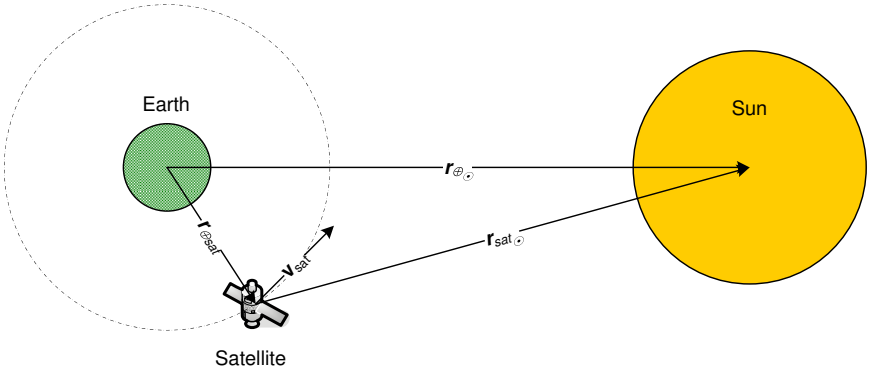

Figure 3.6: Earth-Satellite-Sun Vector Diagram. The bodies and distances in the figure are not to scale; they are positioned for purposes of clarity. The plane of the ecliptic is assumed congruent with the plane of the paper.

where T_{TDB} references the number of Julian centuries based on barycentric dynamical time (TDB).

Using the number of Julian centuries, the mean longitude of the Sun $\lambda_{M_\odot}$, solar mean anomaly $M_\odot$, ecliptic longitude λ_{ecl}, distance between the Earth and the Sun $r_{\oplus\odot}$ and the obliquity of the ecliptic ϵ are calculated from the equations

$$M_\odot = 357.5277233^o + 35999.05034\ T_{TDB} \tag{3.74}$$

$$\lambda_{M_\odot} = 280.460^o + 36000.770\ T_{TDB} \tag{3.75}$$

$$\lambda_{ecl} = \lambda_{M_\odot} + 1.914666471 \sin(M_\odot) + 0.019994643 \sin(2M_\odot) \tag{3.76}$$

$$r_{\oplus\odot} = 1.000140612 - 0.016708617 \cos(M_\odot) - 0.000139589 \cos(2M_\odot) \tag{3.77}$$

$$\epsilon = 23.439291 - 0.0130042\ T_{TDB} \tag{3.78}$$

The ecliptic latitude of the Sun is never greater than 0.000333^o, and is set to zero for this problem without much loss of accuracy. The Earth-Sun vector, in Astronomical Units (AU), is

$$\vec{r}_{\oplus\odot} = r_{\oplus\odot} \begin{bmatrix} \cos(\lambda_{ecl}) \\ \cos(\epsilon) \sin(\lambda_{ecl}) \\ \sin(\epsilon) \sin(\lambda_{ecl}) \end{bmatrix} \tag{3.79}$$

To convert from AU to kilometers, multiply Equation 3.79 by 149598000 [32].

The parameters for the satellite's rotating platform to use in Equation 3.70 are easily computed. The DSCS II's spinning platform is of cylindrical shape; the reflected or incident angle of the cylinder is always $\phi_s = 0$ since the face of the cylinder will always be perpendicular to $\hat{s}$. Subsequently, the unit normal vector $\hat{n}$ will always lie along $\hat{s}$.

The computation of the unit normal vector for the despun platform is more complicated. Because the parabolic antennae are not cylindrical, as the satellite changes its attitude, the effective cross-sectional area presented to the Sun also changes. The control algorithm illustrated in Section 3.4 outlines several methods for calculating $\hat{n}$ for the parabolic antennae.

3.3.3 Solar Gravitational Perturbations. For a satellite orbiting the Earth, the magnitudes of the perturbations caused by the effects of gravitational attraction from a third body (e.g., Sun or Moon) become greater as the altitude of the orbit increases. The third-body effects, as they are termed, become noticeable as the effects of atmospheric drag subside; they are, in fact, the largest perturbations affecting satellites in geosynchronous orbit. The primary third-body gravitational perturbing forces acting on a satellite in geosynchronous orbit are those from the Sun and Moon, although the Moon's perturbations will not be considered due to the complexity of the calculations and the associated processing time. Since the Moon does not induce secular changes in semimajor axis of the orbit, this exclusion does not diminish the results.

In a geosynchronous orbit, the disturbances caused by the Sun can have a significant long-term perturbing effect on the orbit. Vallado lists the main effect as a regression of the satellite's orbital plane about an axis normal to the Sun's orbital plane. The only secular perturbations caused by the solar gravitational perturbation appear in the node and perigee. The expected long-periodic variations in e, i, Ω and ω are entirely due to the regression of the satellite's perigee and the motion of the Earth about the Sun. When modelled perfectly, the Sun causes no secular, long-periodic

or m-monthly variations in semimajor axis, the parameter of most interest in this thesis [32]. To generate a more complete model, however, these third-body perturbations will be included.

The equations used to calculate the perturbing acceleration from the Sun are nearly identical to the previous section. The equation of motion for a three-body system (in this section, the Earth-Sun-satellite system) is given by

$$\ddot{\vec{r}}_{\oplus sat} = -\frac{\mu_{\oplus}\vec{r}_{\oplus sat}}{r^3_{\oplus sat}} + \mu_{\odot}\left(\frac{\vec{r}_{sat\odot}}{r^3_{sat\odot}} - \frac{\vec{r}_{\oplus\odot}}{r^3_{\oplus\odot}}\right) \tag{3.80}$$

where the perturbing acceleration due to the Sun is isolated as

$$\overrightarrow{\delta q}_{\odot} = \mu_{\odot}\left(\frac{\vec{r}_{sat\odot}}{r^3_{sat\odot}} - \frac{\vec{r}_{\oplus\odot}}{r^3_{\oplus\odot}}\right) \tag{3.81}$$

and where $\mu_{\odot}$ is the gravitational parameter of the Sun, $\vec{r}_{sat\odot}$ is the position vector from the satellite to the Sun and $\vec{r}_{\oplus\odot}$ is the position vector from the Earth to the Sun (the calculation of which is presented in Equations 3.74-3.79).

Although at this point the equation could be numerically integrated, closer study yields a potential problem. The distances from the satellite to the Sun and the Earth to the Sun are very similar and thus the value in the parenthesis will be very small. It is possible that this could induce errors during a numerical integration of the equation, unless the capability exists to store large numbers of significant figures (which would significantly lengthen the time required for integration). A series expansion of $r^{-3}_{sat\odot}$ yields a more numerically stable solution of

$$\overrightarrow{\delta q}_{\odot} = -\frac{\mu_{\odot}}{r^3_{\oplus\odot}}\left(\vec{r}_{\oplus sat} - 3\vec{r}_{\oplus\odot}\frac{\vec{r}_{\oplus sat}\cdot\vec{r}_{\oplus\odot}}{r^2_{\oplus\odot}} - 15\vec{r}_{\oplus\odot}\left(\frac{\vec{r}_{\oplus sat}\cdot\vec{r}_{\oplus\odot}}{r^2_{\oplus\odot}}\right)^2\right) \tag{3.82}$$

where an expansion of three terms for the solar perturbation case is sufficiently accurate [32].

The perturbing acceleration in the rotating radial reference frame is [5]

$$\vec{\Delta}_{q_\odot} = \mathbf{R}^{\mathrm{T}} \overrightarrow{\delta q}_\odot \tag{3.83}$$

3.4 Control Algorithm

If left to drift uncontrolled, a satellite in geosynchronous orbit will experience only periodic motion in the semimajor axis due to SRP perturbations [32]. This is due to the Earth's rotation around the Sun; for one-half of the orbit, SRP acts to add a Δv to the perigee of the satellite's orbit and subtract a Δv from the apogee, thus causing the orbit to gradually become elliptic. For the remaining six months of Earth's orbit, SRP causes the satellite to experience the opposite reaction: a Δv is subtracted from the perigee and added to the apogee, circularizing the satellite's orbit again (see Figure 3.7 for further clarification). The purpose of this thesis, however, is to harness the SRP perturbing acceleration and raise the orbit of a satellite into an appropriate disposal orbit (the guidelines of which can be found in Appendix D). To raise the orbit of a satellite the most effectively with respect to time, a host of different methods could be implemented. Two methods will be addressed, the first of which is a controller that would only require attitude changes twice daily. The second is a more complex algorithm that continuously changes the satellite's attitude. Both methods require only electrical power to be implemented, which for the DSCS II is provided by the available solar arrays mounted on the spin-stabilized platform.

3.4.1 Simple Controller. Perhaps the simplest control algorithm is one based on the trigonometrics of the orbital problem. Using the diagram in Figure 3.8, it is evident that the cosine of the angle θ can be computed using the equation

$$\cos\theta = \frac{\vec{r}_{sat\odot} \cdot \vec{v}_{sat}}{\|\vec{r}_{sat\odot}\| \|\vec{v}_{sat}\|} \tag{3.84}$$

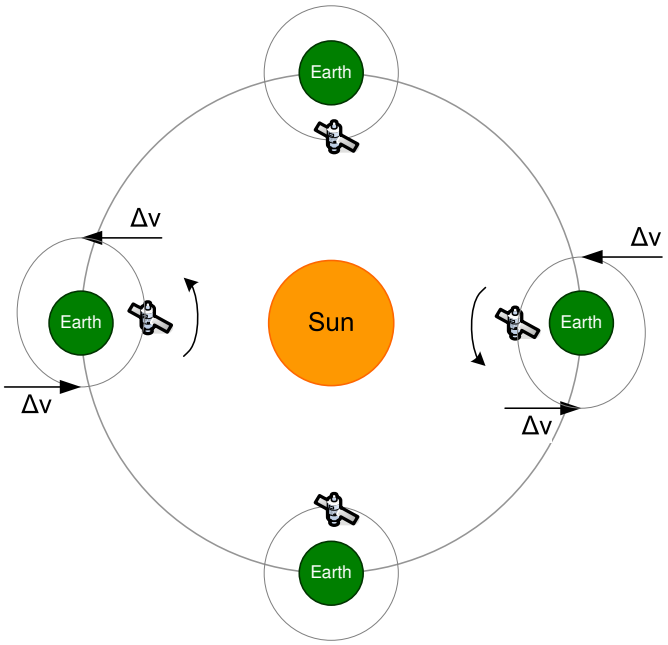

Figure 3.7: The Behavior of a Geosynchronous Satellite Over One Year Under the Long-Periodic Changes in Semimajor Axis Due to SRP.

If $\cos\theta$ is negative, the satellite is moving away from the Sun; if it is positive, the satellite is moving toward the Sun. The control algorithm computes $\cos\theta$, and if negative, positions the parabolic antennae perpendicular to $r_{\oplus\odot}$, thus maximizing the SRP perturbation addition to the acceleration and raising the orbit. This sets the effective area to its maximum value (for DSCS II, approximately 3.3528 m^2). If positive, the controller positions the antenna platform parallel to $r_{\oplus\odot}$ to minimize the SRP perturbation contribution. This, in effect, "turns off" the SRP for half of the satellite's orbit, permitting the orbit raising to dominate instead of being cancelled out by the orbit lowering. In the code, the thickness of the flat plate area is approximated to be 0 m; this sets the antenna area to 0 m^2.

The main advantage to a simplified control algorithm is less operator intervention. For an older satellite already in orbit, such as DSCS II, there is no realistic opportunity to install a complex controller or to reprogram the onboard computer. Thus, feedback from the operators suggests that a satellite operator would manually need to change the satellite's attitude for every re-orientation

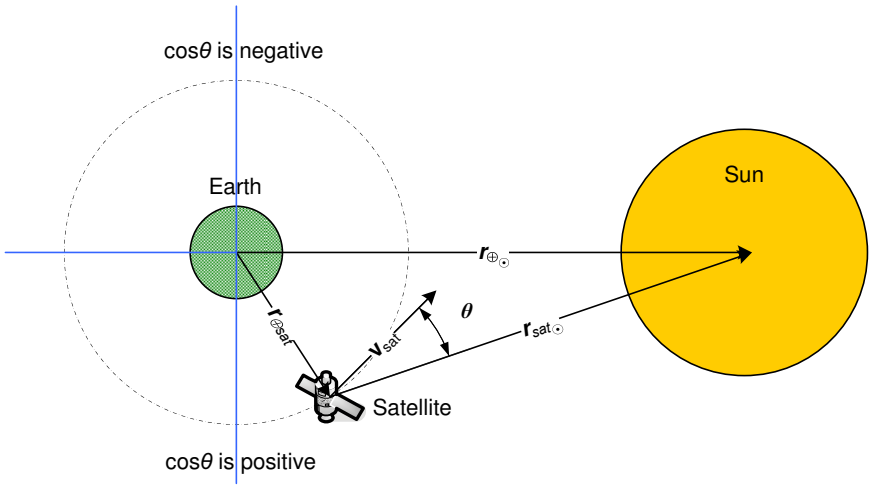

Figure 3.8: Simple Controller Diagram. Note that this diagram is not to scale. Cosine is negative above the horizontal axis, which is defined by $r_{\oplus\odot}$, and is positive below the horizontal axis.

required (certainly tedious). This twice-daily algorithm is one that would result in the least amount of operator hours spent raising the orbit.

The downside of the simple controller is directly related to its advantageous feature of less operator oversight. If changing the attitude of the satellite twice per orbit gleans a moderate change in semimajor axis, it follows that the more reorientations performed over one orbit, the more resulting change in semimajor axis. For this reason, a more complex controller will be studied, one that constantly reorients the satellite to maximize the change in semimajor axis.

3.4.2 Complex Controller. For newer satellites, or satellites yet to be launched or developed, there are many other possible control algorithms that would be able to raise the orbit of a satellite more quickly than the simple algorithm in Section 3.4.1.

Coverstone and Prussing [11] derived a sail force algorithm that forces the unit normal vector, $\hat{n}$, to maximize the rate of orbital energy, $\dot{E}$. Their controller continuously orients the sail (in three dimensions) to maximize the component of the sail force along the satellite's velocity vector, $\vec{v}$. This, in turn, maximizes the instantaneous rate of increase of the total orbital energy. The authors' full

derivation can be found in their journal article; however, it is worth discussing the highlights of the algorithm and the changes implemented for this thesis.

Coverstone and Prussing made several simplifying assumptions in their algorithm that contradict the desired model for this thesis. They derive a simplified perturbing acceleration model in which they assume a constant solar flux and only specular reflection. They introduce an acceleration vector that has no component in the satellite-Sun direction, indicating that they have neglected the forces due to diffuse reflection and absorption. The simplified acceleration is given as

$$\begin{aligned} \vec{S} &= \frac{2WA}{mc}\left(\hat{n}^{\mathrm{T}}\hat{\alpha}\right)^2\hat{n} \\ &= S_o\left(\hat{n}^{\mathrm{T}}\hat{\alpha}\right)^2\hat{n} \end{aligned} \tag{3.85}$$

where W is the constant solar intensity (flux) at 1 AU, A is the sail area, c is the speed of light, $\hat{n}$ is the unit normal vector to the sail and $\hat{\alpha}$ is the unit vector in the direction of the Sun. Using Equation 3.85, the authors derive the equation for the time rate of change of the orbital energy as

$$\dot{E} = \vec{S}^{\mathrm{T}}\vec{v} + \vec{g}_{\odot}^{\mathrm{T}}\vec{v} \tag{3.86}$$

where $\vec{g}_{\odot}$ is the gravitational perturbation of the Sun. The authors note, at this point in their derivation, that their solution is not precisely the minimum time solution, although for low acceleration rates (as in this thesis, with a very small "sail") their solution approaches the minimum time solution. They concede that for many applications, a shorter-duration solution may be achieved, however, since no propellant is being used, having the real minimum-time trajectory is probably not a critical issue.

To maximize the orbital energy, the authors orient the sail such that the expression $\vec{S}^{\mathrm{T}}\vec{v}$ is maximized in Equation 3.86 above. In other words, this will maximize the component of the sail acceleration along the instantaneous velocity vector at each point in the trajectory. In the

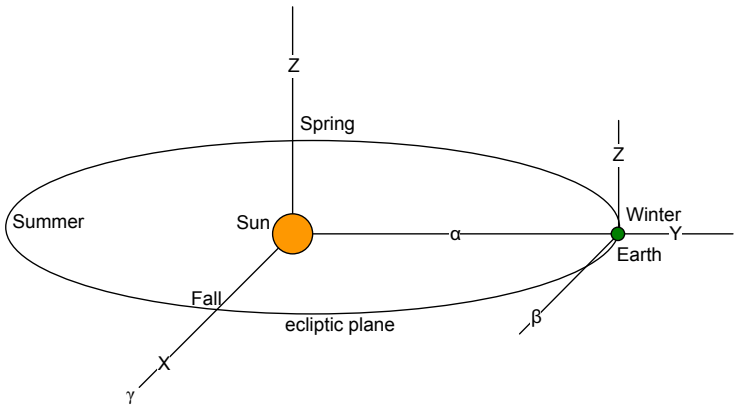

Figure 3.9: $\alpha\beta Z$ Axis Definitions. Note that Coverstone et al. assume the heliocentric Z-axis is collinear with the $\alpha\beta Z$ Z-axis.

derivation, the components of the unit normal vector $\hat{n}$ that result in the maximization of $\dot{E}$, in an $\alpha\beta Z$ reference frame (see Figure 3.9), are

$$n_\alpha = \frac{-|v_\beta|}{\sqrt{v_\beta^2 + \xi\left(v_\beta^2 + v_z^2\right)}} \tag{3.87}$$

$$n_\beta = \xi n_\alpha \tag{3.88}$$

$$n_z = \frac{v_z}{v_\beta} n_\beta \tag{3.89}$$

where

$$\xi = \frac{-3v_\alpha v_\beta - v_\beta\sqrt{9v_\alpha^2 + 8\left(v_\beta^2 + v_z^2\right)}}{4\left(v_\beta^2 + v_z^2\right)} \tag{3.90}$$

and v_α and v_β are rotated into the $\alpha\beta z$ reference frame through a rotation

$$\begin{bmatrix} v_\alpha \\ v_\beta \\ v_z \end{bmatrix} = \begin{bmatrix} \cos\Psi & \sin\Psi & 0 \\ -\sin\Psi & \cos\Psi & 0 \\ 0 & 0 & 1 \end{bmatrix} \begin{bmatrix} v_x \\ v_y \\ v_z \end{bmatrix} \tag{3.91}$$

where Ψ is the celestial longitude of the Sun [11].

The algorithm used in this thesis differs from this point forward. Coverstone and Prussing, in deriving their algorithm, neglected the effect of the inclination of the Earth's axis with respect to the ecliptic plane (approximately 23.5^o). For the purposes of this thesis, an additional rotation is performed between the ECI and heliocentric (XYZ) reference frames. Using the ecliptic latitude from Equation 3.76, the rotation matrix from the ECI frame to the XYZ frame is

$$\mathbf{R}_{XYZECI} = \begin{bmatrix} 1 & 0 & 0 \\ 0 & \cos 23.5 & \sin 23.5 \\ 0 & -\sin 23.5 & \cos 23.5 \end{bmatrix} \tag{3.92}$$

Then, $\vec{v}$ in the heliocentric frame is

$$\vec{v}_{XYZ} = \mathbf{R}_{XYZECI}\vec{v} \tag{3.93}$$

and in the $\alpha\beta Z$ frame,

$$\vec{v}_{\alpha\beta Z} = \begin{bmatrix} \cos\lambda_{ecl} & \sin\lambda_{ecl} & 0 \\ -\sin\lambda_{ecl} & \cos\lambda_{ecl} & 0 \\ 0 & 0 & 1 \end{bmatrix} \vec{v}_{XYZ} \tag{3.94}$$

Once the components of the unit normal vector in the $\alpha\beta Z$ frame are computed using Equations 3.87-3.89, the desired $\hat{n}$ is then rotated back to the ECI frame using the transposes of the matrices in Equations 3.92 and 3.94. Note that to implement the authors' equations with Vallado's algorithm for the perturbing SRP acceleration, the negative of Coverstone and Prussing's unit normal vector must be used. This puts the measurement of ϕ_{inc} in the same frame as Vallado, between the unit normal $\hat{n}$ and the unit vector in the satellite-Sun direction $\hat{s}$ versus between the acceleration vector in Equation 3.85 and the negative of the satellite-Sun vector.

The appropriate ϕ_{inc} for the despun platform is calculated using the following relationship

$$\phi_{inc} = \arccos\left(\hat{n} \cdot \hat{s}\right) \tag{3.95}$$

and the calculations for the SRP perturbing accelerations resume at Equation 3.68.

3.5 Earth Shadow Effects

Over long periods of time, it has been determined that Earth's shadow plays a secular role in the perturbation of a satellite's orbit [7,10]. As stated in Chapter II, the inclusion of such a shadow function in this thesis is particularly necessary, primarily due to the desire to raise the semimajor axis of an orbit. Bryant declared, in 1961, that the addition of an accurate shadow function to an orbital propagation algorithm would in fact result in a (positive) secular change in semimajor axis. Without the model of Earth's shadow, the SRP perturbing acceleration would only direct periodic changes in the semimajor axis [7].

Two particular categories of shadow functions exist: a simplified cylindrical model, as in Ferraz Mello's model [12], and a conical model, such as that presented by Kabelac. While the conical method is more accurate, it is often difficult to implement [16]. Kabelac's model, in particular, uses a more realistic conical Earth shadow with two main regions, the penumbra and umbra (see Figure 3.10 [32]). The umbra is the region that is in total eclipse by the Earth (or other primary body for applications with any planetary body), and the penumbra encompasses the region only partially eclipsed by the Earth or other primary body. The model also accounts for the mutual position of the Sun, Earth and satellite, the shape of conical surface, light diffusion, atmospheric absorption and the effect of ozone [16].

Ferraz Mello's model, however, approximates the Earth's shadow as a cylinder, and hence has only one region (see Figure 3.11 [32]). This approximation stems from an assumption that the Sun is at an infinite distance from the Earth. His algorithm, while greatly simplified from Kabelac's,

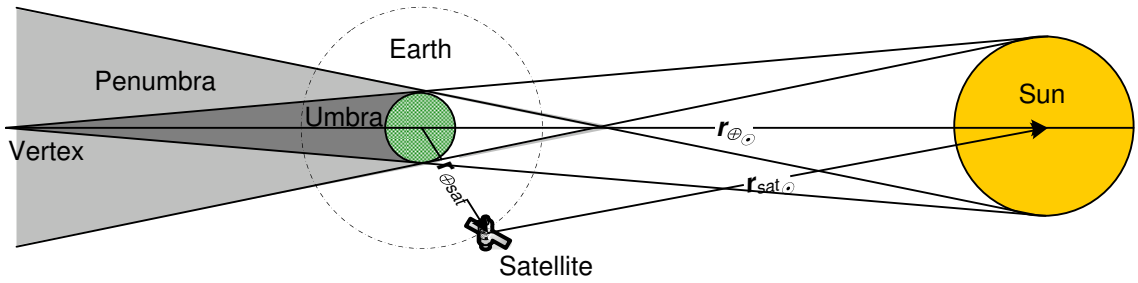

Figure 3.10: Eclipse Geometry with Penumbra and Umbra Regions. The penumbra is the lighter gray region and the umbra is the dark gray region. The figure is looking down onto the ecliptic plane; it is not to scale.

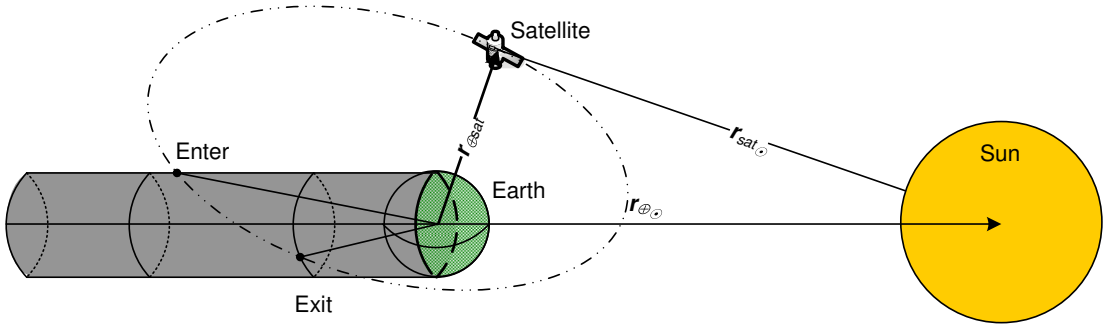

Figure 3.11: Cylindrical Eclipse Geometry. The Sun is approximated as a point source, hence the shadow cast by the Earth is cylindrical in shape instead of conical. The figure is not to scale, and the satellite orbit is not intended to approximate the orbit of DSCS II.

enables the user to include a shadow model without significant loss of accuracy. Kabelac states, in his paper, that his model differs only on the order of 0.1% to 1% in the orbital elements [12, 16]. A version of Ferraz Mello's model is used in this thesis.

The portion of the orbit when a satellite is fully inside the cylindrical shadow region of the Earth is of most interest. When an orbiting object is in the Earth's shadow, the SRP perturbing acceleration has no effect on the orbit of the satellite; the eclipsed satellite is not exposed to SRP due to obstruction from the Earth. Vallado derived an algorithm to determine if two objects have line of sight, and this can be directly applied to the shadow problem. The algorithm can be used to

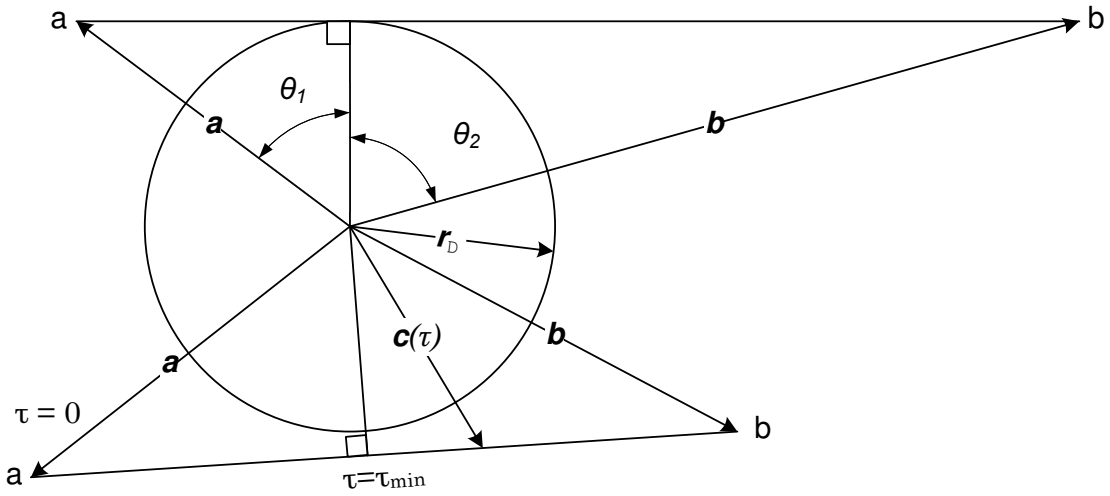

Figure 3.12: Geometry of τ_{min}. Line of Sight exists between the two positions a and b if the sum of the two angles is larger than the calculated value for θ (the angle between the two vectors). The parametric approach, in which the location for the minimum distance to the Earth is found, can also be used; each vector can be represented as a function of τ [32].

determine if the satellite has a direct line of sight with the Sun, and hence whether it is in Earth's shadow. Vallado assumes in his derivation that the light from the Sun acts as a point source. He derives a minimized parametric value, τ_{min}, that minimizes the distance to the central body (see Figure 3.12 for an illustration of the geometry involved in the definition of τ_{min})

$$\tau_{min} = \frac{|\vec{r}_1|^2 - \vec{r}_1 \cdot \vec{r}_2}{|\vec{r}_1|^2 + |\vec{r}_2|^2 - 2\vec{r}_1 \cdot \vec{r}_2} \tag{3.96}$$

Next, he derives a parametric representation of a line between the two position vectors $\vec{r}_1$ and $\vec{r}_2$, and substitutes the minimum parametric value τ_{min} to get

$$|\vec{c}(\tau_{min})|^2 = \frac{(1 - \tau_{min})\,|\vec{r}_1|^2 + (\vec{r}_1 \cdot \vec{r}_2)\,\tau_{min}}{R_\oplus^2} \tag{3.97}$$

The radius of the Earth squared, $R_\oplus^2$, in km, is present in the denominator to ensure (if $\vec{r}_1$ and $\vec{r}_2$ are in units of km) that the value of the parametric function is in units of Earth radians [32]. Implementing the algorithm in the orbit propagation code requires an if statement within MATLAB®.

A summarized version is presented below; the complete algorithm can be found in Appendix C.

$$
\begin{aligned}
&\text{if} \quad \tau_{min} < 0.0 \quad \text{or} \quad \tau_{min} > 1.0 \\
&\qquad \text{the satellite is illuminated} \\
&\text{elseif} \quad |\vec{c}(\tau_{min})|^2 \geq 1.0 \\
&\qquad \text{the satellite is illuminated} \\
&\text{else} \\
&\qquad \text{the satellite is not illuminated}
\end{aligned} \tag{3.98}
$$

If the satellite is illuminated, the SRP perturbing acceleration algorithm is applied; conversely, if the satellite is not illuminated, the SRP perturbing acceleration vector is set to zero.

IV. Results

Each set of results in this chapter includes one of three controllers: no controller, the simple control algorithm or the complex controller. All results include a cylindrical Earth shadow model, and the perturbations caused by third-body gravitational acceleration, oblate Earth (J2) and SRP. They incorporate Vallado's most sophisticated SRP perturbation algorithm with varying solar flux and the inclusion of absorption and reflection coefficients (Equation 3.67). Three individual areas were considered for the despun platform: the original area (reference Section 3.3.2 for a description of how this value was estimated), the original area multiplied by a factor of five and the original area multiplied by a factor of ten. Unless explicitly noted, the results (a tabular summary of which can be found in Section 4.7) presented use the original area. It is also important to note that in all the plots throughout this chapter, "time" on the x-axis indicates the time (in seconds) elapsed since epoch, as defined in Section 3.1.

4.1 Baseline Case

The baseline case, one with no active controller to reorient the satellite to maximize SRP effects, is an interesting one for purposes of comparison. Essentially, the satellite is drifting around the Earth freely in a nominal state, that is, without manual reorientation. Thus, one would expect the satellite to maintain a circular orbit without secular changes in semimajor axis, much like the two-body problem. Additionally, the perturbations should generate only periodic variations in e and i, and both secular and periodic changes in ω, Ω and ν.

The following plots are the results for the DSCS II F-13 satellite with no controller, i.e. the apparent area of the despun platform is set to zero, and the projected area of the spin-stabilized platform is set to its maximum of 5.0168 m^2.

Validation results for the baseline cases (of 1, 100 and 1000 orbits), propagated with Satellite Tool Kit (STK), are also presented in this section. This effort was requested by SMC Det 12 to

determine if the MATLAB® code developed by the author yielded reasonable results as compared to a "known" solution from trusted source (e.g. STK). The other cases in the thesis were unable to be generated in STK for purposes of validation, due primarily to the use of controllers.

The area factor referenced in Section 3.3.2 only affects the flat-plate area (despun platform apparent area); the results for varying areas will yield the same results as the original despun platform area, as this is set to zero for all the baseline cases. Note also that any changes in values for the absorption and specular and diffuse reflection coefficients will not affect the solution, as these are also multiplied by the despun platform area (zero for the baseline case) in Equation 3.67. To avoid duplication, therefore, only one set of plots will be generated for each of the three baseline cases, and no further baseline plots will be included in the sections to come.

To verify that the thesis results for the baseline cases are indeed reasonable, the satellite's motion was propagated in STK for each case. For purposes of comparison, the HPOP propagator was used to simulate the orbit with the same perturbations as considered in the thesis. For the Earth gravity, the model JGM2.grv was chosen, with a maximum degree of 2 and a maximum order of 0. Solar radiation pressure was implemented with a coefficient of reflection of $Cr = 1$ (corresponding to all specular reflection), an area-to-mass ratio of 0.00821604 m^2/kg, and a cylindrical shadow model. The gravitational perturbations due to the Sun were also included. Atmospheric drag, tides and all other gravitational bodies were excluded.

Figures 4.1-4.5 highlight the characteristics of the DSCS II's first orbit from epoch. Figures 4.1 and 4.2 depict the behavior of the ECI position and velocity vectors as the satellite orbits once around the Earth. Figure 4.1 illustrates the periodic motion of the x, y and z components of the ECI position and velocity vectors. As would be expected for a circular orbit, the z components exhibit very little change.

Although the two-dimensional orbit trace in Figure 4.2 appears circular at first glance, it is in fact slightly elliptical ($e_o = 0.00056$). The graph is a plot of of the x and y components of the ECI

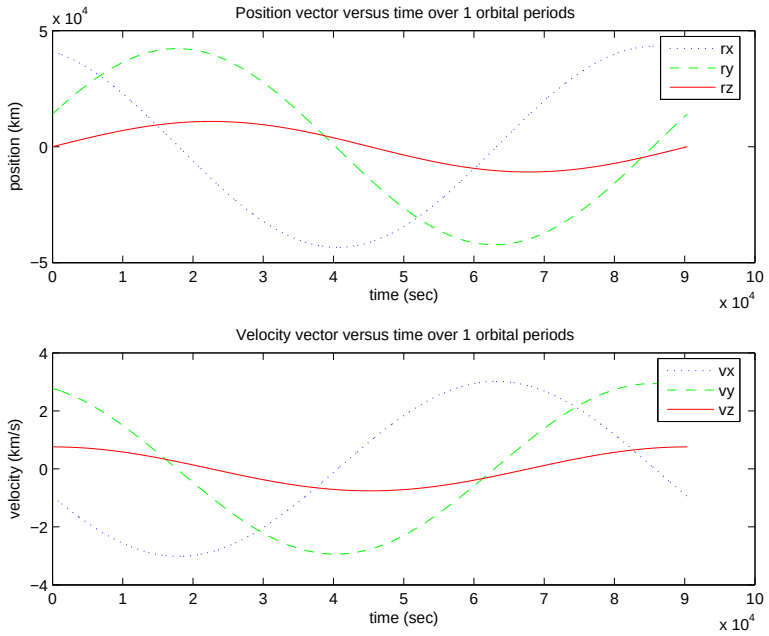

Figure 4.1: ECI Position and Velocity Vectors Versus Time over One Orbit.

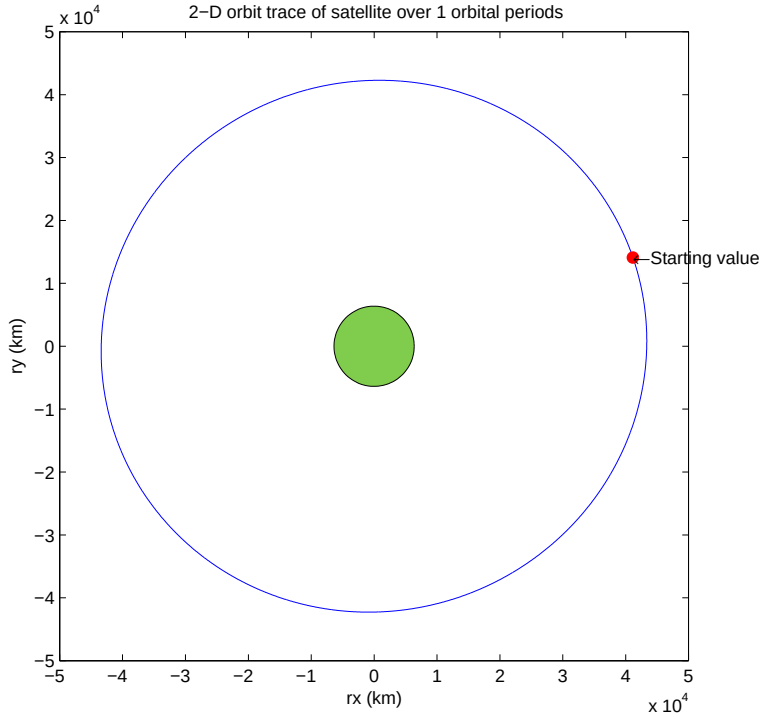

Figure 4.2: The Two-dimensional Orbit Trace over One Orbit. The starting position of the satellite (at epoch) is indicated by a filled circle labeled by "Starting value" on the right side of the graph.

position vector, and as such is "looking down" on the equatorial plane of the Earth (represented as the filled circle in the center of the figure).

Figures 4.3 and 4.4, depict the behavior of i, a and e over the corresponding time period. The inclination of the initial orbit oscillates around the epoch value of 14.4995^o. For satellites in a geosynchronous orbit, i drifts to about 15^o over the course of about 27 years [32], so one would expect that an inclination in the range of 0^o to 15^o is a realistic value. The periodic motion in i is common; perturbations due to zonal harmonics, drag, third-bodies and SRP all cause short or long periodic tenancies in inclination [32].

In this thesis, all secular changes in the satellite's semimajor axis are a direct result of the controller usage. For low Earth orbit, conversely, the drag perturbations induce secular changes in a. The changes in semimajor axis (Δa) throughout the chapter, excluding the Δa indicated in Figures 4.3, 4.6 and 4.8, which are simply the mean values over the integration time, are calculated using the polyfit function in MATLAB®. It is important to note that the polyfit function becomes more accurate as the number of periodic cycles increases, and hence the values given by the function for one orbit are not necessarily the most accurate representation of the change in semimajor axis. The apparent change exhibited in Figure 4.3 is a result of the short period (high frequency) oscillations (from the J2, third-body and SRP perturbations [32]) affecting the mean value calculation. Similarly, the apparent secular change in eccentricity is solely a factor of the short- and long-periodic variations caused by those perturbations. No additional plots of e, i, ω, Ω or ν will be included in beyond this section, as the semimajor axis is the parameter of interest.

Figure 4.3 illustrates one orbit propagated with STK overlaid on one orbit from the MATLAB® code results. The STK results are very similar to the thesis results as would be expected, however, the inherent differences found between the method STK uses to propagate an orbit and the methods presented in this thesis will yield slightly different answers. The mean values of the satellite's semimajor axis are labeled on the first subplot for each method. These are a serviceable indication

of the comparative methods, but the more interesting statistics, the difference between the vectors at each time step (deviation) are given in subplot 2.

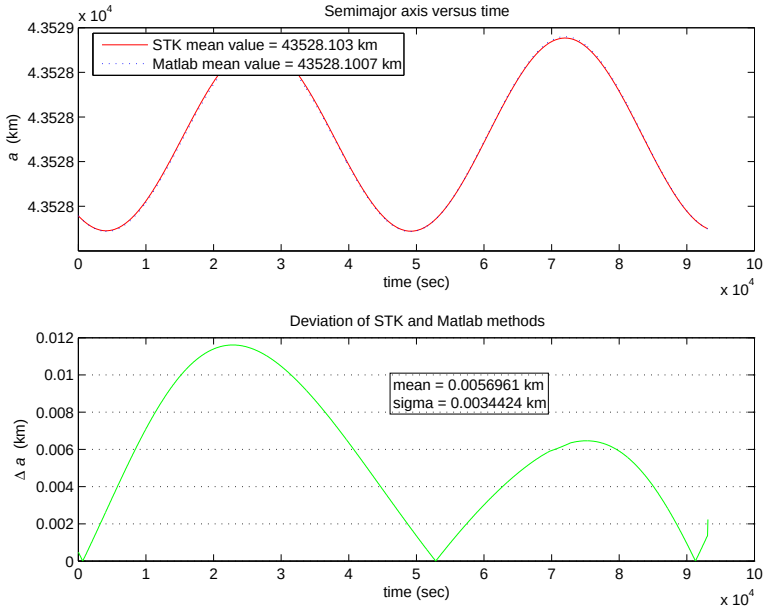

Figure 4.3: STK Similar Case Validation Results for Baseline Case Behavior of a for 1 Orbit.

Figure 4.5 depicts the behavior of ω, Ω and ν for one orbit. The STK results are plotted with the MATLAB® results for purposes of comparison. Again, the different methods yield very similar results for the osculating elements. The periodic motion of ω is expected; all perturbations from zonal harmonics, drag, third-bodies, and SRP induce periodic motion. Any secular motion, although small, should be expected as well; even zonal harmonics, third-body perturbations and SRP perturbations affect the motion of the satellite secularly [32]. Ω and ν, while uninteresting for such a short period, do reflect the predictable behavior of these COE for the satellite, and thus indicate an accurate algorithm. The precession of ν over the course of the orbit is evident in the figure. The right ascension, Ω, exhibits a downward secular trend, indicating that the ascending node (the point on the equatorial plane where the satellite crosses South to North) is precessing toward the Vernal Equinox (in a westerly direction).

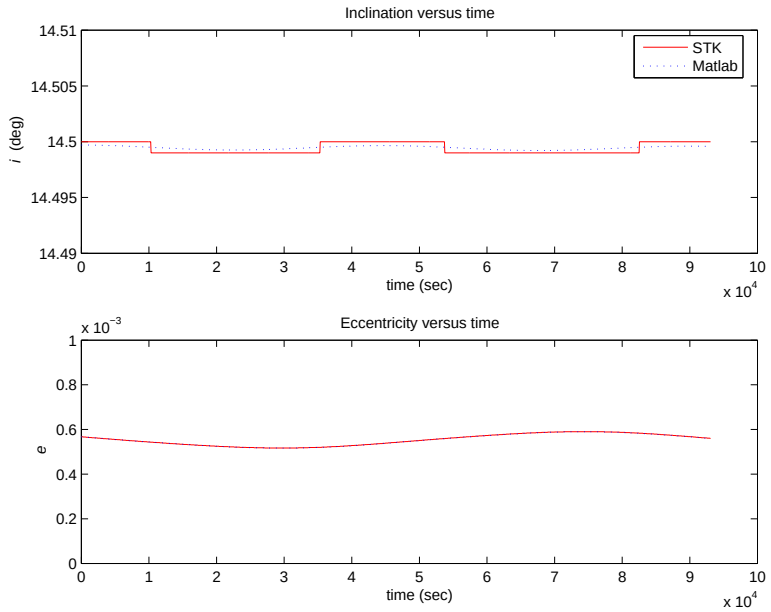

Figure 4.4: STK Similar Case Validation Results for Baseline Case Behavior of i and e for 1 Orbit.

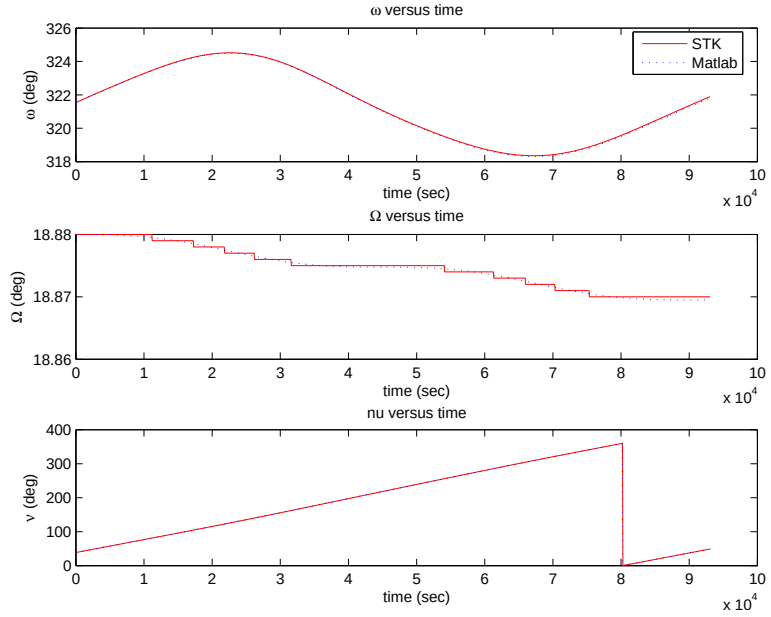

Figure 4.5: STK Similar Case Validation Results for Baseline Case Behavior of ω, Ω and ν for 1 Orbit.

Figures 4.6 and 4.7 illustrate the results for 100 orbits from STK and MATLAB®. Again, note that the STK results are very close to the MATLAB® results. The increase in deviation over time is most likely indicative of small time step differences in the respective integrators of STK and MATLAB® (HPOP and ode45), not of a growing difference between the semimajor axis vectors over the course of many orbits. Since, especially for the 100 orbit case, the deviation appears to have nearly equal discrete steps, another explanation for the rising difference stems from MATLAB®MATLAB® using double precision and STK using a single precision-type integrator. If looked at closely, the trace of a for both methods lies nearly colinearly over the entire time set.

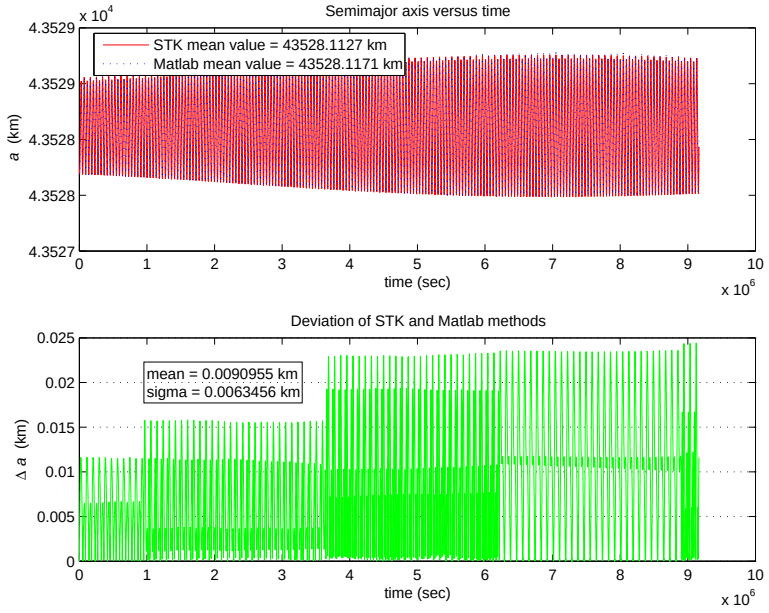

Figure 4.6: STK Similar Case Validation Results for Baseline Case Behavior of a for 100 Orbits.

Figures 4.8 and 4.9 illustrate the results for 1000 orbits from STK and MATLAB®. As in the previous plots of 1 and 100 orbits, the semimajor axis exhibits nearly zero change, as would be expected under no controller influence. The MATLAB® results are again similar, in both period and magnitude, to the STK results. Notice that the mean deviation has decreased from the 100 orbit case, and the 1 sigma standard deviation value has as well.

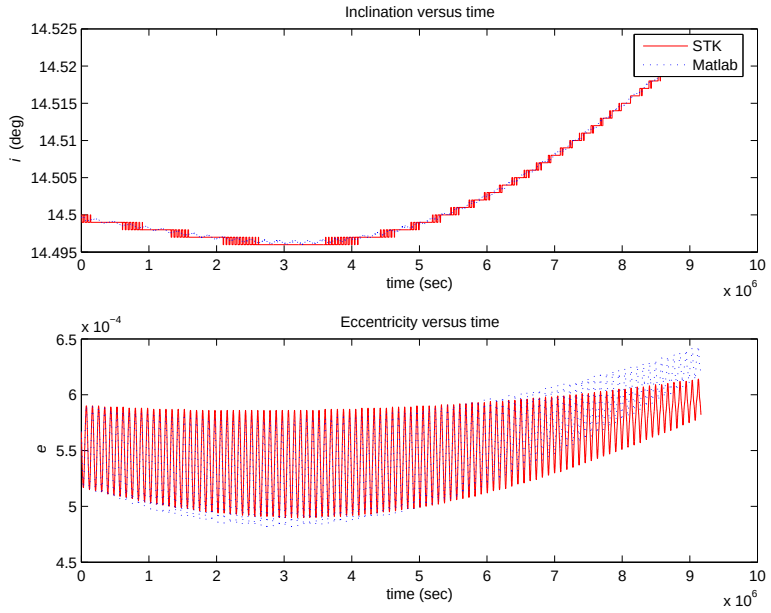

Figure 4.7: STK Similar Case Validation Results for Baseline Case Behavior of i and e for 100 Orbits.

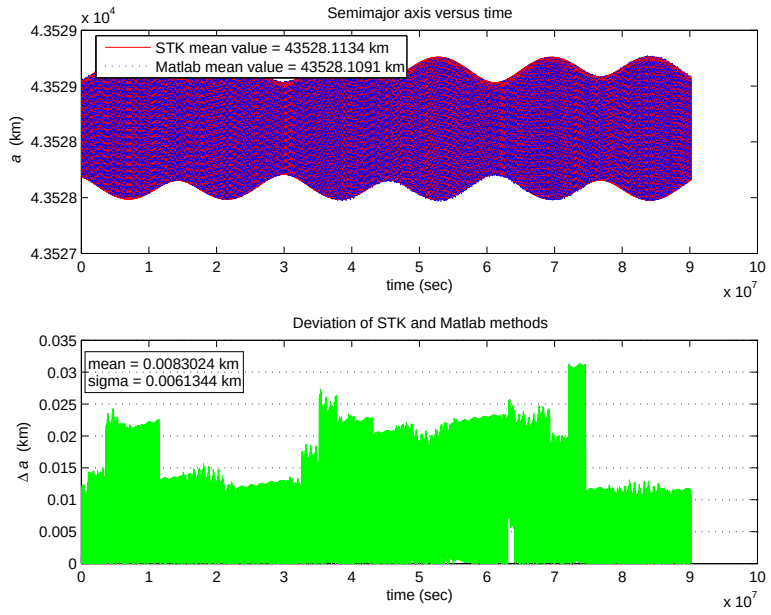

Figure 4.8: STK Similar Case Validation Results for Baseline Case Behavior of a for 1000 Orbits.

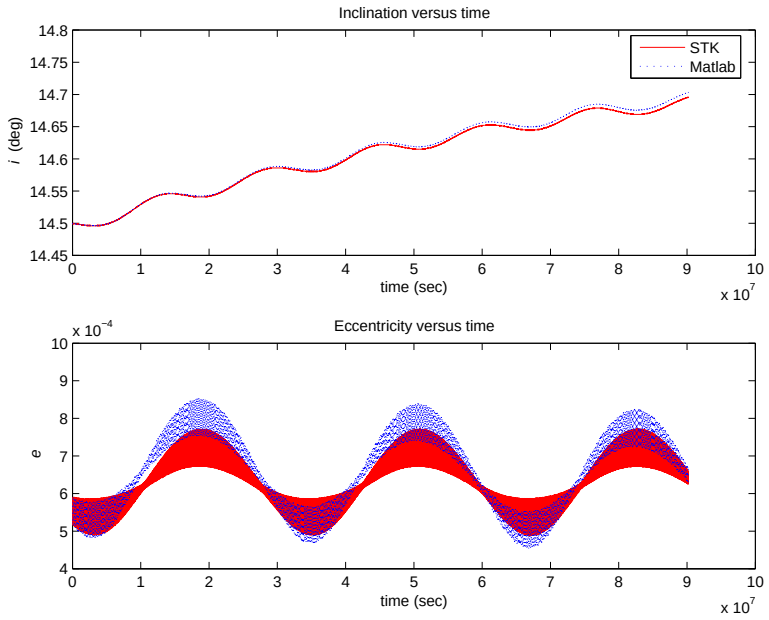

Figure 4.9: STK Similar Case Validation Results for Baseline Case Behavior of i and e for 1000 Orbits.

In conclusion, note that the results generated exhibited only periodic changes in semimajor axis, inclination and eccentricity, as expected. The periodic and secular variations were present in the plots of ω, Ω and ν, again as expected. Just as notable, the STK results seems to validate the MATLAB® code; the small differences between the methods are most likely due to only the numerical integration differences between HPOP and ode45. Most importantly, both methods induced no secular changes in semimajor axis over any number of orbits.

4.2 Nominal Coefficient Case

This section addresses the cases in which the satellite's coefficients of absorption, specular reflection and diffuse reflection are each set to equal one-third (hereafter referred to as the nominal coefficient case). The nominal case was initially chosen to represent the current properties of the DSCS II satellite since they are not well known. Recall that the surfaces of the satellite have degraded significantly since launch into orbit, and the current coefficients of absorption and reflection cannot be directly measured. Without good data on the coefficients, equal weighting

is a reasonable starting point for analysis. Later in the chapter, other possible values of the reflection and absorption coefficients will be investigated and used in the orbital propagation of the satellite, including the cases where each coefficient is made to be dominant. In particular, four additional cases will be examined to observe the changing effects on the satellite's perturbed orbit: all absorption ($c_{Ra} = 1$), all specular reflection ($c_{Rs} = 1$), all diffuse reflection ($c_{Rd} = 1$) and a mix of diffuse and specular reflection ($c_{Rs} = 0.5$ and $c_{Rd} = 0.5$).

For this case, and the cases to follow, one would expect secular changes in semimajor axis due to the use of the controllers. Since the area-to-mass ratio factors linearly into Equation **??** for the perturbing acceleration due to SRP, one would also expect that the higher the ratio, the greater the secular change in semimajor axis (with a linear relationship). In general, one would expect the complex controller to yield greater secular changes in semimajor axis, but this could prove to be dependent on the designated coefficients of absorption and reflection since the controller was designed for purely specular reflection.

4.2.1 Simple Controller Case. This section covers the test case results for the simple controller described in Section 3.4.1. Again, the nominal coefficients of reflection and absorption were used. Two subcases were considered: one using the original approximated despun platform area and the second using varying areas to illustrate the effects of larger exposed areas to the Sun. Note that each of the remaining plots for 1000 orbits has been orbit averaged, that is, the data sets have been reduced via the MATLAB® polyfit command to a linear best fit curve so as to give a clearer representation of the results.

4.2.1.1 Original Despun Platform Area. The original approximated area of the satellite's despun platform (based on the cross-sectional areas of the parabolic antennae) is 3.3445 m^2. The results in this section include that area in the MATLAB® algorithm.

For ease of comparison, the behavior of the semimajor axis using the simple controller are overlaid on the corresponding baseline results from Section 4.1. The behaviors of i, e, ω, Ω and ν are for the most part uninteresting. In any case, as long as the results are as expected per the perturbations included in the algorithm, their values do not affect the desired solution (ultimately, the raise in semimajor axis). Except for the baseline cases in the previous section, therefore, the plots of i and e will be omitted in favor of plots solely of the semimajor axis over time.

Figure 4.10 is a comparison of the baseline and simple controller cases for one orbit only. Note that in each plot hereafter, the change in semimajor axis for the controller case (calculated with polyfit) is given in the title above the plot. The change in semimajor axis, Δa, for the baseline case is 0.35462 km; for the simple controller case, it is 0.30981 km. Normally, one would expect that using the simple controller would be more advantageous than using no controller. The rise over one orbital period, however, is difficult to calculate accurately because the change in semimajor axis is based on the line fit of the osculating element a, rather than a computation of the mean elements. Essentially, the short-periodic variations in a are adversely skewing the calculation of Δa for one orbit. The line fit method gives more representative results when used for the 100 and 1000 orbit results. The plots for 100 and 1000 orbits, as illustrated in Figures 4.11 and 4.12 respectively, yield better results than the baseline case. For 100 orbits, the secular change in semimajor axis is 3.186 km, while for 1000 orbits it is 31.6495 km.

4.2.1.2 Varied Despun Platform Area. The results presented in this section use two area factors to illustrate the changes in behavior of the semimajor axis. The first plot was generated with the area factor equal to five; the second was generated with the area factor set equal to ten.

The 1000 orbit results with an area factor of five (the original despun platform area multiplied by five) are shown in Figure 4.13. At this point, the results begin to vary significantly from the results using the nominal parabolic antennae effective area, especially for the larger number of orbits. Although the plot is not shown, for one orbit, the change in semimajor axis using the

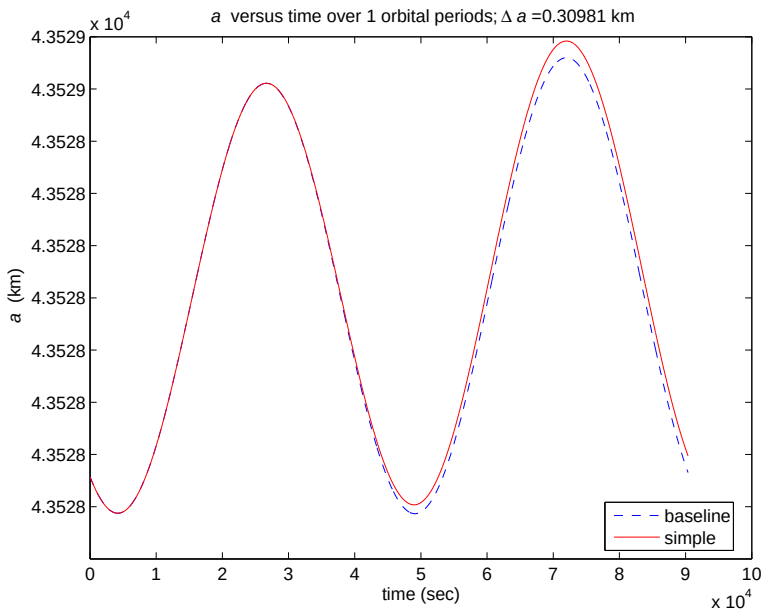

Figure 4.10: Simple Controller Case Behavior of a for Nominal Reflection Coefficients, 1 Orbit and an Area Factor of 1, Overlaid with the Corresponding Baseline Case Behavior of a.

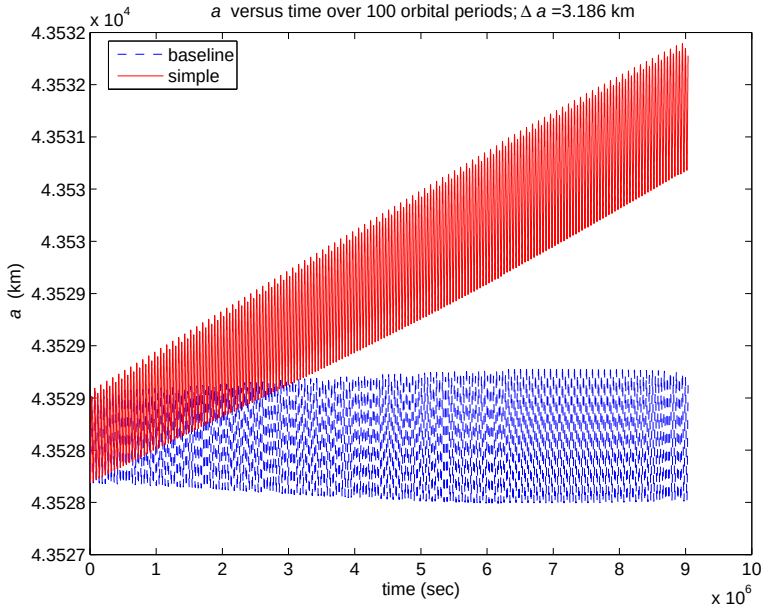

Figure 4.11: Simple Controller Case Behavior of a for Nominal Reflection Coefficients, 100 Orbits and an Area Factor of 1, Overlaid with the Corresponding Baseline Case Behavior of a.

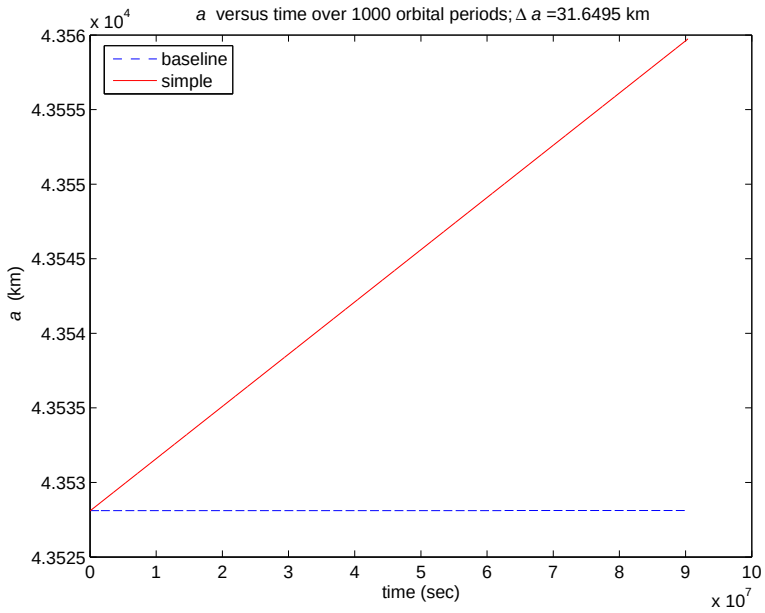

Figure 4.12: Simple Controller Case Behavior of a for Nominal Reflection Coefficients, 1000 Orbits and an Area Factor of 1, Overlaid with the Corresponding Baseline Case Behavior of a.

simple controller is 0.49196 km. For 100 orbits, the gain from using the simple controller over no controller is 15.8675 km and for 1000 orbits it is 158.7075 km. This is a marked improvement over the results in Section 4.2.1.1.

The 1000 orbit results with an area factor of ten (the original despun platform area multiplied by ten) are shown in Figure 4.14. Once again, the results vary significantly from the nominal parabolic antennae effective area, especially for the larger number of orbits. For one orbit, the gain from using the simple controller over no controller is 0.3650 km. For 100 orbits, the change in semimajor axis is 31.7532 km and for 1000 orbits it is 318.2681 km. Based on these results, it appears that the rate of change of semimajor axis is directly proportional to the variable area, as would be expected from the equation for the force due to SRP (Equation 3.67).

4.2.2 Complex Controller Case. This section covers the test case results for the complex controller described in Section 3.4.2. Again, the nominal coefficients of reflection and absorption

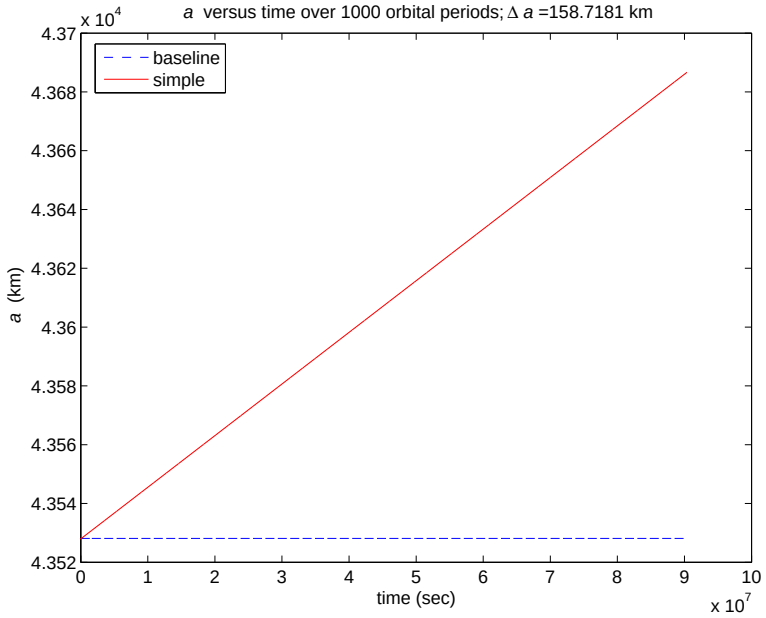

Figure 4.13: Simple Controller Case Behavior of a for Nominal Reflection Coefficients, 1000 Orbits and an Area Factor of 5, Overlaid with the Corresponding Baseline Case Behavior of a.

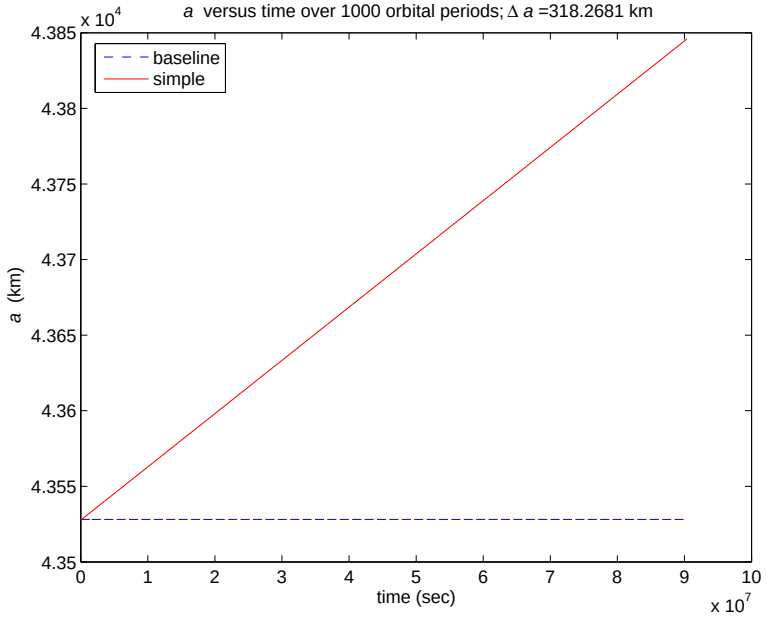

Figure 4.14: Simple Controller Case Behavior of a for Nominal Reflection Coefficients, 1000 Orbits and an Area Factor of 10, Overlaid with the Corresponding Baseline Case Behavior of a.

were used. Two subcases were considered: one using the original approximated despun platform area and the second using varying areas to illustrate the effects of larger parabolic antennae.

4.2.2.1 Original Despun Platform Area. Using the satellite's original apparent despun platform area, the semimajor axis values for the complex controller and baseline cases for 1000 orbits were plotted against the elapsed time in Figure 4.15. For one orbit, the raise in semimajor axis is 0.31468 km. For 100 orbits, the difference from using the complex controller over having no controller is 3.4137 km, and for 1000 orbits it is 34.2982 km. The complex controller, for the nominal coefficient case, yields approximately an 8% increase over the simple controller.

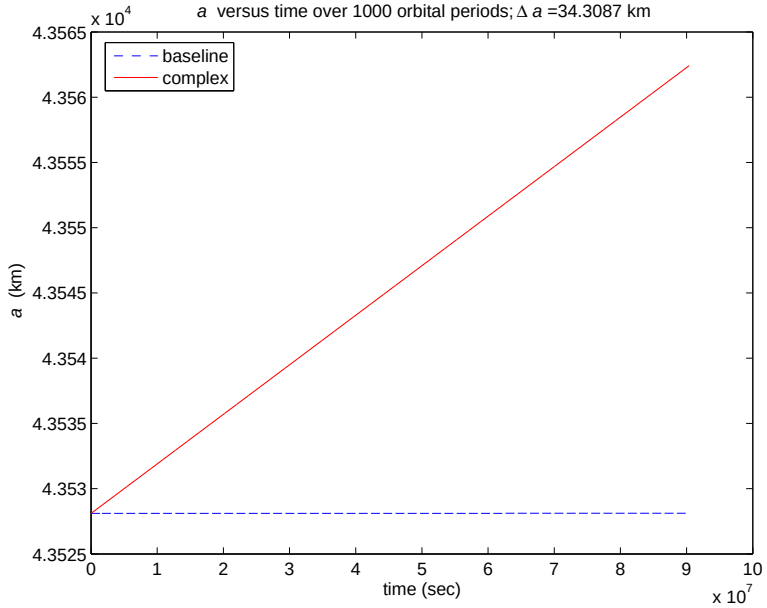

Figure 4.15: Complex Controller Case Behavior of a for Nominal Reflection Coefficients, 1000 Orbits and an Area Factor of 1, Overlaid with the Corresponding Baseline Case Behavior of a.

4.2.2.2 Varied Despun Platform Area. The results presented in this section use two area factors (five and ten) to illustrate the changes in behavior of the semimajor axis. The plot shown was generated with the area factor set equal to ten.

Similarly to the results for the simple controller, a larger effective area for the despun platform results in a significant benefit in semimajor axis increase. For an area factor of five, over one orbit

the semimajor axis rose 0.51633 km, resulting in a benefit over having no controller of 0.16171 km). Over 100 orbits, the benefit is 17.0713 km, and over 1000 orbits it is 172.1135 km.

Figure 4.16 shows the 1000 orbit results when the despun platform effective area is multiplied by ten. Over one orbit, the benefit over having no controller is 0.41377 km. For 100 orbits, it is 34.1493 km, and for 1000 orbits it is 345.1880 km.

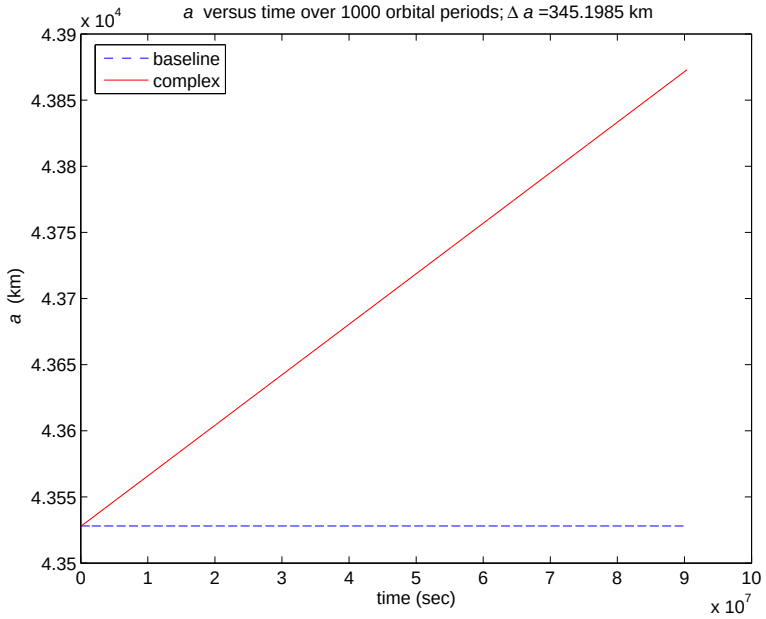

Figure 4.16: Complex Controller Case Behavior of a for Nominal Reflection Coefficients, 1000 Orbits and an Area Factor of 10, Overlaid with the Corresponding Baseline Case Behavior of a.

As expected, the semimajor axis results yielded by using the controllers were dominated by the secular changes, although the periodic changes are evident in the plots for 1 and 100 orbits. For at least the nominal case, and it is predicted for the remaining cases, the area factors do appear to yield a linear relationship with the changes in semimajor axis.

4.3 Absorption Case

This section details the results from the cases in which the diffuse and specular coefficients of reflection have been set to equal zero and the coefficient of absorption has been set to one (hereafter referred to as the "all-absorption" case). It is expected that the performance of the

satellite (with regards to raising the semimajor axis) under the SRP perturbation will be the least in the all-absorption case, primarily due to the direction of the resultant force vector under the all-absorption condition.

4.3.1 Simple Controller Case. This section addresses the results for the all-absorption case using the simple controller described in Section 3.4.1. Two subcases were considered: one using the original approximated despun platform area and the second using varying areas (of five and ten times the original area) to illustrate the effects of a larger despun platform area on the semimajor axis.

4.3.1.1 Original Despun Platform Area. The results in this section use an apparent despun platform area of 3.3445 m^2. Similarly to Section 4.2.1.1, the semimajor axis results from the simple controller test cases are overlaid on the baseline cases for purposes of comparison.

In Figure 4.17, note that the two cases nearly overlap. For one orbit, the raise in semimajor axis for the original area case is 0.29399 km, while for the baseline case it is 0.35462 km. The all absorption result is, as expected, slightly less than the nominal case result in Section 4.2.1.

The data for 100 and 1000 (see Figure 4.18) orbits yield similarly scaled results. For 100 orbits, the change in semimajor axis is 2.1010 km, and for 1000 orbits it is 20.7914 km. These results are, again, slightly lower the nominal case.

4.3.1.2 Varied Despun Platform Area. The results in this section use two different area multiplication factors to illustrate the changes in semimajor axis when using larger despun platform areas. The first plot, Figure 4.19, uses an area factor of five applied to the despun platform's original effective area. The second, Figure 4.20, uses an area factor of ten.

The simple controller does not glean much benefit over the no controller case for one orbit. The advantage is only 0.05823 km, compared to 0.1373 km for the nominal case. The difference for 100 orbits is 10.4413 km and for 1000 orbits (Figure 4.19) it is 104.3604 km. Using the nominal

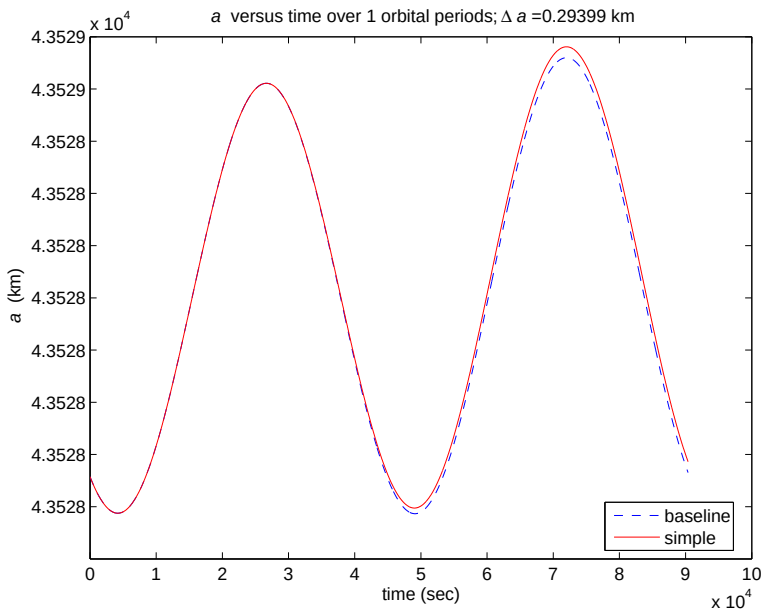

Figure 4.17: Simple Controller Case Behavior of a for all Absorption, 1 Orbit and an Area Factor of 1, Overlaid with the Corresponding Baseline Case Behavior of a.

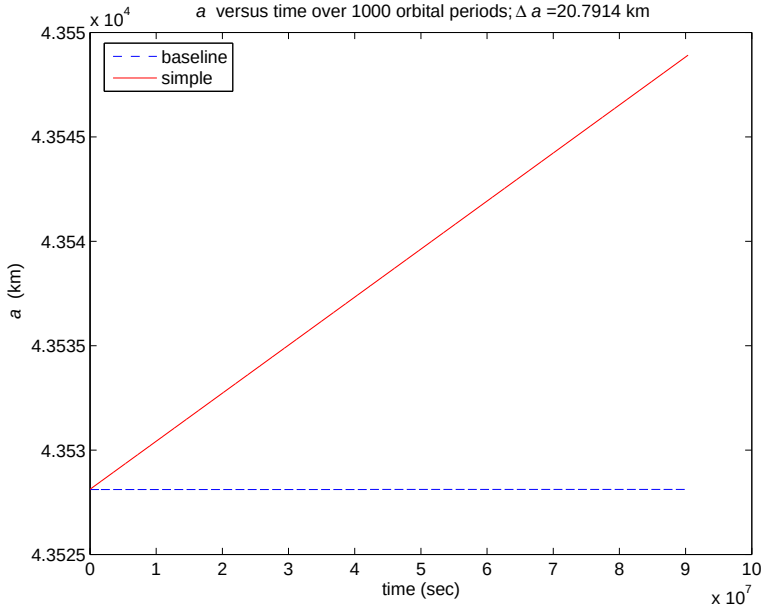

Figure 4.18: Simple Controller Case Behavior of a for all Absorption, 1000 Orbits and an Area Factor of 1, Overlaid with the Corresponding Baseline Case Behavior of a.

coefficients of absorption and reflection, Δa for 1000 orbits was 158.7181 km; for the all absorption case, it is 104.3709 km. As expected, the all absorption case yields a lower semimajor axis increase than the nominal case.

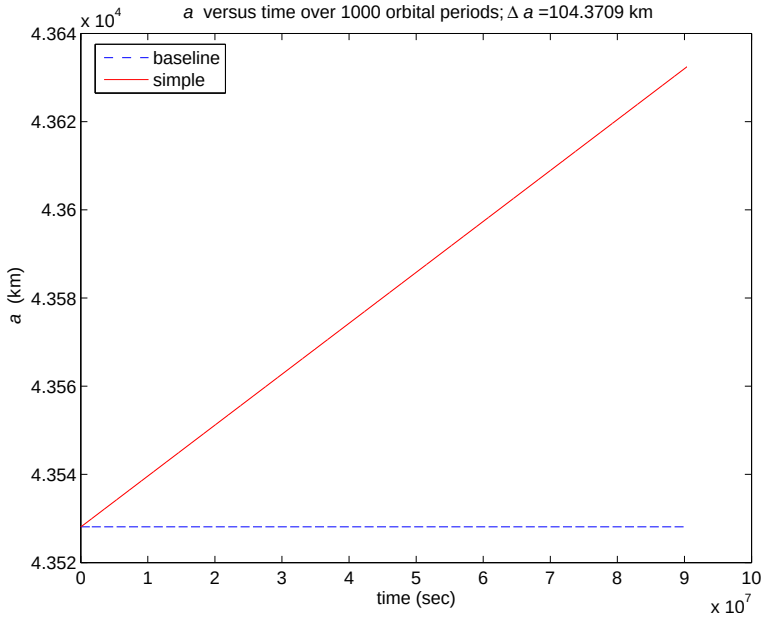

Figure 4.19: Simple Controller Case Behavior of a for all Absorption, 1000 Orbits and an Area Factor of 5, Overlaid with the Corresponding Baseline Case Behavior of a.

The resulting Δa for an area multiplication factor of ten are, of course, higher than the previous results for the all absorption test case. The change in semimajor axis for one orbit is 0.56143 km, for 100 orbits is 20.9048 km and for 1000 orbits (Figure 4.20) is 209.1176 km. Over 1000 orbits, therefore, the semimajor axis increase is about 100 km less than in the corresponding nominal case, where it was 318.2681 km.

4.3.2 Complex Controller Case. Perhaps counterintuitively, the implementation of the complex controller yields less semimajor axis change than the simple controller for the all absorption case, as illustrated in Figure 4.22. The complex controller reorients the despun platform more often than the simple controller, thus the apparent area of the despun platform will be greater for a longer period of time during the orbit. This causes the resultant force vector from SRP to dominate the

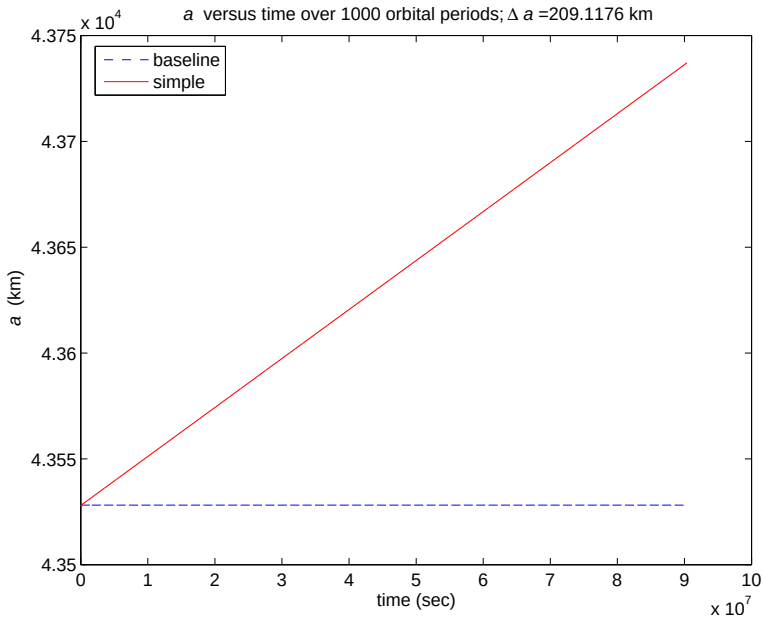

Figure 4.20: Simple Controller Case Behavior of a for all Absorption, 1000 Orbits and an Area Factor of 10, Overlaid with the Corresponding Baseline Case Behavior of a.

complex controller case and the effects of all absorption, therefore, degrade the performance of the satellite under SRP perturbations more quickly. In short, the complex controller is optimized for purely specular reflection, not for pure absorption. The percent difference in using the complex controller versus the simple controller is approximately -39%.

4.3.2.1 Original Despun Platform Area. This section addresses the results of using the complex controller for the all absorption case with the original despun platform approximated area. The resulting changes in the semimajor axis, although an improvement on the baseline case, indicates that this is the least effective scenario for raising the semimajor axis of the satellite orbit (among the cases studied for the purposes of this thesis).

Over one orbit, Δa is 0.28844 km, which is 0.06618 km less than the baseline case. For 100 orbits, Δa is 1.28454 km. For 1000 orbits, as illustrated in Figure 4.21, Δa is 12.6063 km. This is approximately sixty percent of the semimajor axis raise from using the simple controller (see Section 4.3.1.1) and about a third of the complex controller nominal case value in Section 4.2.2.1.

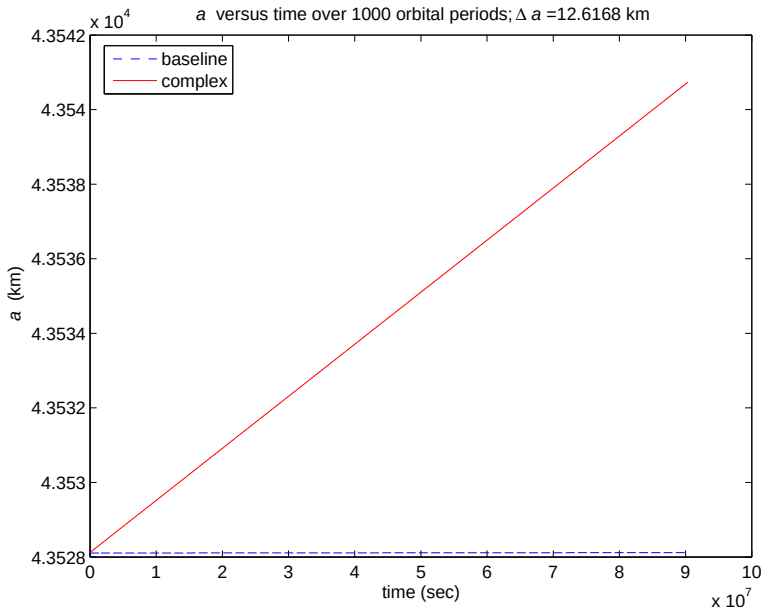

Figure 4.21: Complex Controller Case Behavior of a for all Absorption, 1000 Orbits and an Area Factor of 1, Overlaid with the Corresponding Baseline Case Behavior of a.

4.3.2.2 Varied Despun Platform Area. The results presented in this section use the two aforementioned area factors of five and ten. Figure 4.22 illustrates the 1000 orbit results using an area factor of ten applied to the despun platform.

Like the original area results in Section 4.3.2.1, the changes in semimajor axis in this section continue to be less than all other cases except the baseline case. In particular, for an area factor of five over one orbit, Δa is 0.38511 km. For 100 orbits, Δa is 6.4357 km, and for 1000 orbits it is 63.2965 km. For 1000 orbits, the raise in semimajor axis is about 40 km less than that for the simple controller under all absorption.

Figure 4.22 illustrates the effects of having ten times the original estimated despun platform area for 1000 oribts. For one orbit, the resulting Δa of 0.50595 km is only marginally better than for an area factor of five. Δa is 12.8627 km for 100 orbits, and 126.7702 km for 1000 orbits, which is significantly less than for the complementary nominal case.

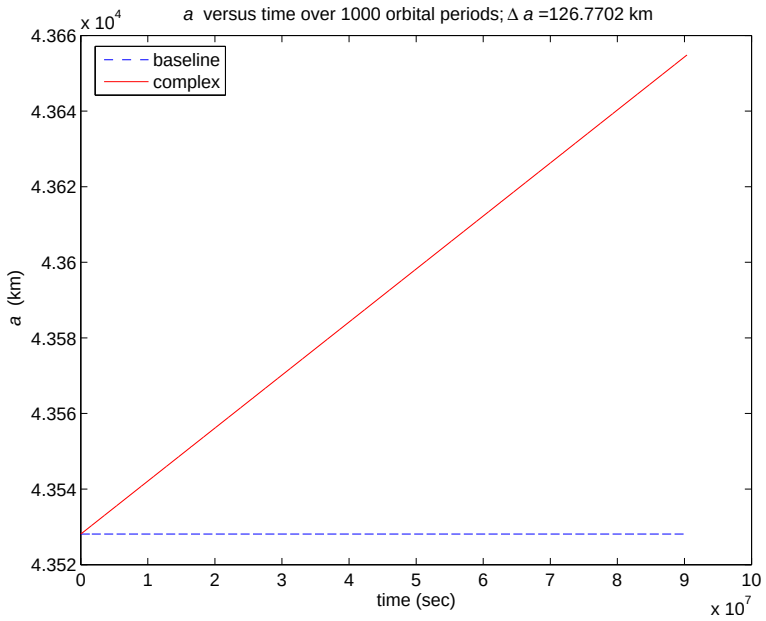

Figure 4.22: Complex Controller Case Behavior of a for all Absorption, 1000 Orbits and an Area Factor of 10, Overlaid with the Corresponding Baseline Case Behavior of a.

4.4 Specular Reflection Case

The specular reflection section addresses the test cases in which the coefficient of specular reflection of the satellite's despun platform is set to one and the remaining coefficients are set to zero. As in the previous sections, several subcases were considered. Test cases were run in MATLAB® for both the simple controller and the complex controller; for each controller the original despun platform approximated area and the area factors of five and ten times the original area were used.

4.4.1 Simple Controller Case. This section presents the results for the purely specular reflection case using the simple controller described in Section 3.4.1. Two subcases were considered: one using the original approximated despun platform area, and the second using varying areas (of five and ten times the original area) to illustrate the effects of having a larger despun platform area on the semimajor axis of the satellite's orbit.

4.4.1.1 Original Despun Platform Area. To facilitate comparison between the purely specular reflection results and the baseline results, the respective results for the behavior of the semimajor axis over time are overlaid in Figures 4.23-4.24.

For one orbit, as shown in Figure 4.23, the simple controller yields a raise in semimajor axis of 0.32216 km. The specular reflection case, therefore, exhibits the most change in semimajor axis thus far, and one would expect the remaining results in Section 4.4.1 to corroborate this. Over 100 orbits Δa is 4.0176 km, and over 1000 orbits Δa is 40.0064 km. These values do in fact exceed the raises in semimajor axis presented in the previous sections (for the simple controller and nominal area).

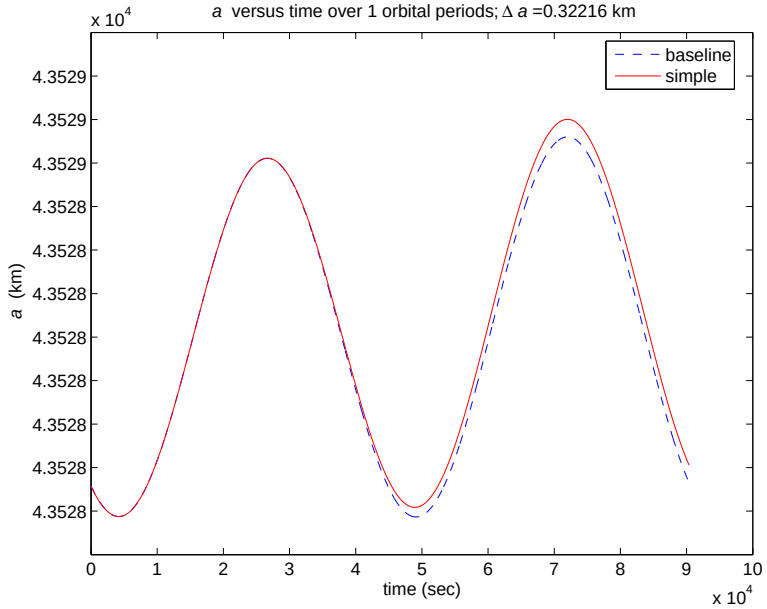

Figure 4.23: Simple Controller Case Behavior of a for all Specular Reflection, 1 Orbit and an Area Factor of 1, Overlaid with the Corresponding Baseline Case Behavior of a.

4.4.1.2 Varied Despun Platform Area. In Section 4.4.1.1, the results presented were the highest raise in semimajor axis thus far, so one would expect the trend to continue for larger despun platform areas. This section addresses the results when area factors of five and ten were applied to the despun platform area.

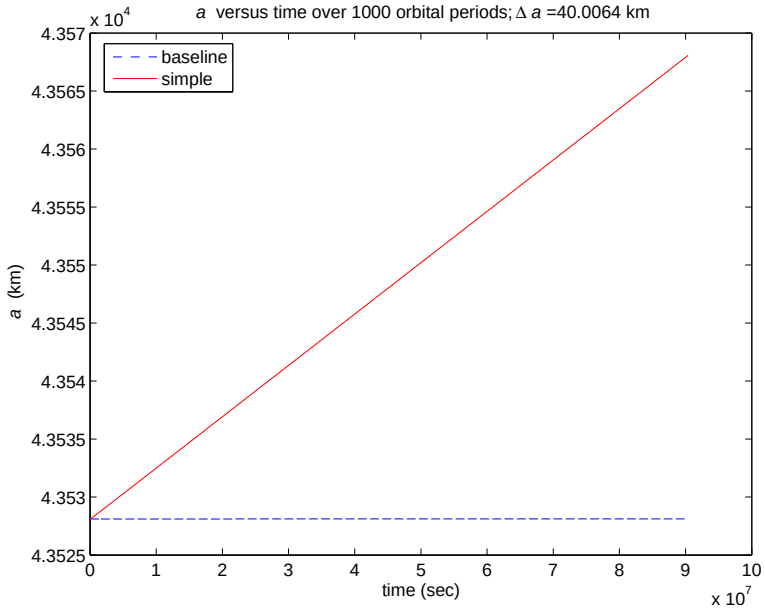

Figure 4.24: Simple Controller Case Behavior of a for all Specular Reflection, 1000 Orbits and an Area Factor of 1, Overlaid with the Corresponding Baseline Case Behavior of a.

For an area factor of five, the results in Figure 4.25 exhibit a marked improvement over the original area results in Section 4.4.1.1, and have nearly double the semimajor axis rise of the corresponding all absorption case. For one orbit, Δa is 0.5537 km. For 100 orbits, the raise is 20.0511 km (the all absorption case was 10.4542 km, by comparison); for 1000 orbits, it is 200.5718 km (the all absorption case was 104.3709 km).

Figure 4.26 (1000 orbits) was generated with the area factor set equal to ten. As expected, the raise in semimajor axis is greater in this case than for both the nominal area and with an area factor of five for the same scenario. The raise in semimajor axis over one orbit is 0.84314 km, which is approximately 0.3 km more than for an area factor of five and 0.5 km more than for the nominal area. This result is also the best for any one-orbit case so far, although one would expect the complex case to generate a larger change in a since the controller was designed for purely specular reflection.

Over 100 orbits, the simple controller generated a Δa of 40.0860 km, double that of the area factor of five and ten times that of the nominal area for this case. For 1000 orbits, the Δa is

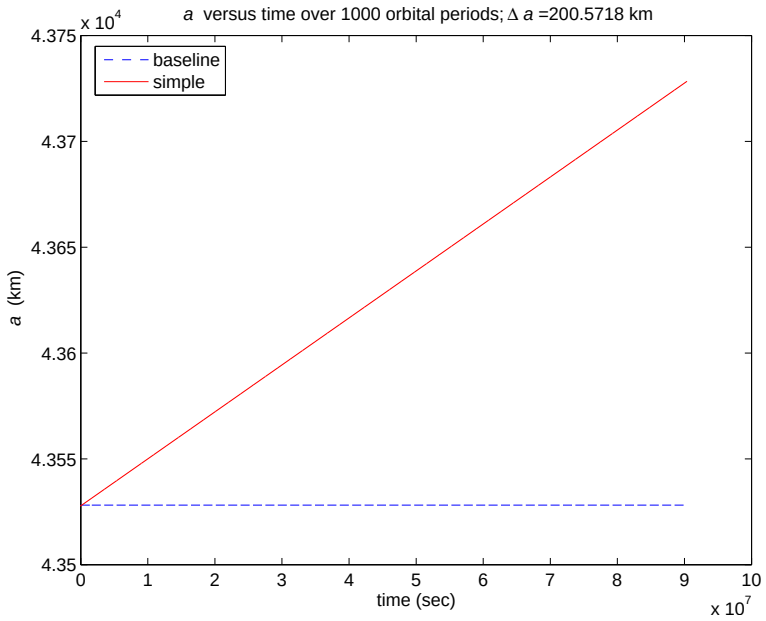

Figure 4.25: Simple Controller Case Behavior of a for all Specular Reflection, 1000 Orbits and an Area Factor of 5, Overlaid with the Corresponding Baseline Case Behavior of a.

402.4059 km, which again is roughly twice that of the area factor of five and ten times that of the nominal area for this case. Also, as for the one-orbit case above, the values of Δa for each set of orbits are the highest yet.

4.4.2 Complex Controller Case. This section covers the test case results for the complex controller. Again, the scenarios used all specular reflection. Two subcases were considered: one with the nominal despun platform area and the second with area factors of five and ten applied to the nominal area. The percent improvement over the simple controller is approximately 42%.

4.4.2.1 Original Despun Platform Area. The satellite's original effective despun platform area was used to compute the change in semimajor axis over time, as illustrated in Figure 4.27 for 1000 orbits. Δa for one orbit is 0.34002 km, which is a slight improvement over the simple controller case in Section 4.4.1.1. Over 100 orbits, the raise in semimajor axis is 5.6209 km, and for 1000 orbits it is 56.8227 km. As expected, these yield the best results so far for the respective number of orbits.

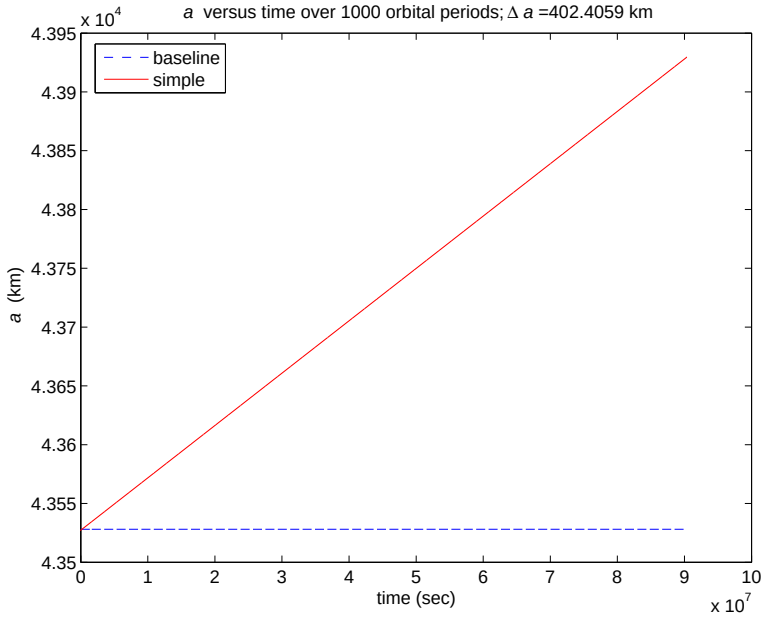

Figure 4.26: Simple Controller Case Behavior of a for all Specular Reflection, 1000 Orbits and an Area Factor of 10, Overlaid with the Corresponding Baseline Case Behavior of a.

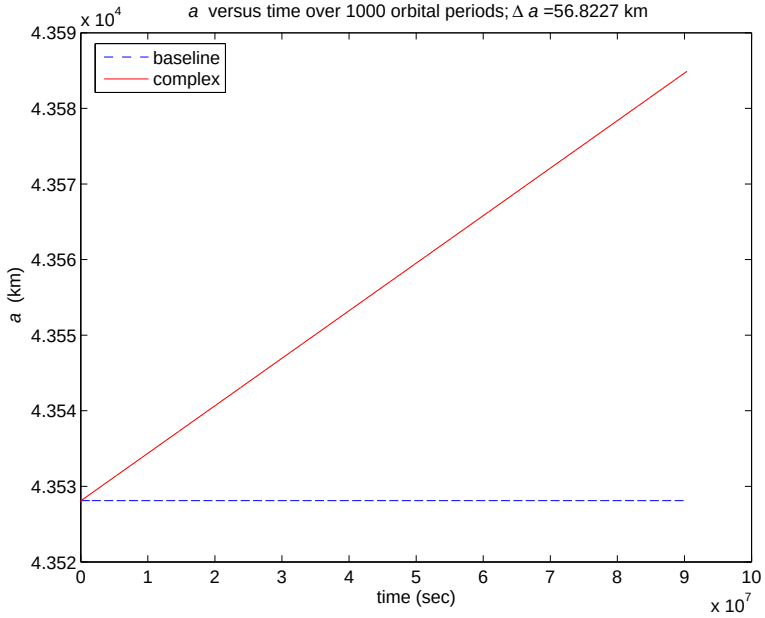

Figure 4.27: Complex Controller Case Behavior of a for all Specular Reflection, 1000 Orbits and an Area Factor of 1, Overlaid with the Corresponding Baseline Case Behavior of a.

4.4.2.2 Varied Despun Platform Area. This section addresses the changes in semimajor axis over time using area factors of five and ten applied to the nominal despun platform area. For an area factor of five, the semimajor axis exhibits a raise of 0.6430 km for one orbit, which is 0.09 km greater than for the simple controller. Δa for 100 orbits is 28.0751 km (about 8 km more than for the simple controller) and for 1000 orbits it is 285.0813 km (roughly 85 km more than for the simple controller).

Figure 4.28 reveals the results generated when an area factor of ten is applied to the original despun platform area. For one orbit, the change in semimajor axis is 1.0217 km, which is about 0.18 km more than the simple controller case and 0.68 km more than the baseline case. Δa for 100 orbits is 56.1473 km, which is roughly twice that of the complex controller for an area factor of five and 1.5 times the simple controller of the same case. For 1000 orbits, Δa is 573.5517 km. As expected, the results for 1000 orbits in this section represent the greatest change in semimajor axis thus far (and will prove, looking ahead, to be the largest Δa of all the cases).

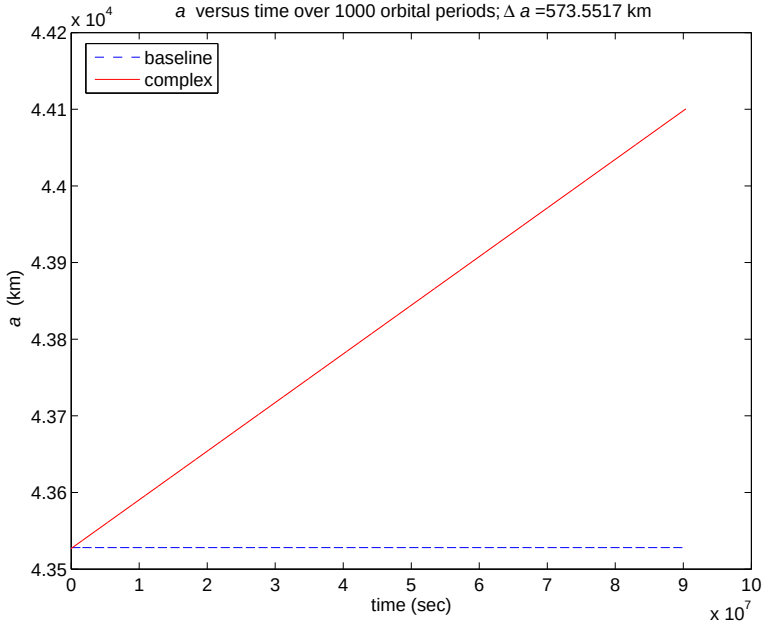

Figure 4.28: Complex Controller Case Behavior of a for all Specular Reflection, 1000 Orbits and an Area Factor of 10, Overlaid with the Corresponding Baseline Case Behavior of a.

4.5 Diffuse Reflection Case

The cases in this section implement the scenarios for all diffuse reflection; the diffuse reflection coefficient is set equal to one and the remaining coefficients are set equal to zero. As in the previous sections, the performance of the satellite will be assessed under two controllers and three distinct area options.

4.5.1 Simple Controller Case. The results for the simple controller, described in Section 3.4.1, appear in this section. For purposes of comparison, the results are again overlaid on the baseline case.

4.5.1.1 Original Despun Platform Area. The first test case for the simple controller employs the original despun platform area. For one orbit (Figure 4.29), the raise in semimajor axis is 0.31328 km, which is more than for the nominal and all absorption cases but less than for the all specular reflection case (the remaining results for Δa in Section 4.5 will follow this pattern of being slightly less than the specular case). Δa for 100 orbits is 3.4368 km and for 1000 orbits (Figure 4.30) it is 34.1497 km.

4.5.1.2 Varied Despun Platform Area. To illustrate the change in behavior of the semimajor axis over time for different despun platform areas, this section applies area factors of five and ten, respectively, to the nominal area. The first plot, Figure 4.31, depicts the semimajor axis changes over 1000 orbits for an area factor of five.

For one orbit, the raise in semimajor axis is 0.50933 km, for 100 orbits it is 17.1353 km and for 1000 orbits it is 171.3268 km. As expected, these values lie (respectively per number of orbits) between the nominal case and the specular reflection case for an area factor of five.

An area factor of ten yields better results; the raise in semimajor axis for one orbit is 0.75438 km, for 100 orbits it is 34.2684 km and for 1000 orbits it is 343.6828 km (as illustrated in Figure 4.32). For 1000 orbits, the diffuse reflection case yields a slight improvement over the

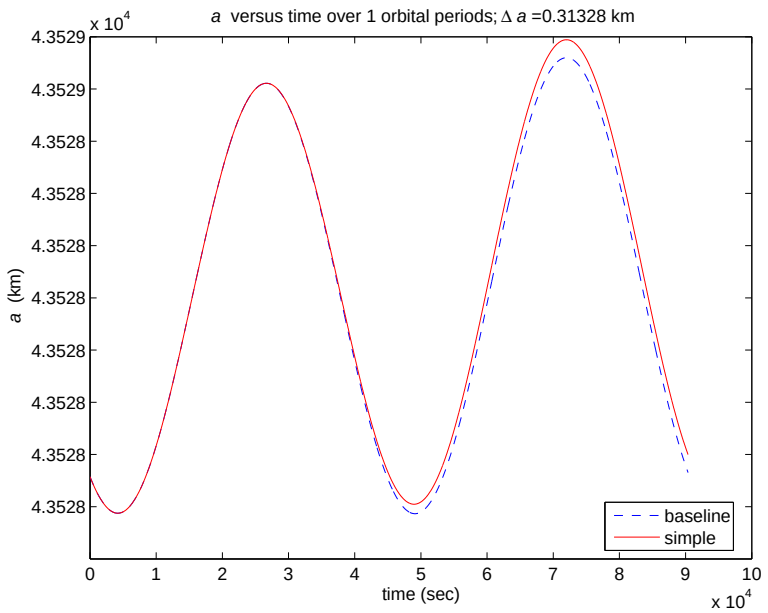

Figure 4.29: Simple Controller Case Behavior of a for all Diffuse Reflection, 1 Orbit and an Area Factor of 1, Overlaid with the Corresponding Baseline Case Behavior of a.

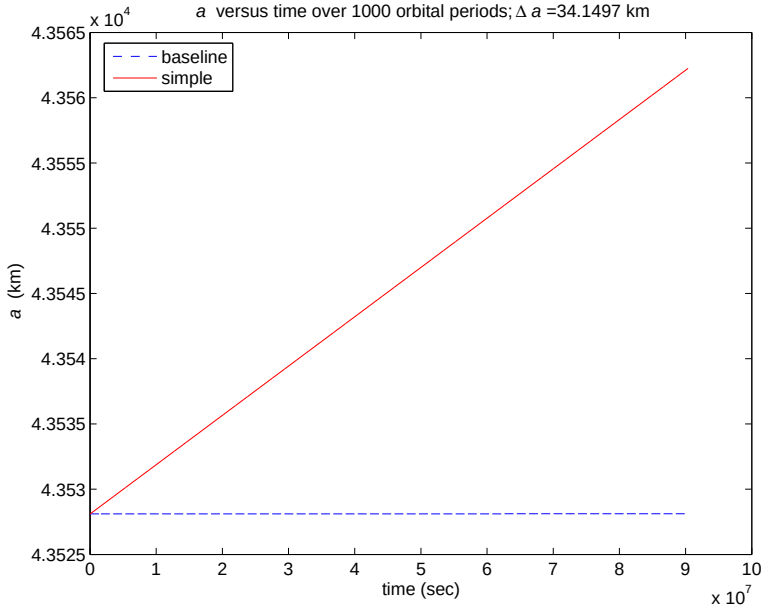

Figure 4.30: Simple Controller Case Behavior of a for all Diffuse Reflection, 1000 Orbits and an Area Factor of 1, Overlaid with the Corresponding Baseline Case Behavior of a.

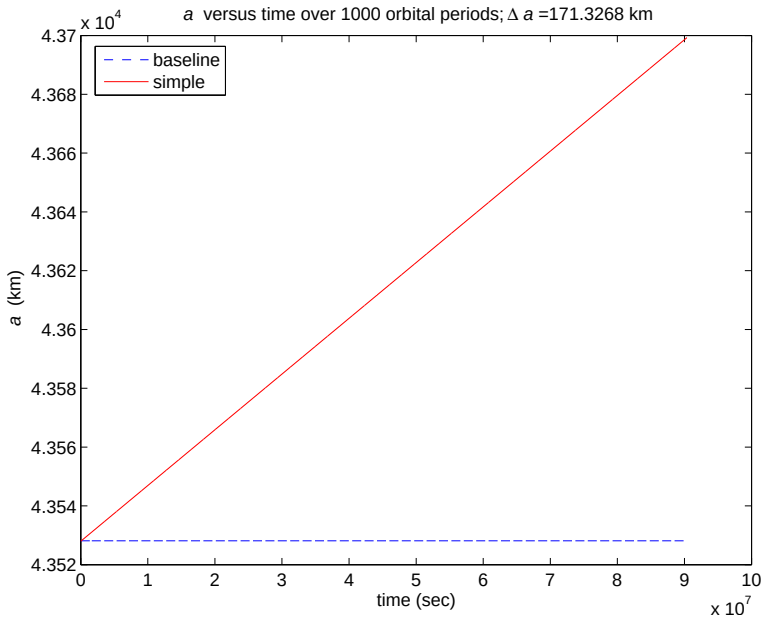

Figure 4.31: Simple Controller Case Behavior of a for all Diffuse Reflection, 1000 Orbits and an Area Factor of 5, Overlaid with the Corresponding Baseline Case Behavior of a.

nominal case (about 25 km), a marked improvement over the all absorption case (roughly 134 km) and a small disadvantage when compared to the specular reflection case (by about 59 km).

4.5.2 Complex Controller Case. This section addresses the changes in semimajor axis for the diffuse case when the complex controller is used versus the simple controller. Again, two subcases were considered: one with the original estimated despun platform area and the second with area factors of five and ten applied to the original area. The percent difference from using the complex controller over the simple controller is -1.7%.

4.5.2.1 Original Despun Platform Area. The nominal area results are illustrated for 1000 orbits in Figure 4.33. Similarly to the all absorption case, the resulting increases for the semimajor axis using the complex controller are slightly less than using the simple controller.

The raise in semimajor axis for one orbit is 0.31559 km, which is 0.0023 km more than for the simple controller. For 100 orbits Δa is 3.3594 km and for 1000 orbits Δa is 33.5575 km. For all diffuse reflection, the complex controller cases yield a slightly lower Δa than their corresponding

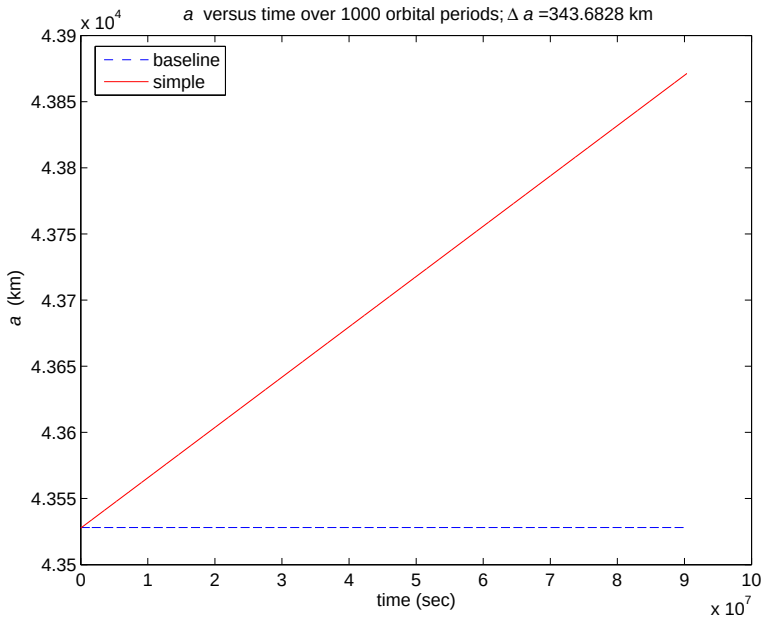

Figure 4.32: Simple Controller Case Behavior of a for all Diffuse Reflection, 1000 Orbits and an Area Factor of 10, Overlaid with the Corresponding Baseline Case Behavior of a.

simple controller cases for 100 and 1000 orbits (note, the differences between the controllers' results for the diffuse case are minimal as compared to the all absorption case).

4.5.2.2 Varied Despun Platform Area. The results presented in this section use two different area multiplication factors (five and ten) applied to the original despun platform area.

For an area factor of five, the resulting changes in semimajor axis are less than for the corresponding simple controller case. For one orbit, Δa is 0.52087 km; for 100 orbits, Δa is 16.7510 km; for 1000 orbits, Δa is 168.2071 km.

Figure 4.34 illustratea the change in semimajor axis versus time for an area factor of ten applied to the nominal despun platform area. While the results still vary dramatically from the baseline results, Δa is slightly less in this case than for the corresponding simple controller case. For one orbit, Δa is 0.77747 km. For 100 orbits, Δa is 33.4959 km and for 1000 orbits, Δa is 337.7322 km.

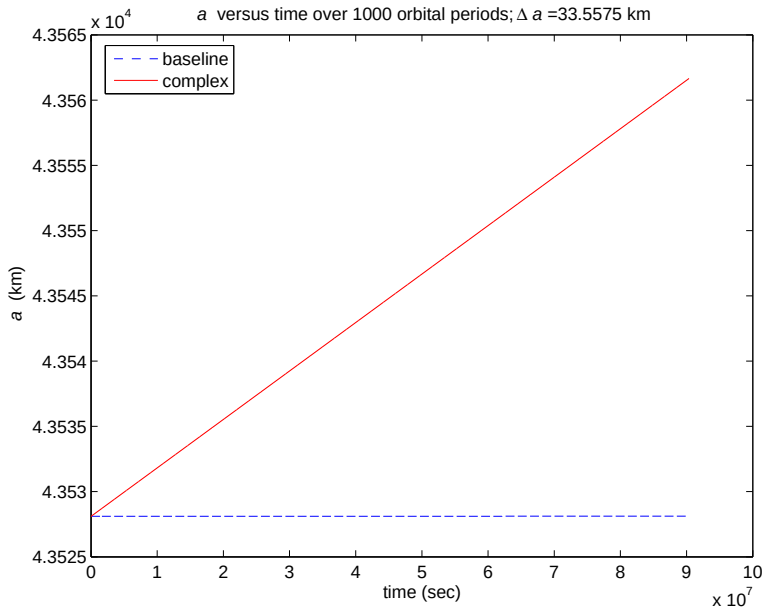

Figure 4.33: Complex Controller Case Behavior of a for all Diffuse Reflection, 1000 Orbits and an Area Factor of 1, Overlaid with the Corresponding Baseline Case Behavior of a.

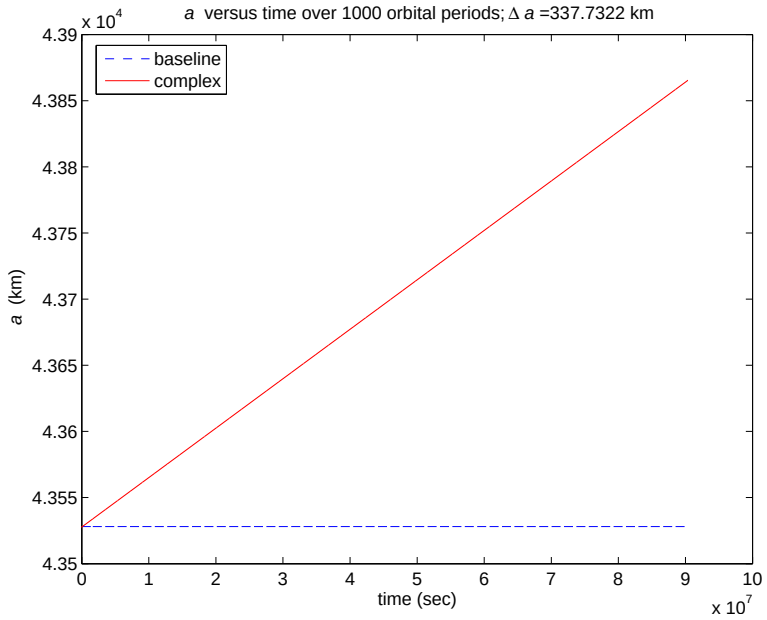

Figure 4.34: Complex Controller Case Behavior of a for all Diffuse Reflection, 1000 Orbits and an Area Factor of 10, Overlaid with the Corresponding Baseline Case Behavior of a.

4.6 Specular and Diffuse Reflection Case

This section addresses the case in which the satellite's diffuse and specular coefficients of reflection are each set to equal one-half and the coefficient of absorption is set to zero. One would expect the results for this case (hereafter referred to as the mixed reflection case) to fall between the results from the previous two sections (purely diffuse and purely specular reflections). The resultant force vector for the mixed case will lie between the resultant force vectors for the purely specular and purely diffuse cases, which leads to the change in semimajor axis being in between the two cases as well.

4.6.1 Simple Controller Case. The simple controller, described in Section 3.4.1, is implemented in this section. The mixed reflection case of half specular and half diffuse reflection was used to produce the plots in the following sections. Two subcases were considered: one using the original despun platform area, and the second using varying areas to illustrate the effects of larger despun platform areas on the semimajor axis.

4.6.1.1 Original Despun Platform Area. The results in this section use the original despun platform area. To facilitate straightforward comparison, the results from this section were plotted on the same graphs as the baseline results from Section 4.2.1. Figures 4.35-4.36 illustrate the original area results for the mixed reflection case.

For one orbit, the raise in semimajor axis is 0.31772 km, which does lie between the corresponding purely specular (0.32216 km) and purely diffuse (0.31328 km) values as expected. For 100 orbits, Δa is 3.7267 km; for 1000 orbits, it is 37.0899 km. These values also lie between the corresponding purely specular and diffuse reflection results.

4.6.1.2 Varied Despun Platform Area. The results in this section use the two area factors applied to the original despun platform area. The first area factor, five, is used in Figure 4.37.

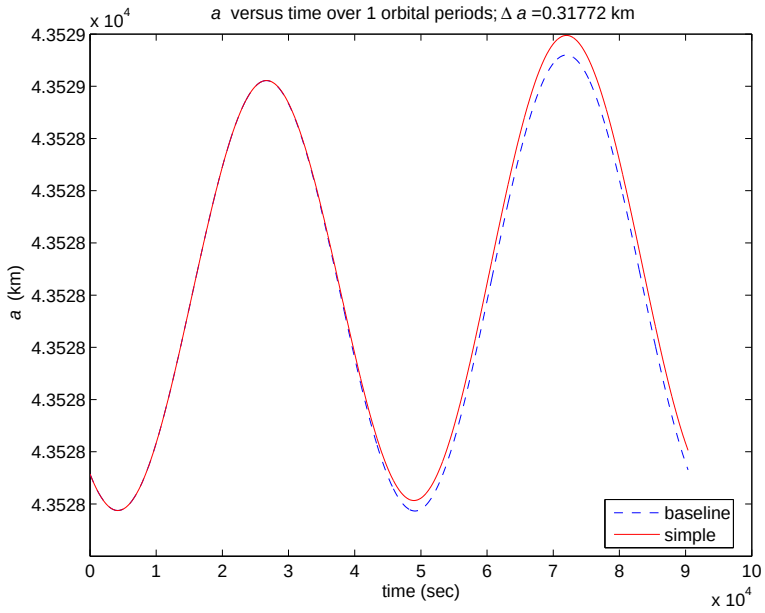

Figure 4.35: Simple Controller Case Behavior of a for 50% Diffuse and 50% Specular Reflection, 1 Orbit and an Area Factor of 1, Overlaid with the Corresponding Baseline Case Behavior of a.

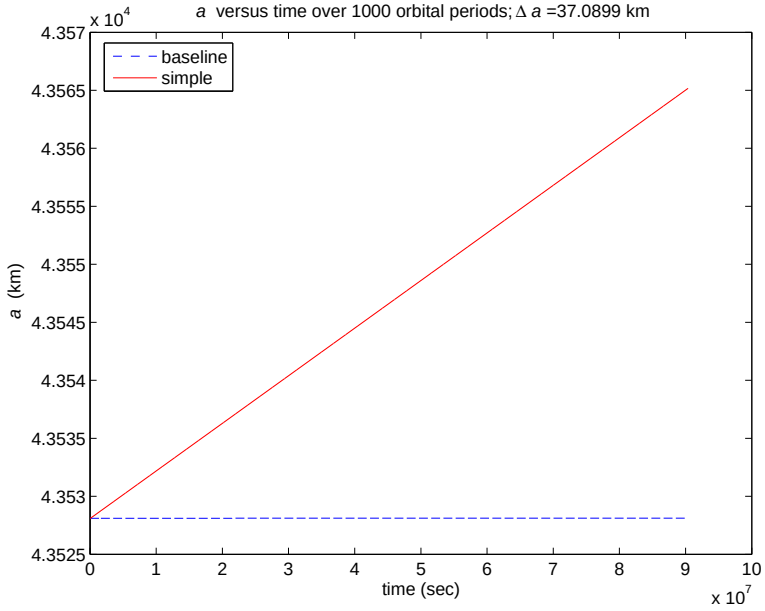

Figure 4.36: Simple Controller Case Behavior of a for 50% Diffuse and 50% Specular Reflection, 1000 Orbits and an Area Factor of 1, Overlaid with the Corresponding Baseline Case Behavior of a.

For one orbit, the resulting change in semimajor axis is 0.53151 km. Over 100 orbits, the total raise is 18.5895 km and for 1000 orbits it is 185.9499 km. Again, these values fall between the purely specular and diffuse reflection values for the same case.

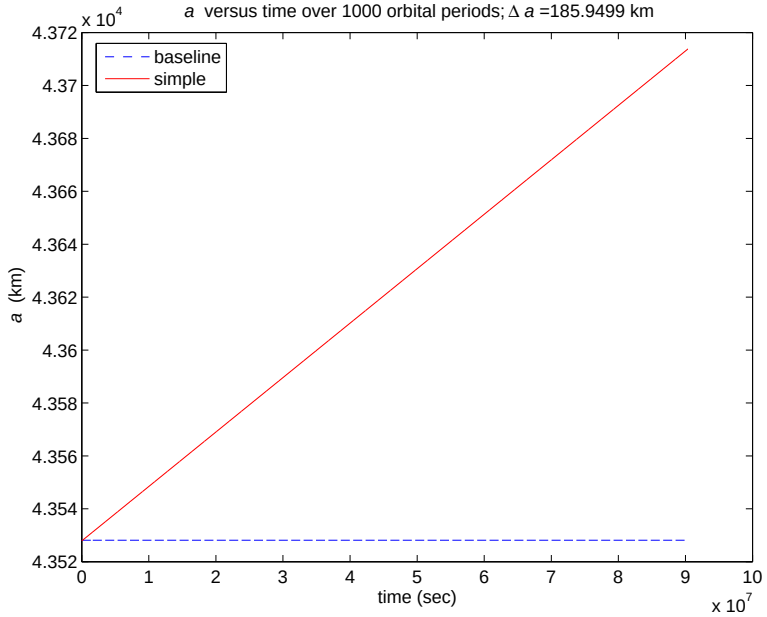

Figure 4.37: Simple Controller Case Behavior of a for 50% Diffuse and 50% Specular Reflection, 1000 Orbits and an Area Factor of 5, Overlaid with the Corresponding Baseline Case Behavior of a.

Figure 4.38 illustrates the resulting changes in semimajor axis when an area factor of ten is applied to the original despun platform area. For one orbit, Δa is 0.79876 km. Over 100 orbits, it is 37.1804 km and over 1000 orbits it is 373.0811 km. Once again, as expected, these values for the raise in semimajor axis fall between the purely specular and purely diffuse results.

4.6.2 Complex Controller Case. This section presents the results for the complex controller described in Section 3.4.2. Again, two subcases were considered: one using the original despun platform area and the second using two area factors applied to the original despun platform area. The percent difference from using the complex controller over the simple controller is approximately 22%.

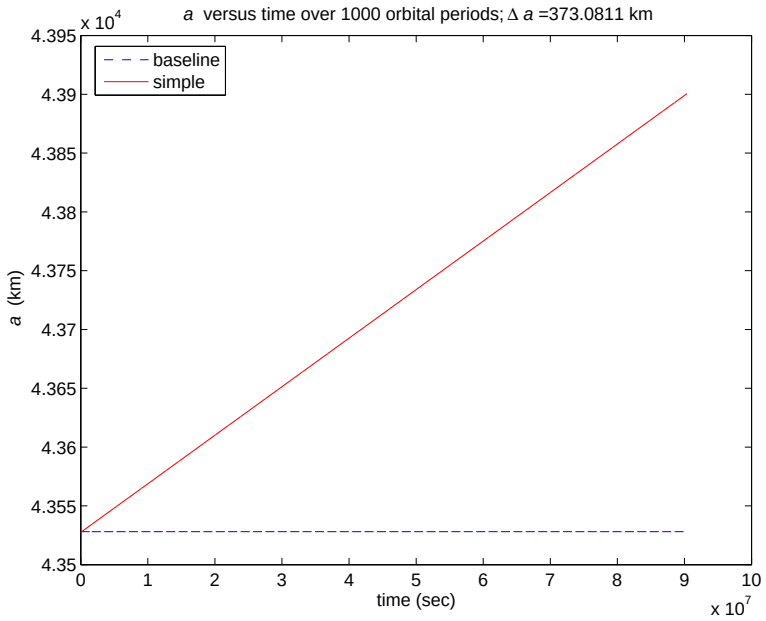

Figure 4.38: Simple Controller Case Behavior of a for 50% Diffuse and 50% Specular Reflection, 1000 Orbits and an Area Factor of 10, Overlaid with the Corresponding Baseline Case Behavior of a.

4.6.2.1 Original Despun Platform Area. Figure 4.39 illustrates the resulting changes in semimajor axis using the complex controller and the original despun platform area of the satellite.

As expected, the values of Δa for this particular case lie between the purely specular and purely diffuse reflection for the corresponding number of orbits. For this scenario, over one orbit, the raise in semimajor axis is 0.3278 km. Over 100 orbits, Δa is 4.4885 km and for 1000 orbits it is 45.1932 km (approximately 10 km more than the simple controller case for mixed reflection and original area).

4.6.2.2 Varied Despun Platform Area. This section details the results when area factors of five and ten are applied to the original despun platform area.

For an area factor of five over one orbit, the raise in semimajor axis is 0.58193 km. Δa is 22.4093 km for 100 orbits and 226.6733 km for 1000 orbits. These values again fall between the corresponding raises in semimajor axis for the specular and diffuse cases.

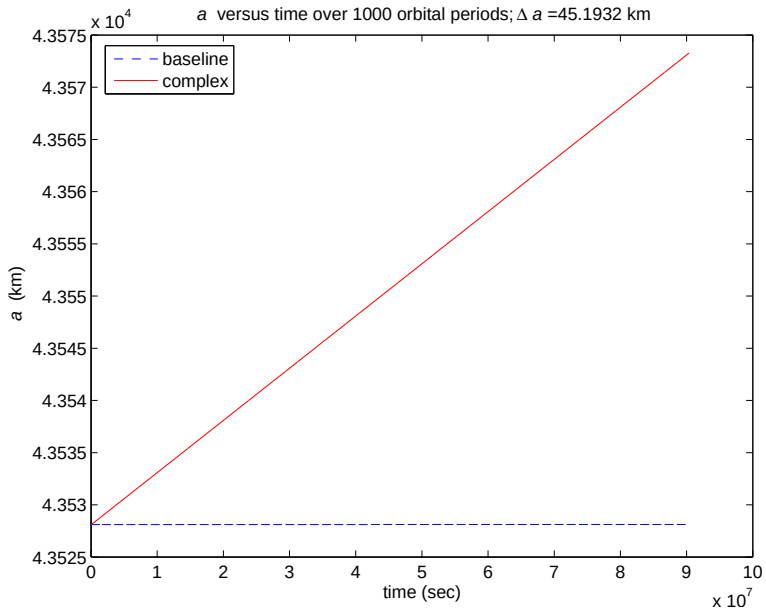

Figure 4.39: Complex Controller Case Behavior of a for 50% Diffuse and 50% Specular Reflection, 1000 Orbits and an Area Factor of 1, Overlaid with the Corresponding Baseline Case Behavior of a.

Figure 4.40 shows the results for an area factor of ten applied to the original despun platform area. For one orbit, the change in semimajor axis is 0.8996 km. Δa is 44.8291 km for 100 orbits and is 455.0825 km for 1000 orbits. These also fall between the values for the specular and diffuse reflection cases.

4.7 Summary of Results

A tabular summary of the results from the thesis is presented in Table 4.1. In Table 4.1, note that for all cases, purely specular reflection results in the largest change in semimajor axis. For the simple controller, the purely diffuse case produces the third best results for semimajor axis change, primarily because the half-diffuse and half-specular mixed case results lie in between the purely specular and purely diffuse results. Notably, the complex controller yields less desirable results than the simple controller for the purely diffuse case, which is likely due to the complex controller being designed to take advantage of completely specular reflection. In fact, the nominal case for

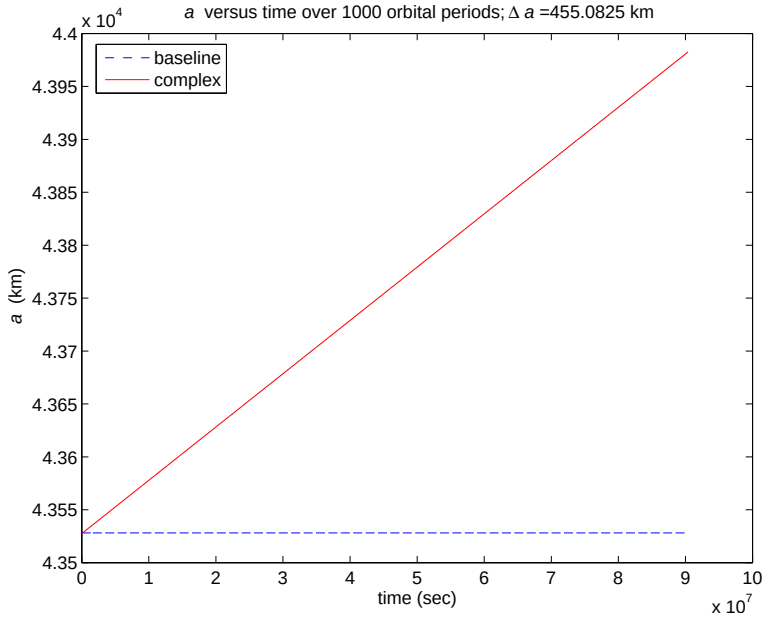

Figure 4.40: Complex Controller Case Behavior of a for 50% Diffuse and 50% Specular Reflection, 1000 Orbits and an Area Factor of 10, Overlaid with the Corresponding Baseline Case Behavior of a.

the complex controller yielded a longer rise in semimajor axis than the diffuse case. The satellite's nominal reflection case, with each coefficient set to one-third, yields results that are slightly less than the purely diffuse case for the simple controller. Finally, as expected, the all absorption case generates the least raise in semimajor axis over all the cases.

Overall, then, the order of effectiveness is:

1. Complex controller with $c_{Rs} = 1$
2. Complex controller with $c_{Rd} = 0.5$ and $c_{Rs} = 0.5$
3. Simple controller with $c_{Rs} = 1$
4. Simple controller with $c_{Rd} = 0.5$ and $c_{Rs} = 0.5$
5. Complex controller with $c_{Rd} = c_{Rs} = c_{Ra} = \frac{1}{3}$
6. Simple controller with $c_{Rd} = 1$
7. Complex controller with $c_{Rd} = 1$
8. Simple controller with $c_{Rd} = c_{Rs} = c_{Ra} = \frac{1}{3}$
9. Simple controller with $c_{Ra} = 1$
10. Complex controller with $c_{Rd} = 1$

Table 4.1: Summary of Results.

Case	Δa (km), the change in semimajor axis from the epoch value								
	1 Orbit			100 Orbits			1000 Orbits		
Area Factor	1	5	10	1	5	10	1	5	10
Baseline	0.3546	0.3546	0.3546	0.0129	0.0129	0.0129	0.0105	0.0105	0.0105
Nominal									
Simple	0.3098	0.4920	0.7197	3.1860	15.8804	31.7532	31.6495	158.7181	318.2681
Complex	0.3147	0.5163	0.7684	3.4266	17.0842	34.1622	34.3087	172.1240	345.1985
Absorption									
Simple	0.2940	0.4129	0.5614	2.1010	10.4542	20.9048	20.7914	104.3709	209.1176
Complex	0.2884	0.3851	0.5056	1.2974	6.4357	12.8627	12.6168	63.2965	126.7702
Specular									
Simple	0.3222	0.5537	0.8431	4.0176	20.0511	40.0860	40.0064	200.5718	402.4059
Complex	0.3400	0.6430	1.0217	5.6209	28.0751	56.1473	56.8227	285.0813	573.5517
Diffuse									
Simple	0.3133	0.5093	0.7544	3.4368	17.1353	34.2684	34.1497	171.3268	343.6828
Complex	0.3156	0.5209	0.7775	3.3594	16.7510	33.4959	33.5575	168.2071	337.7322
Mix									
Simple	0.3177	0.5315	0.7988	3.7267	18.5895	37.1804	37.0899	185.9499	373.0811
Complex	0.3278	0.5819	0.8996	4.4885	22.4093	44.8291	45.1932	226.6733	455.0825

As the main objective of the thesis is to raise the semimajor axis of the DSCS II satellite into a disposal orbit, it is beneficial to address the length of time required to do this. Based on a linear extrapolation of the nominal absorption and reflection results for the complex controller and an area factor of one (so as to use the satellite's actual estimated area), the time required to raise the DSCS II 400 km would be about 33 years, or about 12000 orbits.

Comparatively, the time required is roughly divisible by the area multiplication factor used (keeping a constant mass of 611 kg); a change of 400 km could be reached in approximately 6.6 years if the area of the satellite was five times the original area, and only 3.3 years if it was ten times more. Hence, perhaps the best takeaway from the results chapter is that even a small change in apparent area (area of the satellite facing the Sun) yields a significantly shorter time required to raise the satellite into a disposal orbit. This point is reinforced in Figure 4.41, which illustrates the effects of changing areas and surface reflection properties on the time-to-disposal. Incidently, this effect is not a surprise, as the control force available is linearly proportional to the controlled area.

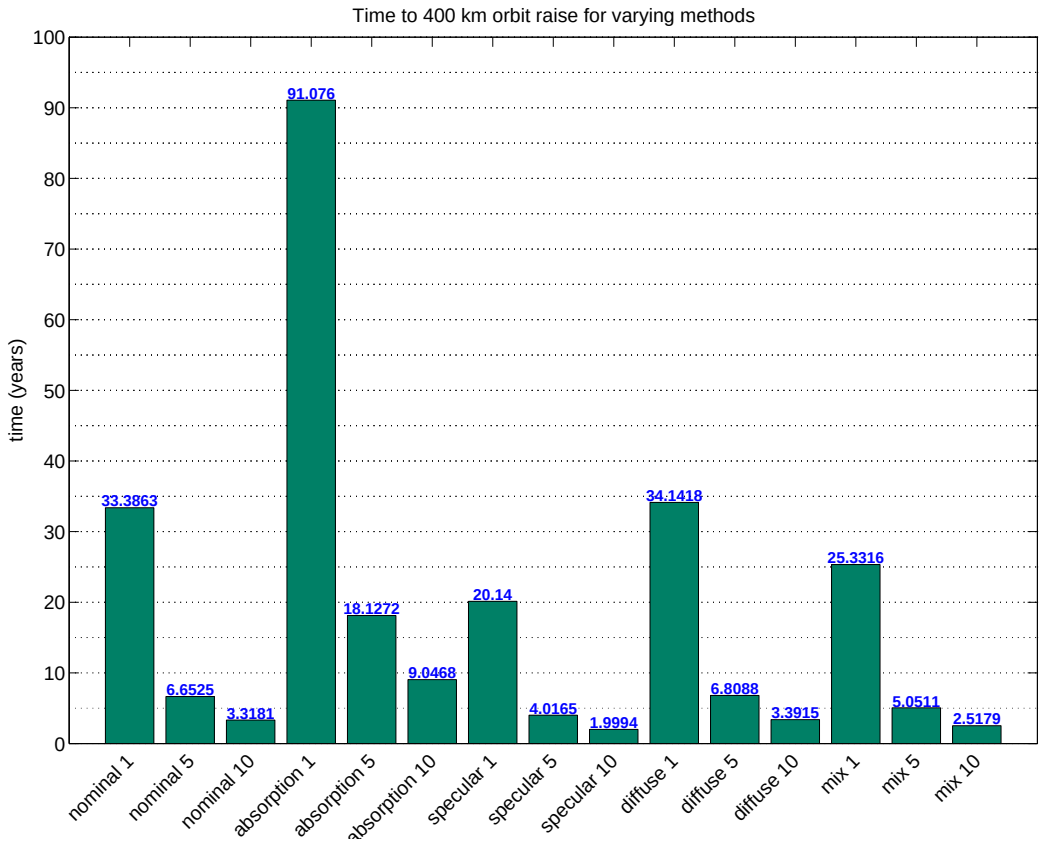

Figure 4.41: Time (in Years) to 400 km versus Case for Complex Controller. The plot illustrates how much time is required to raise the orbit for differing area factors and coefficients of absorption and reflection. The case type and area factor are labeled on the x-axis.

The complex controller case with an area factor of ten and purely specular reflection yields the fastest time-to-disposal (approximately two years). For the original area, the specular case again provides the least amount of time required for disposal, which reflects the optimization of the complex controller for pure specular reflection. Hence, the nominal ("best guess" for the satellite) cases yield more desirable results than both the pure absorption and diffuse reflection cases. These results are also consistent with the equations for the perturbed acceleration due to SRP from Chapter III, since pure specular reflection results in the highest potential force per unit area (as illustrated in Figures 3.3 and 3.4).

If instead the satellite is best modeled as a mix of specular and diffuse reflection, which is most likely a relatively good approximation also as the majority of the satellite is composed of highly polished surfaces (the solar arrays), the time-to-disposal decreases from the nominal case by about 8 years. If the area of the satellite's despun platform was increased by a factor of five, from roughly 5 m^2 to 25 m^2 (or 2.7 m by 6.1 m versus 1.2 m by 2.7 m), both the nominal and mixed reflection cases would enable the satellite to reach a 400 km raise in approximately 5 or 6 years. Although a retrofit to the in-orbit DSCS II F-13 modeled in this thesis would be costly (and unnecessary, as if astronauts were to retrofit it, they might as well dismantle it and bring it down from orbit), this is an interesting consideration for future satellites. Instead of thrusters and fuel, future satellites could store a small deployable solar sail with which to maneuver (using electric power) into a disposal orbit at the end of their mission lives.

In short, the two factors which have the most effect on the amount of time it takes to raise a satellite into a disposal orbit are the area-to-mass ratio and the optical properties of the satellite surfaces. There does not appear to be a "preferred" area, as the disposal time versus the area was essentially linear throughout the region simulated. Additional comments on the results, as well as suggested further work, can be found in Chapter V.

V. Conclusions and Recommendations

5.1 Summary and Conclusions

This thesis has demonstrated that solar radiation pressure, as the most significant non-gravitational perturbation, does have the potential to raise geosynchronous satellite into disposal orbits. Using a controller, the satellite can be maneuvered to optimize the direction of incident solar radiation on its surface, thus using the force from SRP to raise the satellite into a disposal orbit. Several factors control the accuracy of the model; conical versus cylindrical Earth shadow (the satellite spends on the order of 5% and 1% of the orbital period in shadow, respectively [19, 20]), constant versus varying solar flux (about a 7% difference between minimum and maximum values), constant versus changing cross-sectional area of the satellite, and the optical properties of the satellite surface (absorption, reflection, and transmission). A derivation of the SRP model incorporating a cylindrical Earth shadow and time-varying solar flux was developed in Chapter III. In turn, numerical and analysis results were presented in Chapter IV.

Despite the potential of SRP, it is clear that it may not be a practical solution for existing spacecraft. Under the best-performing surface properties (purely specular reflection) and using the best controller, the time-to-disposal is on the order of 20 years for the DSCS II satellite considered in this work. The satellite, however, most likely retains surface characteristics similar to either the nominal (all coefficients of reflection and absorption set equal to 1/3) or mixed (the coefficients of specular and diffuse reflection each set equal to 1/2) cases. As the complex controller provides the largest change in semimajor axis for these two cases, reference Figure 4.41 for the corresponding times-to-disposal of approximately 33 years (nominal) and 25 years (mixed). For larger area-to-mass ratios, the time required to raise the DSCS II F-13 satellite 400 km is lowered as one over the area factor. Hence, a small change in area has a large effect on the time-to-disposal of the satellite, as does small changes in material properties of the satellite's surfaces. This offers hope that new systems designed to take advantage of SRP could achieve much better disposal times.

5.2 Recommendations for Future Work

Future research related to this thesis would prove to be beneficial in estimating to a higher order of accuracy the time required to move the DSCS II satellites into disposal orbits. Several simplifications were made in the thesis which, if included in later work, would yield a more likely estimate.

A conical shadow model, while more difficult to implement, is a more accurate representation of the Earth's shadow than the cylindrical model. Modeling the shadow as such would enable the researcher to study the transition effects of the spacecraft through the regions of the umbra and penumbra. The use of a cylindrical model neglects these transition regions; it models the shadow as having only the dark, or umbra, regions. This, in turn, causes the solar radiation pressure to only appear "off" (satellite in the umbra) or "on" (satellite in sunlight). The amount of time spacecraft spend out of the shadow region directly correlates to the amount of time needed to raise its orbit, and a better model for the shadow would produce a more accurate value for this time-to-disposal. An alternate approach would be to model the cylindrical shadow with a reduced size; this would test the importance of the shadow as it affects the solution.

Also of importance is the method developed by Coverstone et. al. for the complex controller. In additions to the modifications made in this thesis (reference Chapter I) to account for the inclination of the Earth with respect to the ecliptic plane, future work could further modify her model to include absorption, diffuse reflection and transmission of the incident solar ray on the surface of the satellite. As her model only includes specular reflection, the results are certainly skewed to favor the case with purely specular reflection. The inclusion of more complex surface properties of the satellite would generate potentially different results.

If continual interest in raising the orbits of the DSCS II satellites were present, future work should include better data (if possible) on the properties of the satellites. Although the properties of the satellite, to include mass, area, dimensions of the parabolic antennae and coefficients of

reflection and absorption, were reasonably know at the time of launch more than 20 years ago, the current values are not as readily available. As the results show, these values can have a profound impact on the time required to dispose of the satellite into a higher orbit. Of particular interest is the parabolic antennae; this thesis uses a flat plate approximation for them, and having the appropriate dimensions available would enable a more realistic propagation.

Applying this method to other aging satellites in orbit might also be interesting, particularly for satellites of different area-to-mass ratios and those in different orbits than geosynchronous. An important system-level trade-off consideration would be the fuel mass needed for disposal versus the mass required to store, deploy and control a large area "disposal sail". Of course, if used for satellites in lower orbits (less than 800 km), drag will quickly become the highest-order non-gravitational perturbation instead of SRP.

The author believes that additional study of using SRP to dispose of satellites otherwise incapable of being moved into disposal orbits will remain of interest. As long as the demand for newer (or simply more) satellites in high-value orbits such as the geosynchronous belt exists, researchers will continue to be tasked to address how to dispose of satellites that have reached the end of their mission life. For existing dual-spin satellites like the DSCS II modeled in this thesis, however, this method is unlikely a practical option. Instead, future work could be performed to investigate applications with a three-axis satellite with large solar array panels (much like the current constellation of DSCS III satellites). The larger area may be able to be controlled to both provide sufficient power and perform orbit raising. Another potential use is for geosynchronous satellite stationkeeping; if the design of the satellite included a sail-type device, it could be used for both stationkeeping throughout the satellite's mission life and for disposal at end-of-life.

Appendix A. DSCS II TLE and Satellite Parameters

A.1 Interpreting the Two-Line Element Set

The most common method for communicating orbit information is the TLE. This format, used by NASA and the North American Aerospace Defense Command (NORAD), consists of three lines of information that can be deciphered to obtain the properties of the satellite and its current position in orbit about the Earth.

A TLE has one line consisting of a 24-character name (line 0) and two 69-character lines of data (lines 1 and 2). The only valid characters in the lines are the numbers 0-9, the capital letters A-Z, the period, the space, and the plus and minus signs. There are further restrictions on the elements of each line, which are detailed on the CelesTrak website (*http://celestrak.com*). The generic format of a TLE is

```
AAAAAAAAAAAAAAAAAAAAAAA
1 NNNNNU NNNNNAAA NNNNN.NNNNNNNN +.NNNNNNNN +NNNNN-N +NNNNN-N N NNNNN
2 NNNNN NNN.NNNN NNN.NNNN NNNNNNN NNN.NNNN NNN.NNNN NN.NNNNNNNNNNNNNN
```

Tables A.1 and A.2 define each of the individual fields for lines 1 and 2, respectively [15, 21].

The code presented in Appendix C requires the input of most of the parameters in the TLE, and uses them to calculate the classical orbital elements at epoch. The TLE used for this thesis is [28]

```
OPS 9443
1 11621U 79098A   05202.40912884 -.00000117  00000-0  10000-3 0  8408
2 11621 014.4997 018.8800 0005671 321.5388 038.4719 00.95598989542422
```

Table A.1: TLE Line 1 Description.

Column	Description
01	Line number of element data
03-07	Satellite number (from NORAD number)
08	Classification of TLE (U=Unclassified and C=Classified)
10-11	International designator (last two digits of launch year)
12-14	International designator (launch number of the year)
15-17	International designator (piece of the launch)
19-20	Epoch year (only the last two digits)
21-32	Epoch (day of the year and fraction of the day)
34-43	First time derivative of the mean motion or ballistic coefficient*
45-52	Second time derivative of the mean motion (decimal point assumed)
54-61	B^* drag term (decimal point assumed) or radiation pressure coefficient‡
63	Ephemeris type
65-68	Element number
69	Checksum value

*depends on ephemeris type
$^\ddagger B^*$ if GP4 general perturbation theory was used

Table A.2: TLE Line 2 Description.

Column	Description
01	Line number of element data
03-07	Satellite number
09-16	Inclination (degrees)
18-25	Right ascension of the ascending node (degrees)
27-33	Eccentricity (decimal point assumed)
35-42	Argument of perigee (degrees)
44-51	Mean anomaly (degrees)
53-63	Mean motion (revolutions per day)
64-68	Revolution number at epoch (revolutions)
69	Checksum value

A.2 DSCS II F-13 Data

The DSCS satellite system, of which a typical Phase II satellite is illustrated in Figure A.1, is a United States military satellite constellation that was placed in a geosynchronous orbit to provide secure voice and data communications to the military user. The DSCS system succeeded the Initial Defense Satellite Communications System (IDSCS) program, which launched its first satellite into orbit in 1966.

Several reputable sources are available for determining the characteristics of the DSCS satellites, however, they often do not agree on specifics. *Jane's All the World's Aircraft*, for example, assumes that each DSCS satellite has the same specifications. NASA gives details for each satellite launched, but leaves out some necessary details. The specifications, as merged from both sources for the DSCS II satellite used in the thesis, are outlined in Table A.3 [23, 37].

Table A.3: DSCS II F-13 Specifications.

Parameter	Value	Units
mass	611	kg
Spin-Stabilized Platform		
height	1.8288	m
diameter	2.7432	m
surface area	5.0168	m^2
Despun Platform		
height	1.2192	m
width	2.7432	m
surface area†	3.3445	m^2

†estimated approximate surface area

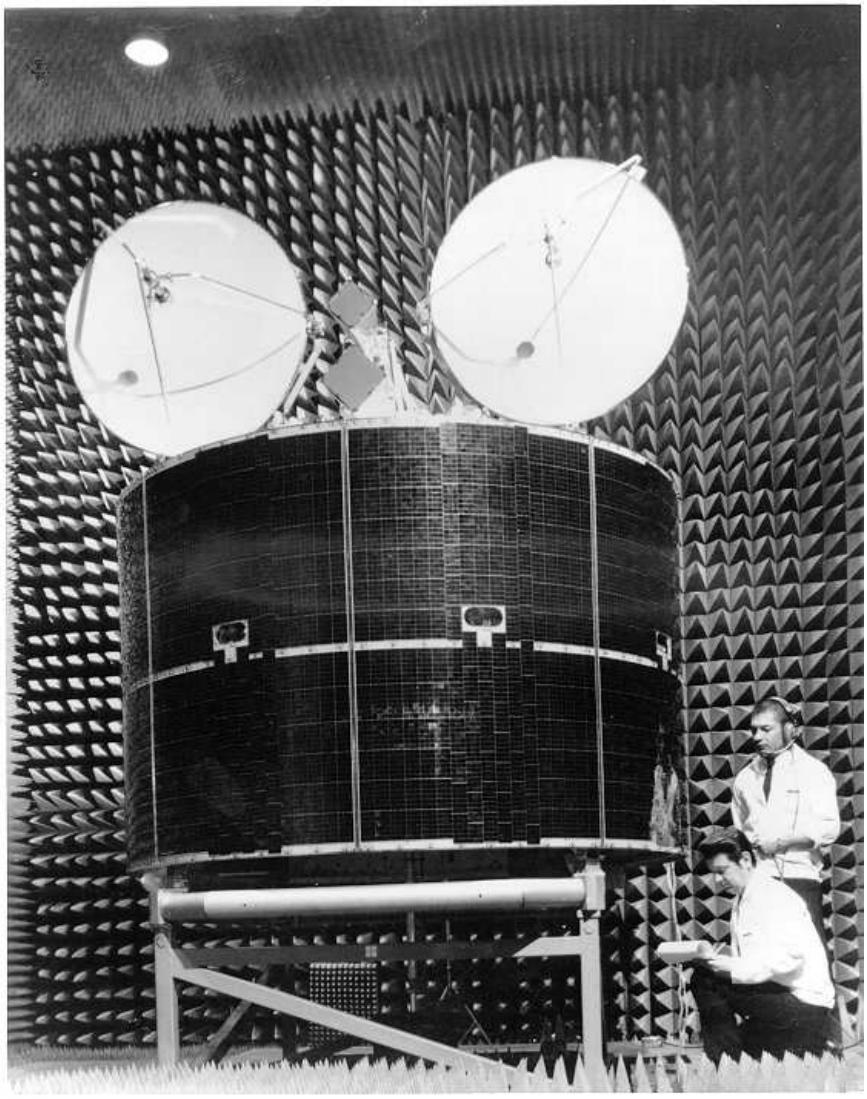

Figure A.1: DSCS II Satellite [1]. Photo courtesy of NASA JPL.

Appendix B. Aphelion Almanac

The Earth reaches aphelion around 4 July annually. The variance in date per year is well documented in the *Astronomical Almanac*, published by the United States Naval Observatory's Astronomical Applications Department. Table B.1 is taken from the larger database, which can be found on their website. Here, d, h and m indicate day, hour and minute, respectively, in Universal Time [31].

Table B.1: Earth Aphelion Dates for Years 2005-2020.

Year	Month	d	h	Day of Year
2005	July	5	05	186
2006	July	3	23	184
2007	July	7	00	188
2008	July	4	08	186
2009	July	4	02	185
2010	July	6	11	187
2011	July	4	15	185
2012	July	5	03	187
2013	July	5	15	186
2014	July	4	00	185
2015	July	6	19	187
2016	July	4	16	186
2017	July	3	20	184
2018	July	6	17	187
2019	July	4	22	185
2020	July	4	12	186

Appendix C. MATLAB® *Source Code*

The MATLAB® code is presented in alphabetical order by m-file. To facilitate better understanding of the overall code hierarchy, reference Figure C.1.

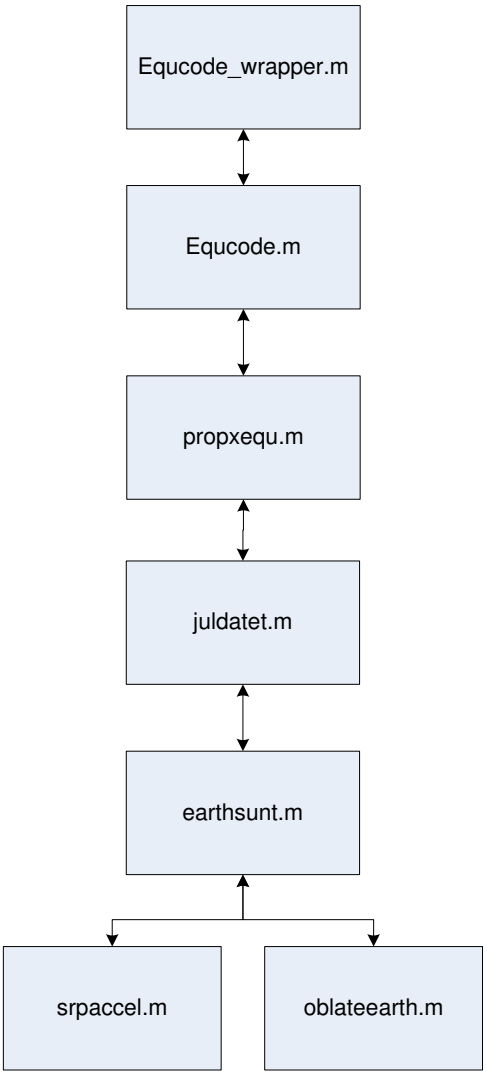

Figure C.1: Basic MATLAB® m-file Structure.

C.1 CALCEA.m

```
% Solves for eccentric anomaly, E from a given mean anomaly, M
% and eccentricty, e.  Performs a simple Newton-Raphson iteration
%
% M must be in radians and E is returned in radians.
%
% Default tolerances is 10^-8 rad.
%
% E = CalcEA(M,e) uses default tolerances
%
% E = CalcEA(M,e,tol) will use a user specified tolerance, tol
%
% Richard Rieber
% 1/23/2005
% E-mail problems/suggestions rrieber@gmail.com

function E = CalcEA(M,e,tol)

%Checking for user inputed tolerance
if nargin == 2
    %using default value
    tol = 10^-8;
elseif nargin > 3
    error('Too many inputs.  See help CalcE')
elseif nargin < 2
    error('Too few inputs.  See help CalcE')
end

Etemp = M; ratio = 1; while abs(ratio) > tol
    f_E = Etemp - e*sin(Etemp) - M;
    f_Eprime = 1 - e*cos(Etemp);
    ratio = f_E/f_Eprime;
    if abs(ratio) > tol
        Etemp = Etemp - ratio;
    else
        E = Etemp;
    end
end
```

C.2 earthsun.m

```
function r_ES_vec = earthsun(epoch_yr,epoch_day,epoch_frac)
% This function calculates the position vector between the
% earth and the sun for the calculated JD in UTC.  Note that this algorithm
% is only valid until the year 2050 due to truncation (see Vallado pg 265).

%~~~~~~~~~~~~~~~~~~~~~~~~~~~~~~~~~~~~~~~~~~~~~~~~~~~~~~~~~~~~~~~~~~~~~~~~~~~~
% note all of these values must be in degrees, not radians!!!
%~~~~~~~~~~~~~~~~~~~~~~~~~~~~~~~~~~~~~~~~~~~~~~~~~~~~~~~~~~~~~~~~~~~~~~~~~~~~
```

```
JD = juldate(epoch_yr,epoch_day,epoch_frac);
    % JD is in ref to UTC (let JD_UTC = JD_UT1)

% find the number of Julian centuries
T_UT1 = (JD - 2451545.0)/36525;                 % Vallado pg 188

lambda_M_sundeg = 280.460 + 36000.770*T_UT1;    % deg
T_TDB = T_UT1;
M_sundeg = 357.5277233 + 35999.05034*T_TDB;     % deg
lambda_ecliptic = lambda_M_sundeg + 1.914666471*sind(M_sundeg) +
...
    0.019994643*sind(2*M_sundeg);               % deg
r_sun = 1.000140612 - 0.016708617*cosd(M_sundeg) -...
    0.000139589*cos(2*M_sundeg);  % AU
epsilon = 23.439291 - 0.0130042*T_TDB;          % deg

% the vector referred to the epoch of date is (in AU)
r_ES_vecAU = [r_sun*cosd(lambda_ecliptic);...
    r_sun*cosd(epsilon)*sind(lambda_ecliptic);...
    r_sun*sind(epsilon)*sind(lambda_ecliptic)];

r_ES_vec = 149598000.*r_ES_vecAU;    % Sun-Earth vector in km

% also calculate the right ascension and declination of the sun (can check
% with Astronomical Almanac)
alpha_sun = atand(cosd(epsilon)*tand(lambda_ecliptic)); delta_sun
= asind(sind(epsilon)*sind(lambda_ecliptic));

return
```

C.3 earthsunt.m

```
function r_ES_vec = earthsunt(t)
% This function calculates the position vector between the
% earth and the sun for the calculated JD in UTC.  Note that this algorithm
% is only valid until the year 2050 due to truncation (see Vallado pg 265).

%~~~~~~~~~~~~~~~~~~~~~~~~~~~~~~~~~~~~~~~~~~~~~~~~~~~~~~~~~~~~~~~~~~~~~~~~~~~~
% note all of these values must be in degrees, not radians!!!
%~~~~~~~~~~~~~~~~~~~~~~~~~~~~~~~~~~~~~~~~~~~~~~~~~~~~~~~~~~~~~~~~~~~~~~~~~~~~

JD = juldatet(t);     % JD is in ref to UTC (let JD_UTC = JD_UT1)

% find the number of Julian centuries
T_UT1 = (JD - 2451545.0)/36525;     % Vallado pg 188

lambda_M_sundeg = 280.460 + 36000.770*T_UT1;    % deg
T_TDB = T_UT1;

M_sundeg = 357.5277233 + 35999.05034*T_TDB;     % deg
lambda_ecliptic = lambda_M_sundeg + 1.914666471*sind(M_sundeg) +
```

```
...
    0.019994643*sind(2*M_sundeg);               % deg
r_sun = 1.000140612 - 0.016708617*cosd(M_sundeg) -...
    0.000139589*cosd(2*M_sundeg); % AU
epsilon = 23.439291 - 0.0130042*T_TDB;          % deg

% the vector referred to the epoch of date is (in AU)
r_ES_vecAU = [r_sun*cosd(lambda_ecliptic);...
    r_sun*cosd(epsilon)*sind(lambda_ecliptic);...
    r_sun*sind(epsilon)*sind(lambda_ecliptic)];

r_ES_vec = 149598000.*r_ES_vecAU;    % Sun-Earth vector in km

% also calculate the right ascension and declination of the sun (can check
% with Astronomical Almanac)
alpha_sun = atand(cosd(epsilon)*tand(lambda_ecliptic)); delta_sun
= asind(sind(epsilon)*sind(lambda_ecliptic));

return
```

C.4 EQUcode.m

```
% This m-file is called by the executable, EQUcode_wrapper.m

%~~~~~~~~~~~~~~~~~~~~~~~~~~~~~~~~~~~~~~~~~~~~~~~~~~~~~~~~~~~~~~~~~~~~~~~~~~~~~
% Define initial orbital parameters for the DSCS II F-13 geostationary
% satellite based on a two line element set at specific UTC (epoch at yr 05
% day 202 fraction .40912884)
%~~~~~~~~~~~~~~~~~~~~~~~~~~~~~~~~~~~~~~~~~~~~~~~~~~~~~~~~~~~~~~~~~~~~~~~~~~~~~

% Line 2 of TLE:
BC_o = -.00000117;                      % ballistic coefficient
epoch_yr = 2005;                        % year in 4-digit format
epoch_day = 202; epoch_frac = .40912884;
    JD_o = juldate(epoch_yr,epoch_day,epoch_frac);

% Line 3 of TLE:
i_o_deg = 14.4997;                      % inclination (deg)
    i_o = i_o_deg*2*pi()/360;           % inclination (rad)
RAAN_o_deg = 18.8800;
    % right ascension of the ascending node (deg)
    RAAN_o = RAAN_o_deg*2*pi()/360;
        % right ascension of the ascending node (rad)
e_o = 0.0005671;                        % eccentricity (dimensionless)
omega_o_deg = 321.5388;                 % argument of perigee (deg)
    omega_o = omega_o_deg*2*pi()/360;   % argument of perigee (rad)
M_o_deg = 38.4719;                      % mean anomaly (deg)
    M_o = M_o_deg*2*pi()/360;           % mean anomaly (rad)
n_o_rev = .95598989;                    % mean motion (rev/day)
    n_o = n_o_rev*(2*pi()/86400);       % mean motion (rad/sec)
revnum_o = 54242;                       % revolution number at epoch (rev)
```

```
%~~~~~~~~~~~~~~~~~~~~~~~~~~~~~~~~~~~~~~~~~~~~~~~~~~~~~~~~~~~~~~~~~~~~~~~~~~~~
% Calculate initial parameters:
%~~~~~~~~~~~~~~~~~~~~~~~~~~~~~~~~~~~~~~~~~~~~~~~~~~~~~~~~~~~~~~~~~~~~~~~~~~~~

a_o = (mu_earth/n_o^2)^(1/3);          % semimajor axis (km), Hale pg 66

ra_o = a_o*(1 + e_o);                  % radius of apoapsis (km), Hale
rp_o = a_o*(1 - e_o);                  % radius of periapsis (km), Hale

ha_o = ra_o - R_earth;                 % height of apoapsis (km), Hale
hp_o = rp_o - R_earth;                 % height of periapsis (km), Hale

T_o = 2*pi()*sqrt(a_o^3/mu_earth);
    % approximate period of orbit (sec), Hale pg 62 (unperturbed)
T_o_hr = T_o/(60*60);
    % approximate period of orbit (hr) (unperturbed)
Energy_o = -mu_earth/(2*a_o);
    % total specific mechanical energy (km^2/sec^2), Hale pg 18
t_o = (T_o/(2*pi()))*M_o;
    % time elapsed from perigee passage (sec), Hale pg 63

% Eccentric anomaly evaluation using Newton-Raphson iteration
E_o = CalcEA(M_o,e_o,1e-10);

nu_o = 2*atan(sqrt((1+e_o)/(1-e_o))*tan(E_o/2)); % true anomaly (rad), Hale
r_o = a_o*(1 - e_o*cos(E_o));      % instantaneous radius of s/c (km), Hale
h_o = r_o - R_earth;               % instantaneous altitude of s/c (km)
rho = rho_s*exp(-beta*h_o);        % density at h_o (kg/km^3)

%~~~~~~~~~~~~~~~~~~~~~~~~~~~~~~~~~~~~~~~~~~~~~~~~~~~~~~~~~~~~~~~~~~~~~~~~~~~~
% Calculate the geocentric position vector of the Sun:
%~~~~~~~~~~~~~~~~~~~~~~~~~~~~~~~~~~~~~~~~~~~~~~~~~~~~~~~~~~~~~~~~~~~~~~~~~~~~

r_ES_vec = earthsun(epoch_yr,epoch_day,epoch_frac);  % returns in units of km

%~~~~~~~~~~~~~~~~~~~~~~~~~~~~~~~~~~~~~~~~~~~~~~~~~~~~~~~~~~~~~~~~~~~~~~~~~~~~
% Calculate the initial modified equinoctial (MEE) element set:
%~~~~~~~~~~~~~~~~~~~~~~~~~~~~~~~~~~~~~~~~~~~~~~~~~~~~~~~~~~~~~~~~~~~~~~~~~~~~

p_o = a_o*(1 - e_o^2);                 % semilatus rectum (km)
f_o = e_o*cos(omega_o + RAAN_o); g_o = e_o*sin(omega_o + RAAN_o);
h_o = tan(i_o/2)*cos(RAAN_o); k_o = tan(i_o/2)*sin(RAAN_o);
L_o = RAAN_o + omega_o + nu_o;         % true longitude

%~~~~~~~~~~~~~~~~~~~~~~~~~~~~~~~~~~~~~~~~~~~~~~~~~~~~~~~~~~~~~~~~~~~~~~~~~~~~
% Call function mequtorv to convert the initial modified MEE
% element set to inital r and v vectors
%~~~~~~~~~~~~~~~~~~~~~~~~~~~~~~~~~~~~~~~~~~~~~~~~~~~~~~~~~~~~~~~~~~~~~~~~~~~~

x_o_vec = mequtorv(p_o, f_o, g_o, h_o, k_o, L_o);
```

```
    % of the form [xo; yo; zo; xdoto; ydoto; zdoto] with r components in km
    % and v components in km/sec

r_o = [x_o_vec(1); x_o_vec(2); x_o_vec(3)]; v_o = [x_o_vec(4);
x_o_vec(5); x_o_vec(6)];

%~~~~~~~~~~~~~~~~~~~~~~~~~~~~~~~~~~~~~~~~~~~~~~~~~~~~~~~~~~~~~~~~~~~~~~~~~~~~~~~
% Call function propxequ to propagate the state vector x from x_o using
% the relationship xdot = f(x,t)
%~~~~~~~~~~~~~~~~~~~~~~~~~~~~~~~~~~~~~~~~~~~~~~~~~~~~~~~~~~~~~~~~~~~~~~~~~~~~~~~
aa = 1; equo_vec = [p_o; f_o; g_o; h_o; k_o; L_o];

ti = 0; options=odeset('MaxStep',MaxStep); [t,x] =
ode45(@propxequ, [ti n*T_o],equo_vec,options);
% [t,x] = ode45(@propxequ,tspan,equo_vec,options); % uncomment to output a
% vector with specific time intervals; use with STK results to plot error

poft = x(:,1); foft = x(:,2); goft = x(:,3); hoft = x(:,4); koft =
x(:,5); Loft = x(:,6);

%~~~~~~~~~~~~~~~~~~~~~~~~~~~~~~~~~~~~~~~~~~~~~~~~~~~~~~~~~~~~~~~~~~~~~~~~~~~~~~~
% compute r(t) and v(t) based on the MEE elements
%~~~~~~~~~~~~~~~~~~~~~~~~~~~~~~~~~~~~~~~~~~~~~~~~~~~~~~~~~~~~~~~~~~~~~~~~~~~~~~~

for i=1:length(poft)
    alpha = sqrt(hoft(i)^2 - koft(i)^2);
    s = sqrt(1 + hoft(i)^2 + koft(i)^2);
    w = 1 + foft(i)*cos(Loft(i)) + goft(i)*sin(Loft(i));
    r = poft(i)/w;

    r1 = (r/s^2)*(cos(Loft(i)) + alpha^2*cos(Loft(i)) +...
        2*hoft(i)*koft(i)*sin(Loft(i)));
    r2 = (r/s^2)*(sin(Loft(i)) - alpha^2*sin(Loft(i)) +...
        2*hoft(i)*koft(i)*cos(Loft(i)));
    r3 = (2*r/s^2)*(hoft(i)*sin(Loft(i)) - koft(i)*cos(Loft(i)));
    r = [r1 r2 r3];

    v1 = (-1/s^2)*sqrt(mu_earth/poft(i))*(sin(Loft(i)) + alpha^2*sin(Loft(i))...
        - 2*hoft(i)*koft(i)*cos(Loft(i)) + goft(i) - 2*foft(i)*hoft(i)*koft(i)...
        + alpha^2*goft(i));
    v2 = (-1/s^2)*sqrt(mu_earth/poft(i))*(-cos(Loft(i)) + alpha^2*cos(Loft(i))...
        + 2*hoft(i)*koft(i)*sin(Loft(i)) - foft(i) + 2*goft(i)*hoft(i)*koft(i)...
        + alpha^2*foft(i));
    v3 = (2/s^2)*sqrt(mu_earth/poft(i))*(hoft(i)*cos(Loft(i)) +...
        koft(i)*sin(Loft(i)) + foft(i)*hoft(i) + goft(i)*koft(i));
    v = [v1 v2 v3];

    rvec = [rvec; r];
    vvec = [vvec; v];
end
```

```
%~~~~~~~~~~~~~~~~~~~~~~~~~~~~~~~~~~~~~~~~~~~~~~~~~~~~~~~~~~~~~~~~~~~~~~~~~~~~
% convert MEE set back to Keplerian element set:
%~~~~~~~~~~~~~~~~~~~~~~~~~~~~~~~~~~~~~~~~~~~~~~~~~~~~~~~~~~~~~~~~~~~~~~~~~~~~

for ii = 1:length(x)
    a = poft(ii)/(1 - foft(ii)^2 - goft(ii)^2); % semimajor axis (km)
    a_vec = [a_vec a];

    e = sqrt((foft(ii))^2 + (goft(ii))^2); % eccentricity (dimensionless)
    e_vec = [e_vec e];

    i = atan2(2*sqrt((hoft(ii))^2 + (koft(ii))^2),1-hoft(ii)^2-koft(ii)^2);
        % inclination (rad)
    i_vec = [i_vec i]; % rad

    w = atan2(goft(ii)*hoft(ii)-foft(ii)*koft(ii),foft(ii)*hoft(ii)+...
        goft(ii)*koft(ii));
        % argument of periapsis (rad)
    w = rad2deg(w); % deg
    w = zero22pi(w); % deg
    w_vec = [w_vec w]; % deg

    RAAN = atan2(koft(ii),hoft(ii));
        % right ascension of the ascending node (rad)
    RAAN = rad2deg(RAAN); % deg
    RAAN_vec = [RAAN_vec RAAN]; % deg

    nu = Loft(ii) - (atan2(koft(ii),hoft(ii)) +...
        atan2(goft(ii)*hoft(ii)-foft(ii)*koft(ii),foft(ii)*hoft(ii)+...
        goft(ii)*koft(ii))); % true anomaly (rad)
    nu = rad2deg(nu);   % deg
    nu = zero22pi(nu);  % deg
    nu_vec = [nu_vec nu]; % deg

    u = atan2(hoft(ii)*sin(Loft(ii))-koft(ii)*cos(Loft(ii)),...
        hoft(ii)*cos(Loft(ii))+koft(ii)*sin(Loft(ii)));
        % argument of latitude
    u_vec = [u_vec u];
end

i_vec_deg = i_vec.*180/pi();        % deg
w_vec_deg = w_vec;

%~~~~~~~~~~~~~~~~~~~~~~~~~~~~~~~~~~~~~~~~~~~~~~~~~~~~~~~~~~~~~~~~~~~~~~~~~~~~
% Calculate misc. parameters of interest
%~~~~~~~~~~~~~~~~~~~~~~~~~~~~~~~~~~~~~~~~~~~~~~~~~~~~~~~~~~~~~~~~~~~~~~~~~~~~

rp_vec = a_vec.*(1 - e_vec); % perigee altitude (km)

OrbitRaise = a_vec(length(a_vec))-a_vec(1); a_end =
a_vec(length(a_vec));
```

```
elapsedtime_days = n*T_o/60/60/24; elapsedtime_years =
n*T_o/60/60/24/365;

omega_i = w_vec_deg(1); omega_f = w_vec_deg(end);

i_i = i_vec_deg(1); i_f = i_vec_deg(end);

RAAN_i = RAAN_vec(1); RAAN_f = RAAN_vec(end);

xx = polyfit(t',a_vec,1); polx = xx(1)*t+xx(2); a_change =
polx(length(polx))-polx(1);

%~~~~~~~~~~~~~~~~~~~~~~~~~~~~~~~~~~~~~~~~~~~~~~~~~~~~~~~~~~~~~~~~~~~~~~~~~~~~
% plot:
%~~~~~~~~~~~~~~~~~~~~~~~~~~~~~~~~~~~~~~~~~~~~~~~~~~~~~~~~~~~~~~~~~~~~~~~~~~~~

% uncomment figs 1-3 for baseline case plots

% figure(1)
% subplot(2,1,1);
% plot(t,rvec(:,1),'b:')
% hold on
% plot(t,rvec(:,2),'g--')
% hold on
% plot(t,rvec(:,3),'r')
% title(['Position vector versus time over ',num2str(n),' orbital periods'])
% legend('rx','ry','rz')
% xlabel('time (sec)')
% ylabel('position (km)')
% subplot(2,1,2);
% plot(t,vvec(:,1),'b:')
% hold on
% plot(t,vvec(:,2),'g--')
% hold on
% plot(t,vvec(:,3),'r')
% title(['Velocity vector versus time over ',num2str(n),' orbital periods'])
% legend('vx','vy','vz')
% xlabel('time (sec)')
% ylabel('velocity (km/s)')
% print(1, '-depsc', 'randv1')
%
% figure(2)
% plot(rvec(:,1),rvec(:,2))
% axis square
% xlim([-50000 50000])
% ylim([-50000 50000])
% hold on
% ttt=linspace(0,2*pi);
% fill(6378*cos(ttt),6378*sin(ttt),[.5 .8 .3])
% axis square
```

```
% hold on
% plot(rvec(1,1),rvec(1,2),'b-.o','LineWidth',2,'MarkerEdgeColor','r',...
%    'MarkerFaceColor','r','MarkerSize',5)
% text(rvec(1,1),rvec(1,2),'\leftarrowStarting value')
% axis square
% title(['2-D orbit trace of satellite over ',num2str(n),' orbital periods'])
% xlabel('rx (km)')
% ylabel('ry (km)')
% hold off
% print(2, '-depsc', '2-Dtrace1')
%
% figure(3)
% plot3(rvec(:,1),rvec(:,2),rvec(:,3))
% title(['3-D orbit trace of satellite over ',num2str(n),' orbital periods'])
% grid on
% axis tight
% xlim([-40000 40000])
% ylim([-40000 40000])
% zlim([-40000 40000])
% hold on
% colormap winter
% [X,Y,Z] = sphere(20);
% surf(6378*X,6378*Y,6378*Z)
% xlabel('rx (km)')
% ylabel('ry (km)')
% zlabel('rz (km)')
% print(3, '-depsc', '3-Dtrace1')

switch nn
    case 1 % 1 orbit
        meanval = mean(a_vec);
        if meanval>a_vec(1)
            achange = meanval - a_vec(1);
        else
            achange = a_vec(1) - meanval;
        end
        slope = achange/t(length(t));

        figure(4);
        subplot(3,1,1); plot(t,i_vec_deg,'r-')
        title(['\it i \rm versus time over ',num2str(n),...
            ' orbital periods'],'fontsize',12)
        set(gca,'fontsize',12)
        xlabel('time (sec)','fontsize',12)
        ylabel('\it i \rm (deg)','fontsize',12)
        subplot(3,1,2); plot(t,a_vec,'b-')
        set(gca,'fontsize',12)
        title(['\it a \rm versus time over ',num2str(n),...
            ' orbital periods; \Delta\it a \rm=',num2str(achange),' km'],...
            'fontsize',12)
        xlabel('time (sec)','fontsize',12)
```

```
        ylabel('\it a \rm (km)','fontsize',12)
        subplot(3,1,3); plot(t,e_vec,'g-')
        set(gca,'fontsize',12)
        title(['\it e \rm versus time over ',num2str(n),' orbital periods'],...
            'fontsize',12)
        % ylim([0 0.002])
        xlabel('time (sec)','fontsize',12)
        ylabel('\it e','fontsize',12)
end

switch nn
    case {2,3,4}
        figure(4);
        subplot(3,1,1); plot(t,i_vec_deg,'r-')
        title(['\it i \rm versus time over ',num2str(n),...
            ' orbital periods'],'fontsize',12)
        set(gca,'fontsize',12)
        xlabel('time (sec)','fontsize',12)
        ylabel('\it i \rm (deg)','fontsize',12)
        subplot(3,1,2); plot(t,a_vec,'b-')
        set(gca,'fontsize',12)
        title(['\it a \rm versus time over ',num2str(n),...
            ' orbital periods; \Delta\it a \rm=',num2str(a_change),' km'],...
            'fontsize',12)
        xlabel('time (sec)','fontsize',12)
        ylabel('\it a \rm (km)','fontsize',12)
        subplot(3,1,3); plot(t,e_vec,'g-')
        set(gca,'fontsize',12)
        title(['\it e \rm versus time over ',num2str(n),' orbital periods'],...
            'fontsize',12)
        % ylim([0 0.002])
        xlabel('time (sec)','fontsize',12)
        ylabel('\it e','fontsize',12)
end

figure(5);

subplot(3,1,1); plot(t,w_vec_deg,'g-'); title(['\omega versus time
over ',num2str(n),' orbital periods'],'fontsize',12);
set(gca,'fontsize',12); xlabel('time (sec)','fontsize',12);
ylabel('\omega (deg)','fontsize',12)

subplot(3,1,2); plot(t,RAAN_vec,'b-'); title(['\Omega versus time
over ',num2str(n),' orbital periods'],'fontsize',12);
set(gca,'fontsize',12); xlabel('time (sec)','fontsize',12);
ylabel('\Omega (deg)','fontsize',12)

subplot(3,1,3); plot(t,nu_vec,'k-'); title(['\nu versus time over
',num2str(n),' orbital periods'],'fontsize',12);
set(gca,'fontsize',12); xlabel('time (sec)','fontsize',12);
ylabel('\nu (deg)','fontsize',12)
```

```
% This script file is the executable portion of the thesis code.  It calls
% EQUcode.m, and includes switch-case functionality to enable "one-push of
% the button"results.  Recommend running through Linux, as the simulation
% takes approximately 12 hours to push through all data sets.  The
% simulation saves off pertinanent workspace variables and all plots (eps).

% Two-body orbit determination code in modified equinoctial elements
% Capt Jody Paris (GA-O6M)

clc

format long

syms E

a_vec = []; e_vec = []; i_vec = []; w_vec = []; RAAN_vec = [];
nu_vec = []; u_vec = []; rvec = []; vvec = [];

%~~~~~~~~~~~~~~~~~~~~~~~~~~~~~~~~~~~~~~~~~~~~~~~~~~~~~~~~~~~~~~~~~~~~~~~~~~~~~~~
% Define constants and global variables
%~~~~~~~~~~~~~~~~~~~~~~~~~~~~~~~~~~~~~~~~~~~~~~~~~~~~~~~~~~~~~~~~~~~~~~~~~~~~~~~

global n g_s G M_earth R_earth mu_earth mu_moon rho J2 SF c m
epoch_yr...
    epoch_day epoch_frac A_plate A_cyl Earth_aphelion_table c_R_plate...
    c_R_cyl aa s_vec cont moon countt

g_s = 9.796432222e-3;
    % mean gravitational acceleration of Earth at surface (km/s^2)
G = 6.67259e-11;                % universal gravitational constant (Nm^2/kg^2)
M_earth = 5.9737e24;            % Earth's mass (kg)
R_earth = 6378;                 % Earth's radius (km)
mu_earth = 3.986004e5;          % Earth's gravitational parameter (km^3/s^2)
beta = 0.14;                    % km^-1
rho_s = 1.225e9;                % density at surface of Earth, kg/km^3
J2 = 0.0010826269;              % Earth's oblateness coefficient
SF = 1353;                      % solar flux value (kg/sec^2)
c = 299792458/1000;             % speed of light (km/sec)
m_moon = 7.3483e22;             % mass of moon (kg)
mu_moon = 4902.799;             % gravitational parameter of moon (km^3/s^2)
Earth_aphelion_table = [2005 186;2006 184;2007 188;2008 186;2009
185;...
    2010 187;2011 185;2012 187;2013 186;2014 185;2015 187;2016 186;...
    2017 184;2018 187;2019 185;2020 186];
    % in [year date] format, from US Naval Observatory

m = 611;                        % satellite mass, kg
l = .004;                       % satellite length (rotating platform), km
d = .003;                       % satellite diameter, km
A_plate = .00000335;            % area of flat plate (parabolic antennae), km^2
```

```
A_cyl = .00000502;              % area of spinning body (cylindrical), km^2
c_R_cyl = [1/3; 1/3; 1/3];
    % reflectivity coefficients [absorption; diffuse; specular] for
    % cylinder

%~~~~~~~~~~~~~~~~~~~~~~~~~~~~~~~~~~~~~~~~~~~~~~~~~~~~~~~~~~~~~~~~~~~~~~~~~~~~~~~
% run baseline case (no controller, despun area = 0)
%~~~~~~~~~~~~~~~~~~~~~~~~~~~~~~~~~~~~~~~~~~~~~~~~~~~~~~~~~~~~~~~~~~~~~~~~~~~~~~~
cont = 1; controller = 'b';
c_R_plate = [1/3; 1/3; 1/3];
    % reflectivity coefficients [absorption; diffuse; specular]
for nn=1:3
    switch nn
        case 1
            n = 1;  % number of orbits to propagate over
            MaxStep = 1e2;
        case 2
            n = 100;  % number of orbits to propagate over
            MaxStep = 1e3;
        case 3
            n = 1000;  % number of orbits to propagate over
            MaxStep = 1e4;
        case 4
            n = 10000;
            MaxStep = 1e5;
    end
    multfactor = 1;
    filename = ['b_' num2str(n)];

    EQUcode     % call EQUcode.m

    % help save
    filenamet = [filename 't'];
    filenamei = [filename 'i'];
    filenamea = [filename 'a'];
    filenamee = [filename 'e'];
%     filenamew = [filename 'w'];           % uncomment to save
%     filenameRAAN = [filename 'RAAN'];     % uncomment to save
%     filenamenu = [filename 'nu'];         % uncomment to save
%
    save(filenamet,'t')
    save(filenamei,'i_vec_deg')
    save(filenamea,'a_vec')
    save(filenamee,'e_vec')
%     save(filenamew,'w_vec_deg')           % uncomment to save
%     save(filenameRAAN,'RAAN_vec')         % uncomment to save
%     save(filenamenu,'nu_vec')             % uncomment to save
%     save('poft1000','poft')               % uncomment to save
%     save('goft1000','goft')               % uncomment to save
%     save('foft1000','foft')               % uncomment to save
%     save('Loft1000','Loft')               % uncomment to save
```

```
%     save('koft1000','koft')              % uncomment to save
%     save('hoft1000','hoft')              % uncomment to save

    % help print
    filenamef4 = [filename 'iae'];
    filenamef5 = [filename 'wRAANnu'];
    print(4, '-depsc', filenamef4)         % prints figure 4 to .eps file
    print(5, '-depsc', filenamef5)         % prints figure 5 to .eps file

    close all;
    clear filename
    a_vec = []; e_vec = []; i_vec = []; w_vec = [];...
        RAAN_vec = []; nu_vec = []; u_vec = []; rvec = [];...
        vvec = [];

end

%~~~~~~~~~~~~~~~~~~~~~~~~~~~~~~~~~~~~~~~~~~~~~~~~~~~~~~~~~~~~~~~~~~~~~~~~~~~~~~~
% run other cases
%~~~~~~~~~~~~~~~~~~~~~~~~~~~~~~~~~~~~~~~~~~~~~~~~~~~~~~~~~~~~~~~~~~~~~~~~~~~~~~~
for cont=2:3   % contoller is indexed in srpaccel.m
    switch cont
        case 1
            controller = 'b';  % baseline case
        case 2
            controller = 's';  % simple controller
            cc = 'simple';
        case 3
            controller = 'c';  % complex controller
            cc = 'complex';
    end
    for CRP=1:5
        switch CRP
            case 1
                c_R_plate = [1/3; 1/3; 1/3];
                % reflectivity coefficients
                % [absorption; diffuse; specular] for antennae
                coeff = [controller '_thirds'];
            case 2
                c_R_plate = [1; 0; 0];  % all absorption
                coeff = [controller '_a'];
            case 3
                c_R_plate = [0; 0; 1];  % all specular reflection
                coeff = [controller '_s'];
            case 4
                c_R_plate = [0; 1; 0];  % all diffuse reflection
                coeff = [controller '_d'];
            case 5
                c_R_plate = [0; .5; .5];  % specular & diffuse reflection
                coeff = [controller '_sd'];
        end
```

```
for nn=1:3
    %~~~~~~~~~~~~~~~~~~~~~~~~~~~~~~~~~~~~~~~~~~~~~~~~~~~~~~~~~~~~~~~~~~~~
    % Define varying parameters for code
    %~~~~~~~~~~~~~~~~~~~~~~~~~~~~~~~~~~~~~~~~~~~~~~~~~~~~~~~~~~~~~~~~~~~~
    switch nn
        case 1
            n = 1;  % number of orbits to propagate over
            MaxStep = 1e2;
            orbitt = [coeff '_1'];
        case 2
            n = 100;  % number of orbits to propagate over
            MaxStep = 1e3;
            orbitt = [coeff '_100'];
        case 3
            n = 1000;  % number of orbits to propagate over
            MaxStep = 1e4;
            orbitt = [coeff '_1000'];
    end
    for mf=1:3
        switch mf
            case 1
                multfactor = 1;
                A_plate = .00000335*multfactor;
                filename = [orbitt '_1'];
            case 2
                multfactor = 5;
                A_plate = .00000335*multfactor;
                filename = [orbitt '_5'];
            case 3
                multfactor = 10;
                A_plate = .00000335*multfactor;
                filename = [orbitt '_10'];
        end

        EQUcode

        % help save
        filenamet = [filename 't'];
        filenamei = [filename 'i'];
        filenamea = [filename 'a'];
        filenamee = [filename 'e'];
        filenamew = [filename 'w'];
        filenameRAAN = [filename 'RAAN'];
        filenamenu = [filename 'nu'];

        save(filenamet,'t')
        save(filenamei,'i_vec_deg')
        save(filenamea,'a_vec')
        save(filenamee,'e_vec')
        save(filenamew,'w_vec_deg')
        save(filenameRAAN,'RAAN_vec')
```

```
            save(filenamenu,'nu_vec')

            % help print
            filenamef4 = [filename 'iae'];
            filenamef5 = [filename 'wRAANnu'];
            print(4, '-depsc', filenamef4)
            print(5, '-depsc', filenamef5)


            if cont~=1
                bt = ['b_' num2str(n) 't'];
                tb=load(bt);
                    % baseline time vector for current case
                ba = ['b_' num2str(n) 'a'];
                ab=load(ba);
                    % baseline semimajor axis vector for current case

                x = polyfit(t',a_vec,1);
                polx = x(1)*t+x(2);
                a_change = polx(length(polx))-polx(1);

                figure(6)
                plot(tb.t,ab.a_vec,'b--')
                title(['\it a \rm versus time over ',num2str(n),...
                    ' orbital periods; \Delta\it a \rm=',...
                    num2str(a_change),' km'],'fontsize',12)
                set(gca,'fontsize',12)
                xlabel('time (sec)','fontsize',12)
                ylabel('\it a \rm (km)','fontsize',12)
                hold on
                plot(t,a_vec,'r')
                legend('baseline',num2str(cc),'Location','Best')
                hold off

                filenamef6 = ['mix_' filename];
                print(6, '-depsc', filenamef6)

            end

            close all

            clear filename
            a_vec = []; e_vec = []; i_vec = []; w_vec = [];...
                RAAN_vec = []; nu_vec = []; u_vec = []; rvec = [];...
                vvec = [];

        end

    end

end
```

```
end
```

C.6 juldate.m

```
function JD = juldate(epoch_yr,epoch_day,epoch_frac)
% This function inputs the epoch information given in the current TLE set
% and outputs the appropriate Julian day based on the algorithm given on
% page 186 of Vallado.  Here, JD is based on UTC but can be set equal to JD_UT1.

% calculate the following based on epoch_frac and epoch_day:
if epoch_yr/4 == fix(epoch_yr/4)
    if epoch_yr/100 == fix(epoch_yr/100)
        if epoch_yr/400 == fix(epoch_yr/400)
            j = 1;  % leap year
        else
            j = 0;  % not a leap year
        end
    else
        j = 1;
    end
else
        j = 0;
end

if epoch_day <= 31
        epoch_mo = 1;
        epoch_dofm = epoch_day;
elseif epoch_day <= 59+j
        epoch_mo = 2;
        epoch_dofm = epoch_day - 31+j;
elseif epoch_day <= 90+j
        epoch_mo = 3;
        epoch_dofm = epoch_day - 59+j;
elseif epoch_day <= 120+j
        epoch_mo = 4;
        epoch_dofm = epoch_day - 90+j;
elseif epoch_day <= 151+j
        epoch_mo = 5;
        epoch_dofm = epoch_day - 120+j;
elseif epoch_day <= 181+j
        epoch_mo = 6;
        epoch_dofm = epoch_day - 151+j;
elseif epoch_day <= 212+j
        epoch_mo = 7;
        epoch_dofm = epoch_day - 181+j;
elseif epoch_day <= 243+j
        epoch_mo = 8;
        epoch_dofm = epoch_day - 212+j;
elseif epoch_day <= 273+j
        epoch_mo = 9;
```

```
        epoch_dofm = epoch_day - 243+j;
elseif epoch_day <= 304+j
        epoch_mo = 10;
        epoch_dofm = epoch_day - 273+j;
elseif epoch_day <= 334+j
        epoch_mo = 11;
        epoch_dofm = epoch_day - 304+j;
else
        epoch_mo = 12;
        epoch_dofm = epoch_day - 334+j;
end

epoch_hrlong = epoch_frac*24; % chop off remainder and use for min
    epoch_hr = fix(epoch_hrlong);
epoch_minlong = (epoch_hrlong - epoch_hr)*60;
    % chop off remainder and use for sec
    epoch_min = fix(epoch_minlong);
epoch_sec = (epoch_minlong - epoch_min)*60;

JD = 367*epoch_yr-real((7*epoch_yr+real((epoch_mo+9)/12))/4)+...
    real(275*epoch_mo/9)+epoch_dofm+1721013.5+((((epoch_sec/60)+...
    epoch_min)/60)+epoch_hr)/24;

return
```

C.7 juldatet.m

```
function JD = juldatet(t)
% This function inputs the epoch information given in the current TLE set
% and outputs the appropriate Julian day based on the algorithm given on
% page 186 of Vallado.  Here, JD is based on UTC but can be set equal to JD_UT1.


epoch_yr_o = 2005; % year in 4-digit format
epoch_day_o = 202; epoch_frac_o = .40912884;

current_epoch_yrlong = t*3.1688764640818e-8; % convert t in sec to years
current_epoch_yr = fix(current_epoch_yrlong);
    current_remainder_yr = current_epoch_yrlong - fix(current_epoch_yrlong);
current_epoch_daylong = current_remainder_yr*365.2442;
    % remainder of years to days
current_epoch_day = fix(current_epoch_daylong);
    current_epoch_frac = current_epoch_daylong - fix(current_epoch_daylong);
        % fraction of a day leftover

epoch_yr = epoch_yr_o + current_epoch_yr; epoch_day = epoch_day_o
+ current_epoch_day; epoch_frac = epoch_frac_o +
current_epoch_frac;

% calculate the following based on epoch_frac and epoch_day:
if epoch_yr/4 == fix(epoch_yr/4)
```

```
    if epoch_yr/100 == fix(epoch_yr/100)
        if epoch_yr/400 == fix(epoch_yr/400)
            j = 1;  % leap year
        else
            j = 0;  % not a leap year
        end
    else
        j = 1;
    end
else
        j = 0;
end

if epoch_day <= 31
        epoch_mo = 1;
        epoch_dofm = epoch_day;
elseif epoch_day <= 59+j
        epoch_mo = 2;
        epoch_dofm = epoch_day - 31+j;
elseif epoch_day <= 90+j
        epoch_mo = 3;
        epoch_dofm = epoch_day - 59+j;
elseif epoch_day <= 120+j
        epoch_mo = 4;
        epoch_dofm = epoch_day - 90+j;
elseif epoch_day <= 151+j
        epoch_mo = 5;
        epoch_dofm = epoch_day - 120+j;
elseif epoch_day <= 181+j
        epoch_mo = 6;
        epoch_dofm = epoch_day - 151+j;
elseif epoch_day <= 212+j
        epoch_mo = 7;
        epoch_dofm = epoch_day - 181+j;
elseif epoch_day <= 243+j
        epoch_mo = 8;
        epoch_dofm = epoch_day - 212+j;
elseif epoch_day <= 273+j
        epoch_mo = 9;
        epoch_dofm = epoch_day - 243+j;
elseif epoch_day <= 304+j
        epoch_mo = 10;
        epoch_dofm = epoch_day - 273+j;
elseif epoch_day <= 334+j
        epoch_mo = 11;
        epoch_dofm = epoch_day - 304+j;
else
        epoch_mo = 12;
        epoch_dofm = epoch_day - 334+j;
end
```

```
epoch_hrlong = epoch_frac*24; % chop off remainder and use for min
    epoch_hr = fix(epoch_hrlong);
epoch_minlong = (epoch_hrlong - epoch_hr)*60;
    % chop off remainder and use for sec
    epoch_min = fix(epoch_minlong);
epoch_sec = (epoch_minlong - epoch_min)*60;

JD = 367*epoch_yr-real((7*epoch_yr+real((epoch_mo+9)/12))/4)+...
    real(275*epoch_mo/9)+epoch_dofm+1721013.5+((((epoch_sec/60)+...
    epoch_min)/60)+epoch_hr)/24;

return
```

C.8 mequtorv.m

```
function x_o_vec = mequtorv(p_o, f_o, g_o, h_o, k_o, L_o)
% This function inputs the initial modified equinoctial element set (p, f,
% g, h, k, & L) and outputs the initial state vector x_o (composed of the r
% and v vectors) based on the inital element set.

global g_s G M_earth R_earth mu_earth

alpha = sqrt(h_o^2 - k_o^2); s = sqrt(1 + h_o^2 + k_o^2); w = 1 +
f_o*cos(L_o) + g_o*sin(L_o); r = p_o/w;

xo = (r/s^2)*(cos(L_o) + alpha^2*cos(L_o) + 2*h_o*k_o*sin(L_o));
yo = (r/s^2)*(sin(L_o) - alpha^2*sin(L_o) + 2*h_o*k_o*cos(L_o));
zo = (2*r/s^2)*(h_o*sin(L_o) - k_o*cos(L_o));

xdoto = (-1/s^2)*sqrt(mu_earth/p_o)*(sin(L_o) +
alpha^2*sin(L_o)...
    - 2*h_o*k_o*cos(L_o) + g_o - 2*f_o*h_o*k_o + alpha^2*g_o);
ydoto = (-1/s^2)*sqrt(mu_earth/p_o)*(-cos(L_o) +
alpha^2*cos(L_o)...
    + 2*h_o*k_o*sin(L_o) - f_o + 2*g_o*h_o*k_o + alpha^2*f_o);
zdoto = (2/s^2)*sqrt(mu_earth/p_o)*(h_o*cos(L_o) + k_o*sin(L_o)...
    + f_o*h_o + g_o*k_o);

x_o_vec = [xo; yo; zo; xdoto; ydoto; zdoto];

return
```

C.9 oblateearth.m

```
function J2term = oblateearth(t,x)

global SF c g_s G M_earth R_earth mu_earth m epoch_yr A_plate
A_cyl...
    Earth_aphelion_table c_R_plate c_R_cyl J2

e_earth = sqrt(0.006694385);
```

```
p = x(1); f = x(2); g = x(3); h = x(4); k = x(5); L = x(6);

%~~~~~~~~~~~~~~~~~~~~~~~~~~~~~~~~~~~~~~~~~~~~~~~~~~~~~~~~~~~~~~~~~~~~~~~~~~~~
% compute r vector from EQU set
%~~~~~~~~~~~~~~~~~~~~~~~~~~~~~~~~~~~~~~~~~~~~~~~~~~~~~~~~~~~~~~~~~~~~~~~~~~~~
alpha = sqrt(h^2 - k^2); s = sqrt(1 + h^2 + k^2); w = 1 + f*cos(L)
+ g*sin(L); r = p/w; ri = (r/s^2)*(cos(L) + alpha^2*cos(L) +
2*h*k*sin(L)); rj = (r/s^2)*(sin(L) - alpha^2*sin(L) +
2*h*k*cos(L)); rk = (2*r/s^2)*(h*sin(L) - k*cos(L)); r_vec = [ri;
rj; rk];

xdot = (-1/s^2)*sqrt(mu_earth/p)*(sin(L) + alpha^2*sin(L)...
    - 2*h*k*cos(L) + g - 2*f*h*k + alpha^2*g);
ydot = (-1/s^2)*sqrt(mu_earth/p)*(-cos(L) + alpha^2*cos(L)...
    + 2*h*k*sin(L) - f + 2*g*h*k + alpha^2*f);
zdot = (2/s^2)*sqrt(mu_earth/p)*(h*cos(L) + k*sin(L) + f*h + g*k);
v_vec = [xdot; ydot; zdot];

ir = r_vec/norm(r_vec); in =
cross(r_vec,v_vec)/norm(cross(r_vec,v_vec)); it = cross(in,ir);
R = [ir it in];   % Rotation matrix from ECI frame to RTN frame

a = R_earth;

%~~~~~~~~~~~~~~~~~~~~~~~~~~~~~~~~~~~~~~~~~~~~~~~~~~~~~~~~~~~~~~~~~~~~~~~~~~~~
% find the geocentric latitude (Vallado pg 146)
%~~~~~~~~~~~~~~~~~~~~~~~~~~~~~~~~~~~~~~~~~~~~~~~~~~~~~~~~~~~~~~~~~~~~~~~~~~~~
phi_gc = atan2(rk,sqrt(ri^2 + rj^2));    % rad, pg 145 instead

%~~~~~~~~~~~~~~~~~~~~~~~~~~~~~~~~~~~~~~~~~~~~~~~~~~~~~~~~~~~~~~~~~~~~~~~~~~~~
% define the Legendre polynomials (Vallado pg 517)
%~~~~~~~~~~~~~~~~~~~~~~~~~~~~~~~~~~~~~~~~~~~~~~~~~~~~~~~~~~~~~~~~~~~~~~~~~~~~
P2 = (1/2)*(3*(sin(phi_gc))^2 - 1); % P_2,0
P2prime = 3*sin(phi_gc);
    % Dr. Wiesel's solution, interpreted from Betts

%~~~~~~~~~~~~~~~~~~~~~~~~~~~~~~~~~~~~~~~~~~~~~~~~~~~~~~~~~~~~~~~~~~~~~~~~~~~~
% find the perturbing acceleration
%~~~~~~~~~~~~~~~~~~~~~~~~~~~~~~~~~~~~~~~~~~~~~~~~~~~~~~~~~~~~~~~~~~~~~~~~~~~~
delta_gr = (-mu_earth/r^2)*(3*(a/r)^2*P2*J2); delta_gn =
(-mu_earth*cos(phi_gc)/r^2)*((a/r)^2*P2prime*J2);

en_vec = [0 0 1]'; inorth =
(en_vec-(en_vec'*ir)*ir)/norm(en_vec-(en_vec'*ir)*ir);
    % describes the local North direction

delta_g = delta_gn*inorth - delta_gr*ir;
    % gravitational disturbing acceleration

J2term = R'*delta_g;
```

```
return
```

C.10 propxequ.m

```
function xdot = propxequ(t,x)
% This function inputs the initial state vector x_o_vec (composed of r_o
% and v_o vectors) and outputs the state vector x_vec (composed of r and v
% vectors) based on those parameters and applicable perturbations.

global n g_s G M_earth R_earth mu_earth rho J2 SF c m epoch_yr
epoch_day...
    epoch_frac aa countt

% track progress:
countt=countt+1; orbitno = t/9.037752480834280e+004; if orbitno >=
aa
    aa; % uncomment to track compile progress
    aa = aa+1;
end

p = x(1); f = x(2); g = x(3); h = x(4); k = x(5); L = x(6);

%~~~~~~~~~~~~~~~~~~~~~~~~~~~~~~~~~~~~~~~~~~~~~~~~~~~~~~~~~~~~~~~~~~~~~~~~~~~~
% calculate current r_vec, v_vec and R
%~~~~~~~~~~~~~~~~~~~~~~~~~~~~~~~~~~~~~~~~~~~~~~~~~~~~~~~~~~~~~~~~~~~~~~~~~~~~
alpha_squared = h^2 - k^2; w = 1 + f*cos(L) + g*sin(L); r = p/w;
Chi = sqrt(h^2 + k^2); s_squared = 1 + Chi^2;

ri = (r/s_squared)*(cos(L) + alpha_squared*cos(L) + 2*h*k*sin(L));
rj = (r/s_squared)*(sin(L) - alpha_squared*sin(L) + 2*h*k*cos(L));
rk = (2*r/s_squared)*(h*sin(L) - k*cos(L));
r_vec = [ri; rj; rk];   % ECI position vector of the satellite (km)
xdot = (-1/s_squared)*sqrt(mu_earth/p)*(sin(L) +
alpha_squared*sin(L)...
    - 2*h*k*cos(L) + g - 2*f*h*k + alpha_squared*g);
ydot = (-1/s_squared)*sqrt(mu_earth/p)*(-cos(L) +
alpha_squared*cos(L)...
    + 2*h*k*sin(L) - f + 2*g*h*k + alpha_squared*f);
zdot = (2/s_squared)*sqrt(mu_earth/p)*(h*cos(L) + k*sin(L) + f*h +
g*k);
v_vec = [xdot; ydot; zdot]; % ECI velocity vector
x_vec = [r_vec; v_vec];

ir = r_vec/norm(r_vec); in =
cross(r_vec,v_vec)/norm(cross(r_vec,v_vec)); it = cross(in,ir);
R = [ir it in];   % Rotation matrix from ECI frame to RTN frame

%~~~~~~~~~~~~~~~~~~~~~~~~~~~~~~~~~~~~~~~~~~~~~~~~~~~~~~~~~~~~~~~~~~~~~~~~~~~~
% calculate current Julian date & Earth-Sun vector
%~~~~~~~~~~~~~~~~~~~~~~~~~~~~~~~~~~~~~~~~~~~~~~~~~~~~~~~~~~~~~~~~~~~~~~~~~~~~
```

```
JD = juldatet(t);     % JD is in ref to UTC (let JD_UTC = JD_UT1)

r_ES_vec = earthsunt(t);    % ECI position vector of the Sun (km)

%~~~~~~~~~~~~~~~~~~~~~~~~~~~~~~~~~~~~~~~~~~~~~~~~~~~~~~~~~~~~~~~~~~~~~~~~~~~~~~~
% calculate matrix form A & b (3 Nov 05 changes)
%~~~~~~~~~~~~~~~~~~~~~~~~~~~~~~~~~~~~~~~~~~~~~~~~~~~~~~~~~~~~~~~~~~~~~~~~~~~~~~~
A = [0 (2*p/w)*sqrt(p/mu_earth) 0;...
    sqrt(p/mu_earth)*sin(L) sqrt(p/mu_earth)*(1/w)*((w+1)*cos(L)+f) -...
    sqrt(p/mu_earth)*(g/w)*(h*sin(L)-k*cos(L));...
    -sqrt(p/mu_earth)*cos(L) sqrt(p/mu_earth)*(1/w)*((w+1)*sin(L)+g)...
    sqrt(p/mu_earth)*(f/w)*(h*sin(L)-k*cos(L));...
    0 0 sqrt(p/mu_earth)*(s_squared*cos(L)/(2*w));...
    0 0 sqrt(p/mu_earth)*(s_squared*sin(L)/(2*w));...
    0 0 sqrt(p/mu_earth)*(1/w)*(h*sin(L)-k*cos(L))];

b = [0; 0; 0; 0; 0; sqrt(mu_earth*p)*(w/p)^2];

%~~~~~~~~~~~~~~~~~~~~~~~~~~~~~~~~~~~~~~~~~~~~~~~~~~~~~~~~~~~~~~~~~~~~~~~~~~~~~~~
% J2 effects
%~~~~~~~~~~~~~~~~~~~~~~~~~~~~~~~~~~~~~~~~~~~~~~~~~~~~~~~~~~~~~~~~~~~~~~~~~~~~~~~
J2term = oblateearth(t,x);  % same results as Vallado!
J2_r = J2term(1,:);   % radial component of SRP perturbing acceleration vector
J2_t = J2term(2,:);   % tangential component of SRP perturbing acceleration vector
J2_n = J2term(3,:);   % normal component of SRP perturbing acceleration vector

%~~~~~~~~~~~~~~~~~~~~~~~~~~~~~~~~~~~~~~~~~~~~~~~~~~~~~~~~~~~~~~~~~~~~~~~~~~~~~~~
% Solar third-body effects
%~~~~~~~~~~~~~~~~~~~~~~~~~~~~~~~~~~~~~~~~~~~~~~~~~~~~~~~~~~~~~~~~~~~~~~~~~~~~~~~
mu_sun = 1.32712428e11;            % km^3/s^2
da = -(mu_sun/norm(r_ES_vec)^3)*(r_vec - ...
    3*r_ES_vec*(dot(r_vec,r_ES_vec)/norm(r_ES_vec)^2) - ...
    15*r_ES_vec*(dot(r_vec,r_ES_vec)/norm(r_ES_vec)^2)^2);
a_sun = R'*da; sun_r = a_sun(1,:); sun_t = a_sun(2,:); sun_n =
a_sun(3,:);

%~~~~~~~~~~~~~~~~~~~~~~~~~~~~~~~~~~~~~~~~~~~~~~~~~~~~~~~~~~~~~~~~~~~~~~~~~~~~~~~
% find the number of Julian centuries
%~~~~~~~~~~~~~~~~~~~~~~~~~~~~~~~~~~~~~~~~~~~~~~~~~~~~~~~~~~~~~~~~~~~~~~~~~~~~~~~
T_TDB = (JD - 2451545.0)/36525;     % Vallado pg 188

%~~~~~~~~~~~~~~~~~~~~~~~~~~~~~~~~~~~~~~~~~~~~~~~~~~~~~~~~~~~~~~~~~~~~~~~~~~~~~~~
% SRP effects (only in sat-sun radial direction according to Vallado)
%~~~~~~~~~~~~~~~~~~~~~~~~~~~~~~~~~~~~~~~~~~~~~~~~~~~~~~~~~~~~~~~~~~~~~~~~~~~~~~~
% implement shadow algorithm (page 297 of Vallado)
tau_min = (norm(r_vec)^2-dot(r_vec,r_ES_vec))/...
    (norm(r_vec)^2+norm(r_ES_vec)^2-2*dot(r_vec,r_ES_vec));
        % make sure vectors have same units!
min_val2 = ((1-tau_min)*norm(r_vec)^2 + r_vec'*r_ES_vec*tau_min)/6378^2;
    % must be in ER^2!
if ((tau_min < 0.0) | (tau_min > 1))
```

```
    % satellite is illuminated; run SRP algorithm
    SRP = srpaccel(JD,x_vec,R,r_ES_vec);
    SRP_r = SRP(1,:);
        % radial component of SRP perturbing acceleration vector
    SRP_t = SRP(2,:);
        % tangential component of SRP perturbing acceleration vector
    SRP_n = SRP(3,:);
        % normal component of SRP perturbing acceleration vector
    shadow = 1;
elseif min_val2 >= 1.0
    % satellite is illuminated; run SRP algorithm
    SRP = srpaccel(JD,x_vec,R,r_ES_vec);
    SRP_r = SRP(1,:);
        % radial component of SRP perturbing acceleration vector
    SRP_t = SRP(2,:);
        % tangential component of SRP perturbing acceleration vector
    SRP_n = SRP(3,:);
        % normal component of SRP perturbing acceleration vector
    shadow = 1;
else
    % satellite is NOT illuminated; skip SRP algorithm since not affected
    SRP_r = 0;
        % radial component of SRP perturbing acceleration vector
    SRP_t = 0;
        % tangential component of SRP perturbing acceleration vector
    SRP_n = 0;
        % normal component of SRP perturbing acceleration vector
    shadow = 0;
end

%~~~~~~~~~~~~~~~~~~~~~~~~~~~~~~~~~~~~~~~~~~~~~~~~~~~~~~~~~~~~~~~~~~~~~~~~~~~~~~
% formulate perturbation acceleration vector (RTN frame)
%~~~~~~~~~~~~~~~~~~~~~~~~~~~~~~~~~~~~~~~~~~~~~~~~~~~~~~~~~~~~~~~~~~~~~~~~~~~~~~
Pr = J2_r + SRP_r + sun_r; Pt = J2_t + SRP_t + sun_t; Pn = J2_n +
SRP_n + sun_n;

P = [Pr; Pt; Pn];

%~~~~~~~~~~~~~~~~~~~~~~~~~~~~~~~~~~~~~~~~~~~~~~~~~~~~~~~~~~~~~~~~~~~~~~~~~~~~~~
% state equation solution
%~~~~~~~~~~~~~~~~~~~~~~~~~~~~~~~~~~~~~~~~~~~~~~~~~~~~~~~~~~~~~~~~~~~~~~~~~~~~~~
xdot = A*P + b;

return;
```

C.11 srpaccel.m

```
function SRP = srpaccel(JD,x_vec,R,r_ES_vec)
% This function inputs the iteration time step and state vector and outputs
% the total disturbing acceleration caused by SRP forces.
global SF c g_s G M_earth R_earth mu_earth m epoch_yr A_plate
```

```
A_cyl...
    Earth_aphelion_table c_R_plate c_R_cyl cont

p_SR_simple = SF/c; % simple approximation (W/km^2)/(km/sec)=W*km/sec
row = epoch_yr-2004; D_aph = Earth_aphelion_table(row,2);
p_SR_complex = (1358/(1.004+0.0334*cos(D_aph))*(1/c));
    % more complex approximation (page 547)
C_Rb = 2; % coefficient of reflectivity of s/c body (dimensionless)
    % 2 indicates flat mirror perp to sun
    % 1 indicates a black body surface
C_Rp = 2;
    % coefficient of reflectivity of parabolic reflectors (dimensionless)

r_vec = [x_vec(1); x_vec(2); x_vec(3)];
    % this is the Earth-Satellite vector
v_vec = [x_vec(4); x_vec(5); x_vec(6)];
r_satsun = -r_vec + r_ES_vec; % -r_earthsat + r_earthsun

switch cont
    case 1 % controller 1

        %~~~~~~~~~~~~~~~~~~~~~~~~~~~~~~~~~~~~~~~~~~~~~~~~~~~~~~~~~~~~~~~~~~~~
        % Baseline case (no controller, area of despun platform = zero)
        %~~~~~~~~~~~~~~~~~~~~~~~~~~~~~~~~~~~~~~~~~~~~~~~~~~~~~~~~~~~~~~~~~~~~
        p_SR_simple = SF/c;
            % simple approximation (W/km^2)/(km/sec)=W*km/sec
        row = epoch_yr-2004;
        D_aph = Earth_aphelion_table(row,2);
        p_SR_complex = (1358/(1.004+0.0334*cos(D_aph))*(1/c));
            % more complex approximation (page 547)
        C_Rb = 1.5;
            % coefficient of reflectivity of s/c body (dimensionless)
            % 2 indicates flat mirror perp to sun
            % 1 indicates a black body surface

        ir = r_vec/norm(r_vec);
        in = cross(r_vec,v_vec)/norm(cross(r_vec,v_vec));
        it = cross(in,ir);
        R = [ir'; it'; in'];
            % Rotation matrix from ECI frame to RTN frame

        r_satsun = -r_vec + r_ES_vec; % -r_earthsat + r_earthsun
        s_vec = r_satsun/norm(r_satsun); % sat-sun UNIT vector

        % for the rotating cylinder:
        phi_cyl = 0;
            % reflected or incident angle of the cylinder
            % (always perpendicular to s_vec since a cylinder)
        n_vec_c = s_vec;
            % again, face of cylinder always perpendicular to s_vec
        n_vec_cyl = n_vec_c/norm(n_vec_c);  % UNIT vector
```

```
    % for the despun platform:
    A_expp = 0;
    phi_plate = 0;
    n_vec_plate = n_vec_cyl;

    % note: reflectivity coefficients [absorption; diffuse; specular]
    a_SRP_plate = (p_SR_complex*A_expp*cos(phi_plate)/m)*...
        (2*((c_R_plate(2)/3) + c_R_plate(3)*cos(phi_plate))*...
        n_vec_plate + (1-c_R_plate(3))*s_vec);
    a_SRP_cyl = (p_SR_complex*A_cyl*cos(phi_cyl)/m)*...
        (2*((c_R_cyl(2)/3) + c_R_cyl(3)*cos(phi_cyl))*n_vec_cyl +...
        (1-c_R_cyl(3))*s_vec);
    a_SRP = -a_SRP_plate - a_SRP_cyl;

    SRP = R*a_SRP;  % SRP acceleration vector in RTN frame
    %~~~~~~~~~~~~~~~~~~~~~~~~~~~~~~~~~~~~~~~~~~~~~~~~~~~~~~~~~~~~~~~~~~~~~~~~

case 2 % controller 2
    %~~~~~~~~~~~~~~~~~~~~~~~~~~~~~~~~~~~~~~~~~~~~~~~~~~~~~~~~~~~~~~~~~~~~~~~~
    % Vallado (page 549)
    %~~~~~~~~~~~~~~~~~~~~~~~~~~~~~~~~~~~~~~~~~~~~~~~~~~~~~~~~~~~~~~~~~~~~~~~~
    s_vec = r_satsun/norm(r_satsun);   % sat-sun UNIT vector
    norm(s_vec);
    costheta = dot(r_satsun,v_vec)./(norm(r_satsun)*norm(v_vec));

    % simple on/off control algorithm
    if costheta <= 0  % full plate area toward sun
        gamma = acos(dot(r_vec,s_vec)/norm(r_vec));   % radians
        A_expp = A_plate; % km^2, flat plate approximation 3m x 1.1176m
    else % no plate area toward sun
        gamma = acos(dot(r_vec,s_vec)/norm(r_vec)) - pi/2;  % radians
        A_expp = 0; % km^2, flat plate approximation
    end

    theta_vallado = acos(dot(r_vec,v_vec)/(norm(r_vec)*norm(v_vec)));
        % radians

    % for the antennae:
    phi_plate = acos(dot(r_vec,s_vec)/norm(r_vec))-gamma;
        % reflected or incident angle of the antennae

    %~~~~~~~~~~~~~~~~~~~~~~~~~~~~~~~~~~~~~~~~~~~~~~~~~~~~~~~~~~~~~~~~~~~~~~~~
    % calculate normal vector, n_vec (based on commanded angle)
    %~~~~~~~~~~~~~~~~~~~~~~~~~~~~~~~~~~~~~~~~~~~~~~~~~~~~~~~~~~~~~~~~~~~~~~~~
    % calculate n_vec (rotate from r_vec to n_vec through gamma):
    R_gamma = [cos(gamma) sin(gamma) 0;-sin(gamma) cos(gamma) 0; 0 0 1];
    n_vec_p = R'*R_gamma*R*r_vec;

    n_vec_plate = n_vec_p/norm(n_vec_p);
        % UNIT vector perpendicular to plate surface, directed opposite
```

```
        % of normal force (thus towards Sun)
    %~~~~~~~~~~~~~~~~~~~~~~~~~~~~~~~~~~~~~~~~~~~~~~~~~~~~~~~~~~~~~~~~~~~~~~~

case 3 % controller 3

    %~~~~~~~~~~~~~~~~~~~~~~~~~~~~~~~~~~~~~~~~~~~~~~~~~~~~~~~~~~~~~~~~~~~~~~~
    % Coverstone model for control algorithm (modified)
    %~~~~~~~~~~~~~~~~~~~~~~~~~~~~~~~~~~~~~~~~~~~~~~~~~~~~~~~~~~~~~~~~~~~~~~~
    s_vec = r_satsun/norm(r_satsun);
        % sat-sun UNIT vector (km) in ECI frame

    % 1. calculate the number of Julian centuries
    T_UT1 = (JD - 2451545.0)/36525; % Vallado pg 188
    lambda_M_sundeg = 280.460 + 36000.770*T_UT1;
        % mean ecliptic longitude of the Sun (deg), Vallado pg 265
    T_TDB = T_UT1;
    M_sundeg = 357.5277233 + 35999.05034*T_TDB;
        % Sun's mean anomaly (deg)
    lambda_ecliptic = lambda_M_sundeg + 1.914666471*sind(M_sundeg) +...
        0.019994643*sind(2*M_sundeg);
        % ecliptic longitude of the Sun (deg)

    % 2. rotate v_vec from ECI to heliocentric XYZ frame:
    R_XYZfromECI = [1 0 0;0 cosd(23.5) sind(23.5);...
        0 -sind(23.5) cosd(23.5)];
    v_vec_XYZ = R_XYZfromECI*v_vec;

    % 3. rotate v_vec_XYZ to alpha-beta-z (ABC) frame:
    R_ABZfromXYZ = [cosd(lambda_ecliptic) sind(lambda_ecliptic) 0;
        -sind(lambda_ecliptic) cosd(lambda_ecliptic) 0; 0 0 1];
    v_vec_ABZ = R_ABZfromXYZ*v_vec_XYZ;

    % 4. calculate the desired normal vector, n_vec_ABZ:
    zeta = (-3*v_vec_ABZ(1)*v_vec_ABZ(2) - v_vec_ABZ(2)*...
        sqrt(9*v_vec_ABZ(1)^2 + 8*(v_vec_ABZ(2)^2 +...
        v_vec_ABZ(3)^2)))/(4*(v_vec_ABZ(2)^2 + v_vec_ABZ(3)^2));
    n_alpha = -abs(v_vec_ABZ(2))/sqrt(v_vec_ABZ(2)^2 +...
        zeta^2*(v_vec_ABZ(2)^2 + v_vec_ABZ(3)^2));
    n_beta = zeta*n_alpha;
    n_z = (v_vec_ABZ(3)/v_vec_ABZ(2))*n_beta;
    n_vec_ABZ = -[n_alpha; n_beta; n_z];

    % 5. rotate n_vec_ABZ from ABZ frame to heliocentric XYZ frame:
    n_vec_XYZ = R_ABZfromXYZ'*n_vec_ABZ;

    % 6. rotate n_vec_XYZ from XYZ frame to ECI frame:
    n_vec = R_XYZfromECI'*n_vec_XYZ; % unit normal vector in ECI frame
    n_vec_plate = n_vec;

    phi_plate = acos(dot(n_vec,s_vec));
        % reflected or incident angle of the antennae (rad)
```

```
        A_expp = A_plate;
            % assume controller faces full area of plate toward Sun always
        %~~~~~~~~~~~~~~~~~~~~~~~~~~~~~~~~~~~~~~~~~~~~~~~~~~~~~~~~~~~~~~~~~~~~
end

switch cont
    case {2,3} %controller 2 or 3
        % for the rotating cylinder:
        phi_cyl = 0;
            % reflected or incident angle of the cylinder
            % (always perpendicular to s_vec since a cylinder)
        n_vec_c = s_vec;
            % again, face of cylinder always perpendicular to s_vec
        n_vec_cyl = n_vec_c/norm(n_vec_c);  % UNIT vector

        % note: reflectivity coefficients [absorption; diffuse; specular]
        a_SRP_plate = (p_SR_complex*A_expp*cos(phi_plate)/m)*...
            (2*((c_R_plate(2)/3) + c_R_plate(3)*cos(phi_plate))*...
            n_vec_plate + (1-c_R_plate(3))*s_vec);
        a_SRP_cyl = (p_SR_complex*A_cyl*cos(phi_cyl)/m)*(2*((c_R_cyl(2)/3)...
            + c_R_cyl(3)*cos(phi_cyl))*n_vec_cyl + (1-c_R_cyl(3))*s_vec);
        a_SRP = -a_SRP_plate - a_SRP_cyl;

        SRP = R'*a_SRP; % SRP acceleration vector in RTN frame
end

return;
```

Appendix D. Disposal Orbit Guidelines

D.1 Satellite Disposal Guidelines

The United States Space Command (USSPACECOM) is tasked with defining and directing policies with respect to the disposal of satellites owned by the DoD. The pertaining policy directive, UPD10-39 (reference Section D.2), states that it is critical to remove abandoned spacecraft from orbit at the end of their orbital life. In "high value" operational orbits, there is an increasing threat of collision between satellites. Removing unused satellites from a given orbit (particularly low-Earth orbit and geosynchronous orbit) would both reduce the number of potential collisions and allow additional room for new satellites to be launched.

Necessary paperwork and approvals aside, the portion of the document pertinent to this thesis lies in Paragraph 5.4, entitled "Above Geosynchronous Orbit". Although the document states that a satellite may be disposed of using any of the methods listed in Section 5, the current orbit of the DSCS II satellite leads toward implementation of Paragraph 5.4. To summarize, USSPACECOM directs that the abandoned satellite must be maneuvered to an orbit with a perigee altitude above 36100 km. The DSCS II F-13 satellite already exceeds this requirement, however, for the purposes of this thesis it will still be used to determine how long it would take to raise its orbit a specified amount.

D.2 UPD10-39

BY ORDER OF USCINCSPACE

UNITED STATES SPACE COMMAND
POLICY DIRECTIVE 10-39

1 FEBRUARY 2001

Operations

SATELLITE DISPOSAL PROCEDURES

NOTICE: This publication is available digitally at: https://midway.peterson.af.mil/2letters/sc/css/scr/norad-us/utable.htm.

OPR: J35X (LCDR Steven R. White)
Supersedes UPD10-39, 3 Nov 97.

Certified by: JS (COL Robert A. Hammerle)
Pages: 7
Distribution: F

This policy directive establishes United States Space Command (USSPACECOM) policy on the disposal of Department of Defense owned satellites which Commander-in-Chief, US Space Command (USCINCSPACE) exercises Combatant Command (COCOM) authority as defined by the current Forces for Unified Commands document. It does not apply to Air Force Reserve Command (AFRC) nor Air National Guard (ANG) units.

SUMMARY OF REVISIONS

This policy directive incorporates updated guidance for satellite disposal methods/regions, with majority of revisions found in paragraphs **5.**-5.6. A bar (|) indicates a revision from the previous edition.

1. General. The space environment is critical as a medium for the collection and dissemination of data and information crucial to the warfighter's mission accomplishment. If the practice of abandoning spacecraft in-place within high value operational orbits at the end of their mission life continued, there will be an ever-increasing threat of collision between abandoned and operational satellites. Furthermore, such collisions themselves will become a major secondary source of orbital debris, posing a geometrically growing threat to future space operations that will be virtually impossible to control. To protect this vital resource from being polluted by space debris, this document provides direction and guidance for the proper disposal of satellites. These procedures comply with the minimization and mitigation of space debris as directed by National and Department of Defense (DOD) Space Policy. The guidelines do not preclude any end-of-life testing that the organization with satellite system responsibility deems necessary either prior to or following the placement into a disposal orbit.

2. Mission Payload/Vehicle Health. Removing a non-mission capable satellite from its operational orbit into an established disposal region is of paramount importance. As a satellite approaches the end of its operational life, each SATCOM System Expert (SSE) responsible for the satellite bus, or their equivalent for non-SATCOM systems (see **Table 1.** and **Table 2.**), will ensure that every satellite maintains adequate disposal capability. This is to include assuring command/control capability and maintaining the required amount of fuel to reach the disposal region. Disposal of vehicles approaching the end of their

operational life will be recommended if further degradation precludes future removal from high-value operational orbits.

Table 1. Organizations With System Responsibility (Communication Satellites and Secondary Payloads).

SATELLITE SYSTEMS/ PAYLOADS	SATCOM OPERATIONAL MANAGER (SOM)	SATCOM SYSTEM EXPERT (SSE)
FLTSAT, UHF Follow-On (UFO), FEP, UFO(E), UFO(EE), Polar EHF, GBS Phase II	USSPACECOM	NAVSPACECOM
DSCS	USSPACECOM	DISA
Milstar, AFSATCOM, SCTS, Polar UHF, LES	USSPACECOM	AFSPC

Table 2. Organizations With System Responsibility (Non-Communication Satellites).

SATELLITE SYSTEMS	ORGANIZATION
DSP	SPACEAF
DMSP	SPACEAF in coordination with the National Polar-Orbiting Operational Environment Satellite System (NPOESS) Integrated Program Office (IPO)
GPS	SPACEAF

3. Disposal Criteria. SATCOM System Experts (SSE's), or their equivalent for non-SATCOM systems, will coordinate with sustainment and satellite operations activities, components or agencies with secondary payloads on the bus, and develop specific criteria for satellite disposal. USSPACECOM components and agencies will forward the criteria to USSPACECOM/J3 (and J6 for SATCOM systems) for review and approval. The disposal criteria will include the minimum acceptable levels of bus support to the payloads, payload capability and capacity (primary and secondary), vehicle command/control capability, vehicle power capacity, fuel requirements for disposal maneuver, and any other disposal maneuver requirements.

4. Standard Operations. As part of standard operations, SATCOM System Experts (SSE's), or their equivalent, will monitor satellite capability criteria. Once a satellite has been designated non-mission capable per the established criteria and/or is demonstrating potential disposal capability problems, the organization will forward a disposal recommendation as described below. At a minimum, the recommendation will include the disposal criteria that are being met and projected date of disposal. Standard disposal recommendations should be sent three months in advance of the anticipated disposal date.

4.1. Military Satellite Communications (MILSATCOM) Disposal Recommendation. SATCOM System Experts (SSE's) will forward the satellite disposal recommendation to USSPACECOM/J6. USSPACECOM/J3/J6 will then coordinate with other government agencies to determine any

requirements for, and the feasibility of, potential alternate use. USSPACECOM will then consolidate these requirements, and make a recommendation to Joint Staff/J6 on the satellite's disposition. Once final approval is received, USSPACECOM/J3 will direct disposal action. The SSE will develop and provide a plan of action and timeline for disposal/transfer to include end-of-life testing requirements, Test and Checkout (TACO), and disposal orbit parameters to USSPACECOM/J6/Global SATCOM Support Center (GSSC). A final status report will be released by the SATCOM Operational Manager (SOM) to the SATCOM community (i.e., CINCs, Joint Program Offices, USSPACECOM components, etc.). If the satellite is recommended for continued use by another agency, then the operations/maintenance/support and final disposal plan will be coordinated with the Joint Staff J3/J6.

4.2. Non-MILSATCOM Disposal Recommendation. The organization with satellite system responsibility will submit their disposal recommendation to USSPACECOM/J3, who will make the determination for final disposition. Once approval has been granted, the responsible organization will develop and provide a plan of action and timeline for disposal to include end-of-life testing requirements, TACO, and disposal orbit parameters to USSPACECOM/J3.

4.3. Emergency Situation. In the case of an emergency where it is believed that there is less than 30 days to react, the decision process for the safe disposal of a satellite must be expedited. The Satellite Control Authority (SCA)/system operator will make a telephone request, followed by message, for disposal to the SATCOM System Experts (SSE), or their equivalent for non-SATCOM systems. The SATCOM System Experts (SSE), or their equivalent, will coordinate via phone and message with USSPACECOM/J6 for MILSATCOM systems or USSPACECOM/J3 for non-MILSATCOM systems. USSPACECOM/J3/J6 will coordinate the disposal recommendation.

4.4. Maneuver Vector Screening. The component will ensure planned disposal vectors and orbit parameters are submitted to Cheyenne Mountain Operations Center (CMOC), J3SY Combat Analysis Branch before disposal for approval of reentry locations and/or orbital safety screening for possible conflicts. USSPACECOM/J3 will resolve any conflicts concerning reentry locations and/or orbital safety screening. After disposal maneuvers have been completed, the component will ensure that the final vectors are provided to CMOC. If the satellite fails to reach proper disposal orbit, the Space Control Center (SCC) will conduct conjunction analysis. If there is a possible conflict with a manned space vehicle or other objects, continue routine conjunction analysis. Notify the Space Operations Center (SPOC) and other space partners of all conjunctions associated with disposal operations.

5. Post Mission Disposal. Satellites should be disposed of by one of the following methods. Because of fuel gauging uncertainties near the end of mission, a disposal plan should use a maneuver strategy that most reduces the risk of leaving the satellite near a high-value orbit. The disposal region perigee and apogee altitudes listed below should prevent lunar and solar perturbations from causing these satellites to interfere with high-value operational orbits. Programs whose current design capabilities are unable to meet the guidelines listed in paragraphs **5.1.-5.6.**, will optimize disposal actions based on the published design capabilities.

5.1. Atmospheric Reentry. Maneuver the satellite to an orbit in which, using conservative projections for solar activity and other perturbations, atmospheric drag will cause atmospheric reentry within 25 years after completion of mission. If atmospheric reentry is performed by a planned deorbit, it will be planned such that any remaining portions of the satellite will impact the earth only in non-populated, preferably oceanic, areas.

5.2. Between Low Earth Orbit (LEO) and Medium Earth Orbit (MEO)/Semisynchronous. Maneuver the satellite to an orbit with perigee altitude above 2,000 km and apogee altitude below 19,700 km.

5.3. Between Medium Earth Orbit (MEO)/Semisynchronous and Geosynchronous Earth Orbit (GEO). Maneuver the satellite to an orbit with perigee altitude above 20,700 km and apogee altitude below 35,300 km.

5.4. Above Geosynchronous Earth Orbit (GEO). Maneuver the satellite to an orbit with perigee altitude above 36,100 km.

5.5. Heliocentric, Earth-escape. Maneuver to remove the satellite from Earth orbit, into a heliocentric orbit.

5.6. Direct retrieval. Retrieve the satellite and remove it from orbit as soon as practical after mission completion.

6. Safing. Properly safing the payloads and the bus is a critical step in the disposal process. This process will assist in the elimination of stored energy from the satellite and limit the probability of post mission explosion spreading more debris. Safing procedures to be considered vary with each system, but may include burning all residual fuel to depletion and leaving fuel lines with valves open; disabling all battery charging systems; leaving batteries in a permanent discharge state; venting all pressurized systems; removing power from control moment gyroscopes; disabling transmitters; deactivating range safety systems; depleting all volatile liquids; or stabilizing the spacecraft in a neutral thermal flight mode.

7. Review. This policy directive will be reviewed at least every 3 years to ensure the most current guidance is provided.

RALPH E. EBERHART, General, USAF
Commander in Chief

Attachment 1

GLOSSARY OF REFERENCES AND SUPPORTING INFORMATION

References

Presidential Decision Directive (PDD) NSC-49/NSTC-8, ***National Space Policy***

Department of Defense Directive 3100.10, ***Space Policy***

United States Space Command Instruction (UI) 13-4, ***Minimization and Mitigation of Space Debris***

NASA Safety Standard 1740

National Reconnaissance Office Instruction (NROI) 82-3, ***Satellite Debris Mitigation-End of Life***

Chairman of the Joint Chiefs of Staff, CJCSI 6250.01, ***Satellite Communications***

Terms

Apogee—The point of a satellite's greatest distance from Earth and minimum velocity.

Combatant Command (COCOM)—Non-transferable command authority established by title 10, United States Code, Section 164, exercised only by commanders of unified combatant commands. COCOM is the authority of a Combatant Commander, to perform those functions of command over assigned forces involving organizing and employing commands and forces, assigning tasks, designating objectives, and giving authoritative direction over all aspects of military operations, joint training, and logistics necessary to accomplish the mission assigned to the command. COCOM provides full authority to organize and employ commands and forces as the CINC considers necessary to accomplish assigned missions.

Military Satellite Communications (MILSATCOM)—The satellite communications resources that are owned and operated by DOD primarily in the government frequency bands. USCINCSPACE COCOM systems include, but are not limited to, Defense Satellite Communications System (DSCS), Fleet Satellite (FLTSAT), UHF Follow-on (UFO), and Milstar.

Perigee—The point of a satellite's closest approach to Earth and greatest velocity.

SATCOM System Expert (SSE)—The component or designated organization responsible for providing the technical planning and functions in support of the operational management of a specific SATCOM constellation.

Satellite Control Authority (SCA)—The authority to provide Telemetry, Tracking and Commanding (TT&C) of the satellite's bus and to provide control and management of the satellite's payload. Authority is inherent in the Operational Control (OPCON) of a satellite or can be delegated in part or entirely to another organization.

Secondary Payloads—Those payloads placed on a satellite that provide a different capability than its primary payload. The secondary capability of a satellite system is taken into consideration when making a decision to dispose of a satellite.

USSPACECOM Components—The three service components of USSPACECOM are U.S. Army Space Command (USARSPACECOM), Naval Space Command (NAVSPACECOM), and 14th Air Force (SPACEAF). 14th Air Force, Vandenberg AFB, California, which falls under the administrative control

of Air Force Space Command (AFSPC), Peterson AFB, Colorado, is dual hatted as SPACEAF and operates as USSPACECOM's functional component.

Attachment 2

METRICS TO MEASURE COMPLIANCE WITH POLICY

A2.1. The purpose of metrics is to identify the established goals or standards based on our customers needs and measure how well we meet the standards based on our customers feedback. The key metrics in the disposal process are satellites that are placed within disposal regions for present satellite systems and incorporation of disposal capabilities for future systems. These metrics will be reviewed and revised every 3 years, or as needed.

A2.2. Execute Satellite Placement into a Disposal Orbit. This metric measures the number of satellites placed into a proper disposal region after having been declared non-mission capable or subsystem disposal criteria are met. The goal is to place all non-mission capable satellites into a specified disposal region.

A2.2.1. Customer: Primary-USSPACECOM; secondary-DOD, National and commercial users.

A2.2.2. Goal and source: 100 percent insertion to proper disposal region, determined by Cheyenne Mountain Operations Center (CMOC).

A2.2.3. Data source: Organization with satellite system responsibility and CMOC.

A2.2.4. Calculation method: Percentage determined by dividing the number of satellites reaching a disposal region by the total number of satellites being disposed of (not to include those satellites undergoing end-of-life testing prior to disposal).

A2.3. Satellite Programs Planning for Disposal Capabilities**.** This metric compares the number of new satellite programs being developed with the number of these programs that incorporate a disposal capability into the system that meets the requirements of this directive. As long as a satellite has the capability to meet the disposal criteria upon launch, this requirement is being met.

A2.3.1. Customer: Primary-USSPACECOM; secondary-DOD, National and commercial users.

A2.3.2. Goal and source: 100 percent of future satellite programs being developed incorporate satellite disposal capabilities, as determined by System Program Offices (SPOs).

A2.3.3. Data source: Space and Missile Command (SMC) SPOs.

A2.3.4. Calculation method: Percentage determined by dividing the number of new programs that incorporate a disposal capability by the number of new satellite programs.

Bibliography

1. 45 Space Wing Office of History . "The Cape: Miltary Space Operations 1971-1992." *https://www.patrick.af.mil/heritage/Cape/Cape2/Cape2-5.htm*, July 2002.

2. Battin R. H. *An Introduction to the Mathematics and Methods of Astrodynamics*. New York, NY: AIAA Education Series, American Institute of Aeronautics and Astronautics, 1987.

3. Betts J. T. "Optimal Interplanetary Orbit Transfers by Direct Transcription," *The Journal of the Astronautical Sciences*, *42*(3):247–268 (September 1994).

4. Betts J. T. "Very Low-thrust Trajectory Optimization Using a Direct SQP Method," *Journal of Computational and Applied Mathematics*, *120*:27–40 (September 2000).

5. Betts J. T. and Erb S. O. "Optimal Low Thrust Trajectories to the Moon," *Society for Industrial and Applied Mathematics Journal of Applied Dynamical Systems*, *2*(2):144–170 (May 2003).

6. Broucke R. A. and Cefola P. J. "On the Equinoctial Orbit Elements," *Celestial Mechanics*, *5*:303–310 (1972).

7. Bryant R. W. "The Effect of Solar Radiation Pressure on the Motion of an Artificial Satellite," *NASA Technical Note*, *D-1063*:1–8 (September 1961).

8. Chobotov V. A. *Spacecraft Attitude Dynamics and Control*. Malabar, FL 32950: Krieger Publishing Co, 1991.

9. Chobotov V. A., editor. *Orbital Mechanics*. Reston, VA 20191-4344: AIAA, 2002. 3rd ed.

10. Cook D. G. *Solar Radiation Pressure Modeling Issues for High Altitude Satellites*. MS thesis, Graduate School of Engineering, Air Force Institute of Technology (AETC), Wright-Patterson AFB OH, 2001. AFIT/GSO/ENY/01M-01.

11. Coverstone V. L. and Prussing J. E. "Technique for Escape From Geosynchronous Transfer Orbit Using a Solar Sail," *Journal of Guidance, Control, and Dynamics*, *26*(4):628–634 (July-August 2003).

12. Ferraz-Mello S. "Analytical Study of the Earth's Shadowing Effects on Satellite Orbits," *Celestial Mechanics*, *5*:80–101 (1972).

13. Georgevic R. M. "The Solar Radiation Pressure Force and Torques Model," *The Journal of the Astronautical Sciences*, *20*(5):257–274 (March-April 1973).

14. Hale F. J. *Introduction to Space Flight*. Englewood Cliffs, NJ: Prentice Hall, 1994.

15. Hall C. D. "AOE4140 Lecture Notes Appendix A." January 2003.

16. Kabelac J. "Shadow Function - Contribution to the Theory of the Motion of Artificial Satellites," *Bulletin. Astronomical Institutes of Czecholovakia*, *39*:213–220 (1988).

17. Kechichian J. A. "Optimal Low-thrust Rendezvous Using Equinoctial Orbital Elements," *Acta Astronautica*, *38*(1):1–14 (1996).

18. Kechichian J. A. "The Treatment of the Earth Oblateness Effect in Trajectory Optimization in Equinoctial Coordinates," *Acta Astronautica*, *40*(1):69–82 (1997).

19. Longo C. R. O. and Rickman S. L. "Method for the Calculation of Spacecraft Umbra and Penumbra Shadow Terminator Points," *NASA Technical Paper* (April 1995).

20. Marasch M. W. and Hall C. D. "Application of Energy Storage To Solar Electric Propulsion Orbital Transfer," *Journal of Spacecraft and Rockets* (April 1999).

21. McCants M. "Keplerian Elements Formats." Radio Amateur Satellite Corporation (AMSAT), March 1999.

22. McInnes C. "Solar Sail Mission." Internet, University of Glasgow, Department of Aerospace Engineering, *http://www.aero.gla.ac.uk/Research/Ss/Solar.htm*, February 2001.

23. NASA Joint Propulsion Laboratory . "DSCS II Quicklook." JPL Mission and Spacecraft Library, *http://msl.jpl.nasa.gov/QuickLooks/dscs2QL.html*, 2005.

24. NASA National Space Science Data Center at Goddard Space Flight Center , "Planetary and Lunar Missions Under Consideration." Internet, October 2005.

25. Proulx R., Cefola P., and Luu K. "The Role of Short-periodic Motion in Formation Flying of Satellites With Large Differential Area to Mass Ratio," *Advances in the Astronautical Sciences*, *109*(III):2127–2148 (2002).

26. Rieber R. "Newton-Raphson MATLAB® Iteration Code." January 2005.

27. Space and Missile Systems Center, Detachment 12 . "Mission Statement." *http://www.smc.kirtland.af.mil/*, 2005.

28. Space-Track *http://www.space-track.org*, 2004.

29. The James Clerk Maxwell Foundation *www.clerkmaxwellfoundation.org*, August 1998.

30. Trawny N., Graesslin M., Laufer R., and Roeser H.-P. "Mission Scenarios for a Controlled Lunar Impact of a Small Satellite," *55th International Astronautical Congress (Vancouver, Canada)*, 1–6 (October 2004).

31. United States Naval Observatory , "Earth's Seasons, Equinoxes, Solstices, Perihelion and Aphelion, 1992-2020." Internet, October 2003. Astronomical Applications Department.

32. Vallado D. A. *Fundamentals of Astrodynamics and Applications*. Boston, Massachusetts: Kluwer Academic Publishers, 2001. 2nd ed.

33. Vokrouhlicky D. and Farinella P. "Radiative Forces and LAGEOS' Orbit," *Advances in Space Research*, *16*(12):15–19 (1995).

34. Walker M. J. H., Ireland B., and Owens J. "A Set of Modified Equinoctial Orbit Elements," *Celestial Mechanics*, *36*:409–419 (1985).

35. Wie B. *Space Vehicle Dynamics and Control*. Reston, VA: American Institute of Aeronautics and Astronautics, 1998.

36. Williams D. R. "SELenological and ENgineering Explorer (SELENE)." *http://nssdc.gsfc.nasa.gov/database/MasterCatalog?sc=SELENE*, September 2005.

37. Wilson A., editor. *Jane's Space Directory*. Sentinel House, 163 Brighton Rd, Coulson, Surrey CR5 2NH, UK: Jane's Information Group Limited, 1993. 9th ed.

REPORT DOCUMENTATION PAGE

Form Approved
OMB No. 0704–0188

1. REPORT DATE *(DD–MM–YYYY)*	2. REPORT TYPE	3. DATES COVERED *(From — To)*
23–03–2006	Master's Thesis	Jun 2004 — Mar 2006

4. TITLE AND SUBTITLE

The Effects of Using Solar Radiation Pressure to Alleviate Fuel Requirements for Orbit Changing and Maintenance of the DSCS II F-13 Satellite

5a. CONTRACT NUMBER

5b. GRANT NUMBER

5c. PROGRAM ELEMENT NUMBER

6. AUTHOR(S)

Jody A. Paris, Capt, USAF

5d. PROJECT NUMBER

5e. TASK NUMBER

5f. WORK UNIT NUMBER

7. PERFORMING ORGANIZATION NAME(S) AND ADDRESS(ES)

Air Force Institute of Technology
Graduate School of Engineering and Management (AFIT/EN)
2950 Hobson Way
WPAFB OH 45433-7765

8. PERFORMING ORGANIZATION REPORT NUMBER

AFIT/GA/ENY/06-M08

9. SPONSORING / MONITORING AGENCY NAME(S) AND ADDRESS(ES)

AFSPC/SMC/Det 12
Attn: Mr. Daniel Crouch
3548 Aberdeen Ave SE
Kirtland AFB, NM 87117
DSN: 263–1780, Email: daniel.crouch@kirtland.af.mil

10. SPONSOR/MONITOR'S ACRONYM(S)

11. SPONSOR/MONITOR'S REPORT NUMBER(S)

12. DISTRIBUTION / AVAILABILITY STATEMENT

APPROVED FOR PUBLIC RELEASE; DISTRIBUTION UNLIMITED.

13. SUPPLEMENTARY NOTES

14. ABSTRACT

Orbit disposal and maintenance of aging satellites has become a significant concern over the past few years, as the increasing number of orbiting objects threatens to limit the launching of future satellites. Many of the satellites currently in orbit, however, were not built with disposal considerations. The DSCS II series was launched into orbit beginning in the 1970s, and many satellites are now without the fuel required to conventionally transition to a sanctioned disposal orbit. In GEO orbit the largest non-gravitational perturbation is solar radiation pressure. By adjusting the attitude of a satellite with a controller to maximize the perturbing acceleration due to the force of SRP, the satellite can be slowly raised into a disposal orbit. The results from this study, along with validation results propagated with STK, are presented. After making several simplifying assumptions, the time required to raise the modelled DSCS II F-13 satellite 400 km into a disposal orbit is approximately 33 years. This time-to-disposal can be reduced by using a larger area-to-mass ratio and more reflective surface materials.

15. SUBJECT TERMS

solar radiation pressure, stationkeeping, disposal orbit, maneuvering satellites, equations of motion, earth orbits, modified equinoctial elements

16. SECURITY CLASSIFICATION OF:			17. LIMITATION OF ABSTRACT	18. NUMBER OF PAGES	19a. NAME OF RESPONSIBLE PERSON
a. REPORT	b. ABSTRACT	c. THIS PAGE			Nathan A. Titus, Lt Col, USAF
U	U	U	UU	155	19b. TELEPHONE NUMBER *(include area code)* (937) 255-3636 x4597, nathan.titus@afit.edu